CERN–2006–006
12 July 2006

ORGANISATION EUROPÉENNE POUR LA RECHERCHE NUCLÉAIRE
CERN EUROPEAN ORGANIZATION FOR NUCLEAR RESEARCH

Conceptual design of the SPL II

A high-power superconducting H^- linac at CERN

F. Gerigk (Editor), M. Baylac[1], E. Benedico Mora, F. Caspers, S. Chel[2], J.M. Deconto[1], R. Duperrier[2], E. Froidefond[1], R. Garoby, K. Hanke, C. Hill, M. Hori[3], J. Inigo-Golfin, K. Kahle, T. Kroyer, D. Kuechler, J.-B. Lallement, M. Lindroos, A.M. Lombardi, A. López Hernández, M. Magistris, T.K. Meinschad, A. Millich, E. Noah Messomo, C. Pagani[4], V. Palladino[5], M. Paoluzzi, M. Pasini, P. Pierini[4], C. Rossi, J.P. Royer, M. Sanmarti, E. Sargsyan, R. Scrivens, M. Silari, T. Steiner, J. Tückmantel, D. Uriot[2], M. Vretenar

GENEVA
2006

[1] LPSC Grenoble.
[2] CEA Saclay.
[3] CERN/Tokyo University.
[4] INFN Milan.
[5] INFN Naples.

CERN–800 copies printed–July 2006

Abstract

An analysis of the revised physics needs and recent progress in the technology of superconducting RF cavities have led to major changes in the specification and in the design for a Superconducting Proton Linac (SPL) at CERN. Compared with the first conceptual design report (CERN 2000–012) the beam energy is almost doubled (3.5 GeV instead of 2.2 GeV), while the length of the linac is reduced by 40% and the repetition rate is reduced to 50 Hz. The basic beam power is at a level of 4–5 MW and the approach chosen offers enough margins for upgrades. With this high beam power, the SPL can be the proton driver for an ISOL-type radioactive ion beam facility of the next generation ('EURISOL'), and for a neutrino facility based on superbeam + beta-beam or on muon decay in a storage ring ('neutrino factory'). The SPL can also replace the Linac2 and PS Booster in the low-energy part of the CERN proton accelerator complex, improving significantly the beam performance in terms of brightness and intensity for the benefit of all users including the LHC and its luminosity upgrade. Decommissioned LEP klystrons and RF equipment are used to provide RF power at a frequency of 352.2 MHz in the low-energy part of the accelerator. Beyond 90 MeV, the RF frequency is doubled to take advantage of more compact normal-conducting accelerating structures up to an energy of 180 MeV. From there, state-of-the-art, high-gradient, bulk-niobium superconducting cavities accelerate the beam up to its final energy of 3.5 GeV. The overall design approach is presented, together with the progress that has been achieved since the publication of the first conceptual design report.

Contents

Tables

Acronyms and abbreviations

AD	Antiproton Decelerator
ADS	Accelerator Driven Systems
APT	Accelerator Production of Tritium
BARC	Bhabha Atomic Research Centre, India
BCP	Buffered Chemical Polishing
BENE	Beams for European Neutrino Experiments
BINP	Budker Institute of Nuclear Physics, Russia
BPM	Beam Position Monitor
CAT	Centre for Advanced Technology, India
CCC	CERN Control Centre
CCDTL	Cell-Coupled Drift Tube Linac
CCL	Coupled-Cavity Linac
CDR1	Conceptual Design of the SPL, 2000
CDR2	Conceptual Design of the SPL II, 2006
CEA	Commissariat pour l'Energie Atomique, France
CEBAF	Continuous Electron Beam Accelerator Facility, USA
CNRS	Centre National de la Recherche Scientifique
CP	Charge-conjugation Parity
CW	Continuous Wave (operation)
DC	Direct Current
DESY	Deutsches Elektronen SYnchrotron, Germany
DTL	Drift Tube Linac
EP	Electrolytical Polishing
ESS	European Spallation Source
EURISOL	EURopean Isotope Separation On-Line
HARP	Hadron production experiment at CERN
HIPPI	High Intensity Pulsed Proton Injectors, Europe
HOM	Higher Order Mode
HPR	High Pressure Rinsing
HVAC	Heating Ventilation and Air Conditioning
ILC	International Linear Collider
IN2P3	Institut Nationale de Physique Nucléaire et de Physique des Particules, France
INFN	Istituto Nazionale di Fisica Nucleare, Italy
IPHI	Injecteur de Protons de Haute Intensité, France
ISOL	Isotope Separator On-Line
ISOLDE	Isotope Separator On Line Experiment at CERN
ISR	Intersecting Storage Rings
ISS	International Scoping Study
ISTC	International Science and Technology Center, Russia
ITEP	Institute for Theoretical and Experimental Physics, Russia
JPARC	Japan Proton Accelerator Research Complex, Japan
LANL	Los Alamos National Laboratory, USA
LEBT	Low Energy Beam Transport
LEP	Large Electron–Positron collider at CERN
LHC	Large Hadron Collider at CERN

Linac	Linear accelerator
LPSC	Laboratoire de Physique Subatomique et de Cosmologie, France
MEBT	Medium Energy Beam Transport
MLI	Multi-Layer Insulation
MOSFET	Metal Oxide Semiconductor Field Effect Transistor
MPS	Machine Protection System
Nb/Cu	Niobium on copper
NC	Normal-conducting
nToF	neutron Time of Flight
PLC	Programmable Logic Controller
ppp	protons per pulse
PPS	Personnel Protection System
pps	protons per second
PS	Proton Synchrotron at CERN
PSB	PS Booster
RF	Radio Frequency
RFQ	Radio Frequency Quadrupole
RIA	Rare Isotope Accelerator
RIB	Radioactive Ion Beam
r.m.s.	root mean square
RRR	Residual Resistance Ratio (resistivity at 300 K/residual resistivity at operating temperature)
SC	SuperConducting
SCL	Side-Coupled Linac
SEM	Secondary Electron emission Monitor
SNS	Spallation Neutron Source, USA
SPL	Superconducting Proton Linac at CERN
SPS	Super Proton Synchrotron at CERN
TERA	TErapia con Radiazioni Adroniche, Italy
TESLA	TeV Energy Superconducting Linear Accelerator project. Lead laboratory: DESY, Germany
TRASCO	TRAsmutazione SCOrie, Italy
TTF	TESLA Test Facility, Germany
TTL	Transistor–Transistor Logic
VNIIEF	All-Russian Scientific Research Institute of Experimental Physics, Russia
VNIITF	All-Russian Scientific Research Institute of Technical Physics, Russia
XFEL	X-ray Free Electron Laser, Europe

Chapter 1

Introduction and executive summary

The construction of a Superconducting Proton Linac (SPL) at CERN was initially proposed as an economical means to replace the Proton Synchrotron (PS) injectors (Linac2 and PSB), re-using the valuable asset of RF equipment resulting from the decommissioning of the Large Electron–Positron (LEP) collider. When the idea of a neutrino factory based on muon decay was suggested, the SPL, because of its potential for high beam power, became a very attractive solution for the proton driver. The design of the accelerator evolved to match the needs of such a facility, while respecting the constraints of the existing RF equipment. Thereafter a basic scheme for a neutrino factory at CERN was worked upon, until efforts were drastically reduced and most resources were re-oriented towards the Large Hadron Collider (LHC). Only the developments concerning the SPL, in particular its low-energy part, continued to be supported because of their potential application in 'Linac4', the successor to Linac2.

In 2002, an alternative concept for a neutrino facility based on beta-decaying radioactive ions was proposed by P. Zucchelli [1]. The association of such a source of ν_e or anti-ν_e with a neutrino superbeam generating a high flux of ν_μ or anti-ν_μ in the same energy range is especially powerful. Assuming that the existing CERN accelerators would be used to accelerate these ions, the optimum energy for the proton driver generating the neutrino superbeam was then determined to be $\approx$ 3.5 GeV [2]. As this energy is also better for the other applications like neutrino factory and PS injector, it has been selected for the updated design of the SPL (see Chapter 2). The basic characteristics for this new design are summarized in Table 1.1. Design details are presented in Chapter 4.

Table 1.1: SPL main characteristics

Mean beam power	5 MW
Beam kinetic energy	3.5 GeV
Repetition rate	50 Hz
Number of protons per pulse/per second	$0.178/8.92 \times 10^{15}$
Pulse length	0.72 ms
Average pulse current†	40 mA
Overall length‡	430 m
Bunch frequency	352.2 MHz

† After chopping.

‡ Pure linac length without debuncher section (see Section 4.5.1).

To operate at these increased energy and current levels, more instantaneous RF power is needed than available with the existing LEP klystrons. Combined with the remarkable progress in superconducting RF technology, this led to the decision to use pulsed klystrons and a harmonic of 352.2 MHz (704.4 MHz) in the superconducting part of the accelerator. As a direct result of this optimization, the second version of the SPL is 340 m shorter than the initial one (430 m instead of 770 m length without debuncher section at the linac end), even though it accelerates up to 3.5 GeV instead of 2.2 GeV.

The RF frequency of 352.2 MHz remains very convenient at low energy, leading to acceptable dimensions, tolerances and gradients in the normal-conducting, low-β accelerating structures like Radio Frequency Quadrupoles (RFQ), Drift Tube Linac (DTL) and Cell-Coupled Drift Tube Linac (CCDTL) up to the energy of 90 MeV. Fourteen LEP klystrons and circulators will be re-used in this part of the linac. In the rest of the SPL, the frequency is doubled to 704.4 MHz. Normal-conducting SCL structures are employed up to 180 MeV, and multi-cell elliptical superconducting cavities afterwards. It is proposed

to build the first part of the linac, up to 160 MeV (Linac4), in an existing hall close to the PS and to use it as an improved injector for the PSB.

The layout of the SPL on the CERN site is similar to that of the previous proposal, except for its reduced length (see Fig. 1.1). The existing transfer tunnels allow for an easy connection to the PS and the ISOLDE/EURISOL experimental area. The accumulator and compressor rings needed for a neutrino factory could be located inside the Intersecting Storage Rings (ISR) tunnel or in its vicinity.

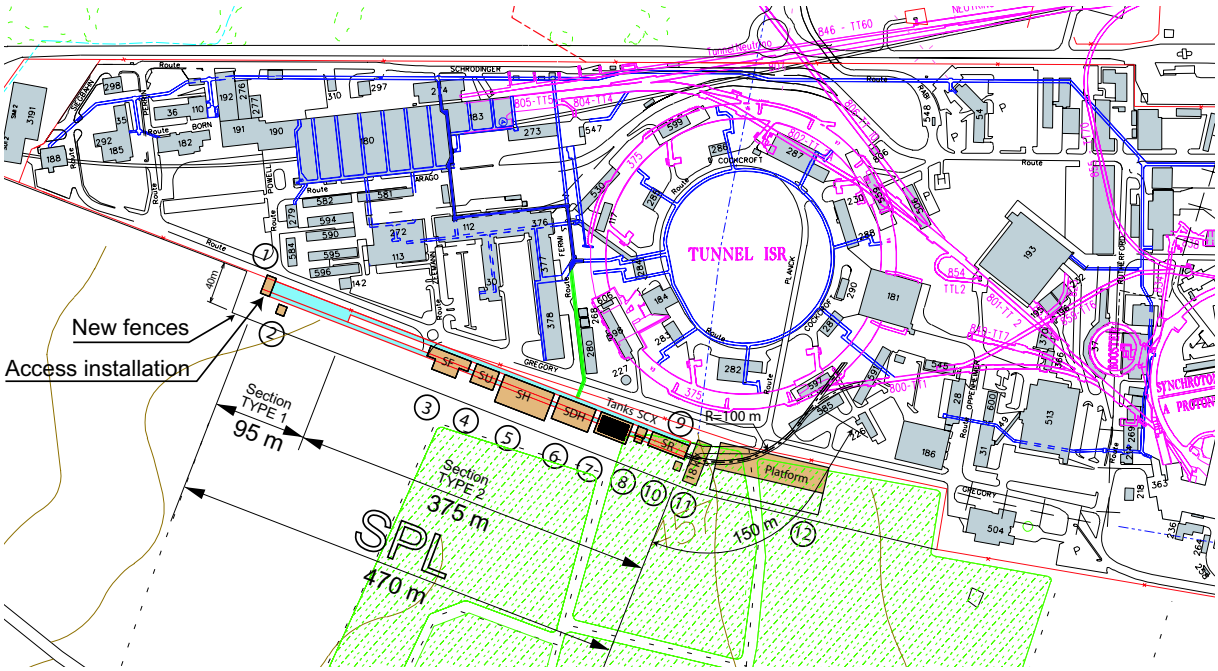

Fig. 1.1: SPL layout on the CERN site

The new design and layout of the SPL leaves room for evolution in terms of beam energy and beam power. The space available at the foreseen location allows for a longer accelerator length, and hence a higher beam energy. The infrastructure is already dimensioned for the beam power of 5 MW that is required for an ISOL-type second-generation facility like EURISOL.

Chapter 2

Choice of parameters and overall design

The SPL design in the first conceptual design report (CDR1) [3] was mainly driven by the high-power needs of a CERN-based neutrino factory [4] and the idea to re-use RF equipment [klystrons, waveguides, and superconducting (SC) cavities] from the decommissioned LEP collider at CERN. In the mean time, the needs of the neutrino production schemes have changed and EURISOL became an additional potential high-power user of the SPL. Moreover, the requirements of the CERN proton chain [5, 6] in view of possible LHC luminosity upgrades are more clear [7, 8] and there has been considerable progress in the technology of bulk-niobium SC cavities. The high-power needs of EURISOL and possible neutrino facilities, together with the requirements of LHC upgrade scenarios, led to a revision of the SPL parameters and to a re-design of the linac itself taking into account the latest technical developments in the field of high-intensity proton linacs [9].

2.1 Neutrino production

Three different neutrino production methods are considered to be covered by the SPL (see Section 3.1):

a) Superbeam: 4 MW proton beam + accumulator ring + pion production target.
b) Beta-beam: $\approx$ 200 kW of the 4 MW proton beam + ISOL-type target + PS, SPS + decay ring.
c) Neutrino factory: 4 MW proton beam + accumulator and compressor ring + pion production target + muon cooling and capture channel + muon acceleration + muon decay ring.

While the neutrino factory scenario offers the ultimate potential for neutrino physics, a combination of the superbeam and beta-beam scenarios in the same energy range appears as a possible viable alternative. Making use of the CERN infrastructure for the beta-beam scenario, the optimum energy for a CERN-based superbeam facility was determined to be 3.5 GeV [2].

Recent simulation work for options (a) and (c) seems to indicate that the optimum energy for pion production targets is somewhere between 5 GeV and 10 GeV [10, 11]. At these energies the simulations show up to 50% higher transmission through an example muon front-end than for energies around 1–2 GeV. However, for lack of experimental data the computed results in the region of 3–5 GeV are still uncertain and will have to be confirmed by experiments. At present 3.5 GeV seems a reasonable compromise between the size of the linac and the pion production rate, even if it is likely that the optimum energy will be slightly higher. Considering the much more compact design of the revised SPL design, it is possible to increase the energy of the SPL by several GeV if needed (see also Section 6.1).

Another commonality of the superbeam and neutrino factory options is the need for an accumulator ring (plus compressor ring in the case of a neutrino factory) to achieve the required time structure. The base line scenario for CDR1 and this second design (CDR2) is the assumption to use the ISR tunnel for this purpose. In CDR1 the large circumference ($\approx$ 1 km) of the ISR tunnel was needed to limit the number of injection turns. Owing to the long beam pulse length (2.2 ms), however, 660 injection turns were still needed to fill the accumulator/compressor ring at a repetition frequency of 75 Hz. At this high number of turns the heating of the H^- injection foil and possible beam instabilities during the injection period may develop into intensity limitations for the whole proton driver complex. One goal in the re-design of the SPL was to remove this potential bottleneck and at the same time to reduce the size of the accumulator/compressor ring. In the new scheme for 'neutrino operation' of the SPL, the beam pulse length is reduced to 0.57 ms at 3.5 GeV and would require only 176 injection turns into an ISR-sized ring instead of 660 as assumed in the previous design (see Fig. 2.1). The shorter pulse length opens the possibility to reduce the size of the accumulator/compressor ring (and by doing so to reduce the cost of lattice) while still keeping a reduced number of injection turns. A reduction in size of $\approx$ 50% would

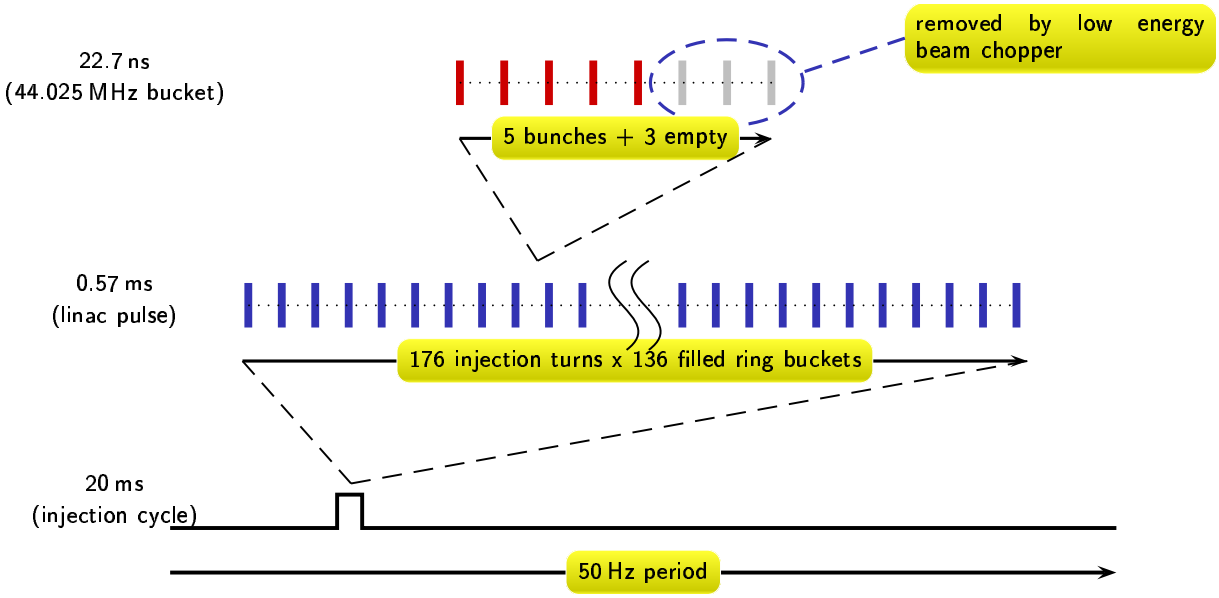

Fig. 2.1: Possible timing scheme for 'neutrino operation' assuming an accumulator and compressor ring with a 44 MHz RF system in the ISR tunnel

require $\approx$ 360 injection turns and would result in a ring that could be built either in a new tunnel inside the ISR or at a different, more convenient location on the CERN site.

2.2 EURISOL operation

Two types of target are foreseen in the reference scenario of the EURISOL design study [12] (see Section 3.2). For the time being, both the high-power (5 MW) and the low-power (100 kW) targets assume a continuous-wave (CW) proton beam at 1 GeV. The transition to pulsed beams will in both cases reduce the lifetime of the targets because of the increase of thermal stresses. In the case of the low-power targets, first studies [13] indicate that for a pulsed machine the pulse lengths should be of the order of 1 ms and the repetition rate should be 50 Hz (or higher) to minimize the instantaneous thermal load in the target. So far the various cross-sections for fragmentation and/or spallation in the low-power target do not indicate a clear advantage or disadvantage of using a 3.5 GeV beam rather than a 1 GeV beam. High-power target studies [14] for CW beams at different energies show that the spallation efficiency reaches its maximum between 1 GeV and 2 GeV, though there is little difference in neutron flux for a 1 GeV or 3.5 GeV beam. At higher energies the heat deposition in the target will be more evenly distributed and there is a significant reduction in the power deposited in the window. On the other hand, more primary protons will escape at higher energies if one assumes an equal target length for 1 GeV and 3.5 GeV beams. The impact of pulsed operation on EURISOL high-power targets has not yet been studied in detail. However, similar challenges are faced by the Spallation Neutron Source (SNS) [15] or in the studies for the European Spallation Source (ESS) [16]. A possible timing scheme to produce a 5 MW beam for EURISOL is depicted in Fig. 2.2.

In this scenario, the low-energy beam chopper creates a $\approx$ 0.1 ms gap in the bunch train to switch the beam from the high-power to a low-power target. A second possible way to share the beam within one pulse is to use partial resonant laser stripping to 'shave off' a fraction of the beam over the whole pulse length, which can then be diverted to one (or more) different users. Given that the R&D on laser stripping is showing success, this method would relax the instantaneous thermal shocks on the low-power targets and avoid wasting RF power during the 0.1 ms gap in the bunch train.

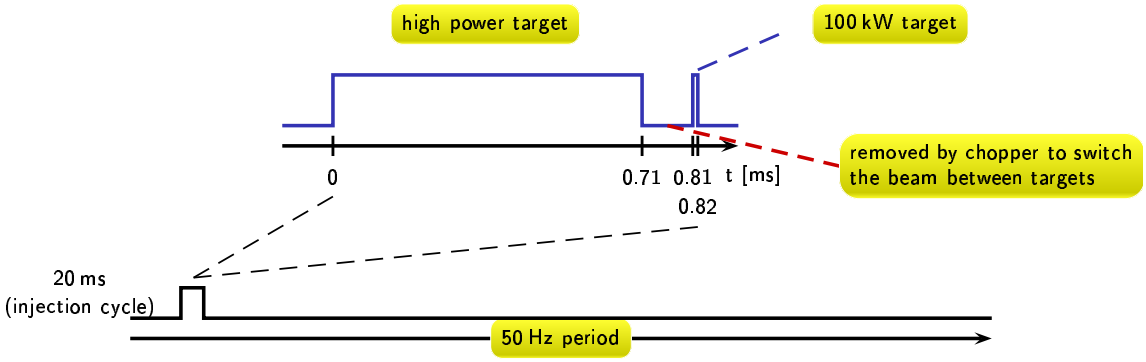

Fig. 2.2: Possible timing scheme for EURISOL operation

2.3 Progress in bulk-niobium superconducting cavities since CDR1

In CDR1 [3], the layout of the superconducting section was based on re-using decommissioned $\beta = 1$ elliptical cavities which became available at the end of 2000 after the shutdown of LEP. Since the development of the LEP cavities, significant progress has been made in the field of superconducting RF [17]. In particular, starting from the success of the procedures introduced for the mass production of LEP and CEBAF cavities, the TTF/TESLA Collaboration [18, 19] has in the past decade pushed the state-of-the-art superconducting RF technology of bulk-niobium cavities to new levels in terms of achievable accelerating gradients [20]. Moreover, the bulk-niobium technology has been successfully applied to the design of elliptical cavities for high-current proton accelerators for various applications, ranging from the Accelerator Production of Tritium (APT) at LANL [21] to nuclear waste transmutation in Accelerator Driven Systems (ADS) [22, 23, 24], neutron spallation sources (SNS) [25], and radioactive beam production (RIA) [26].

To cover the energy range from 120 MeV to 1080 MeV it was foreseen in CDR1 to develop three new families of medium-β elliptical multi-cell superconducting cavities using the same technology (niobium sputtered on copper, Nb/Cu) that was used for the LEP cavities. At the time this technology was preferred to bulk-niobium cavities because it promised higher stiffness for the operation in pulsed mode and because it was a well-established (and tested) technology at CERN. For the revised design, presented in this report, two families of 704.4 MHz bulk-niobium elliptical multi-cell cavities are foreseen for the superconducting portion of the linac. The technology of niobium sputtering on copper substrates—which has also evolved considerably since its use in LEP [27]—in principle has the perspective of achieving similar RF performances and cannot be excluded in terms of potential RF performances. However, the Nb/Cu technology requires more R&D activities focused on its adaptation and optimization to the reduced-β elliptical resonators, as clearly indicated by the extensive experience gained at CERN on several prototypes [28]. Moreover, for the medium-β structures the low-pressure operation at 2 K is likely to be needed both to reach low values for the surface resistance and to ensure a stable environment for operation. This need softens the perspectives of cost reduction of the Nb/Cu technology, usually dominated by the simplicity of operation at 4.2 K.

In addition to achieving high gradients it was also demonstrated that cavity vibrations and Lorentz-force detuning during pulsed operation can be reduced via stiffening and controlled with fast piezo tuners (e.g. [15, 29, 30]). As discussed in Section 4.3.4.1, the SPL superconducting linac design is based on achieving $E_{\mathrm{peak}} = 50$ MV/m and $B_{\mathrm{peak}} = 100$ mT on the cavity surface, values which are consistent with the performances of bulk-niobium structures reported by several laboratories [20, 31]. In the case of the SPL, two families ($\beta = 0.65$ and $\beta = 1.0$) of five-cell bulk-niobium elliptical cavities have been chosen to cover the energy range from 180 MeV to 3.5 GeV. Using the above-mentioned peak surface fields and the ratios of peak field over accelerating field, we assume accelerating gradients of 19 MV/m and 25 MV/m for $\beta = 0.65$ and $\beta = 1$ cavities.

2.4 Parameter choices and differences between CDR2 and CDR1

The current planning for the SPL foresees as a first step the construction of Linac4 [32, 33, 34, 35], which will replace the present Linac2 at CERN and which is designed to operate at the SPL duty cycle. For the construction of the SPL, Linac4 will be relocated in the SPL tunnel to serve as normal-conducting front end. The output beam energy of 160 MeV for Linac4 is chosen to reduce the space-charge forces at injection into the PSB by 50% compared with Linac2, and should thus allow the beam brightness out of the PSB to increase by a factor of 2 [36]. Since the foreseen $\beta = 0.65$ cavities have only poor acceleration efficiency at 160 MeV, it was decided to increase the normal-conducting section up to 180 MeV before starting with the superconducting part of the linac. The two families of SC cavities then accelerate the beam up to its final energy of 3.5 GeV. Figure 2.3 shows a block diagram of the linac and Table 2.1 lists the main layout parameters.

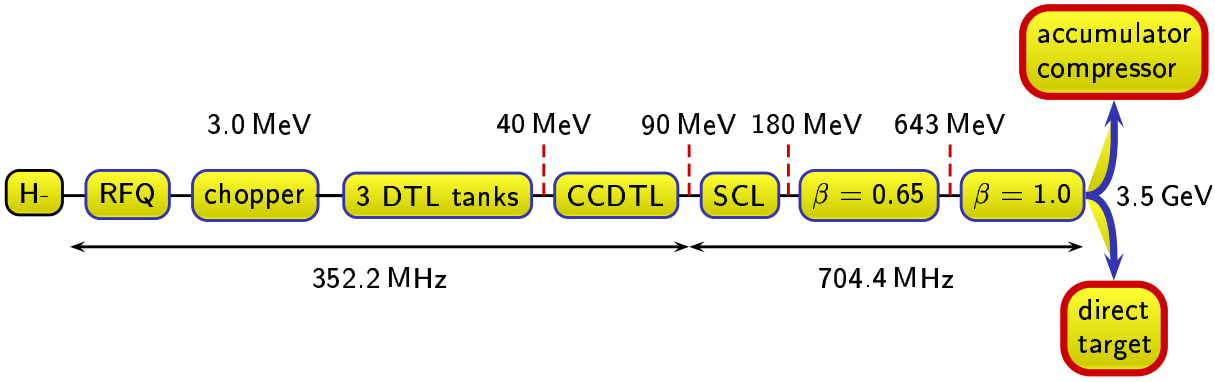

Fig. 2.3: Schematic layout of the linac

Table 2.1: Main layout parameters for all linac sections

Section	**Energy range** [MeV]	**No. of cavities**	**No. of accel. gaps**	**Peak RF energy** [MW]	**No. of LEP klystrons**†	**No. of new klystrons**‡	**Length** [m]
Source, LEBT	0.095	–	–	–	–	–	3
RFQ	0.095–3	1	560	1.0	1	–	6
Chopper line	3	3	3	0.1	–	–	3.7
DTL	3–40	3	85	3.8	5	–	13.6
CCDTL	40–90	24	72	6.4	8	–	25.5
SCL	90–180	24	264	15.1	–	5	34.9
$\beta = 0.65$	180–643	42	210	18.5	–	7	86
$\beta = 1.0$	643–3560	136	680	116.7	–	32	256
Total				161.6	14	44	429

† LEP klystrons: 352.2 MHz, 1 MW. ‡ New klystrons: 704.4 MHz, 4–5 MW.

The energy of 3.5 GeV is chosen as a compromise between the needs of a neutrino production target and the needs of a CERN-based EURISOL proton driver. Because of the higher beam energy and the higher mean current during the pulse, the pulse length could be reduced from 2.2 ms in CDR1 to 0.57 ms in CDR2 (comparing the 'neutrino' operation mode). The shorter pulse length eases the injection into subsequent rings and also relaxes the requirements on the H^- source. The average pulse current of 40 mA in the 'neutrino' operation corresponds to a peak bunch current of 64 mA after the chopper line and to $\approx$ 80 mA from the source. Beam dynamics studies showed that the space-charge

levels resulting from these currents are still acceptable for the low-energy part of the linac, yielding only moderate emittance growth in the area of the chopper line and the subsequent DTL. Since the klystrons are designed for operation at a 10% duty cycle, a wide range of machine modifications becomes possible without fundamentally changing the linac design: lower peak currents with increased pulse length (in case the H^- source is not able to deliver the required peak design currents), upgrades in beam power by lengthening the beam pulse, delivering two (or more) beam pulses within the same linac pulse (supply of different users at 50 Hz repetition rate), etc. It is also conceivable to add a second low-energy section (source, RFQ, chopper) with a proton source to add more flexibility (in terms of pulse length and peak current) for users which do not need H^- injection. With the compact layout of the SC section, energy upgrades become feasible at moderate cost (see Section 6.1).

Before every beam pulse, the SC cavities have to be 'filled' with energy in order to build up the required accelerating voltage. After the beam pulse when the klystrons are switched off, the stored energy decays and is reflected into the RF loads. During the 'filling' and 'decaying' process a large amount of RF power is reflected into the RF loads without being used for acceleration. The smaller SC cavities at 704.4 MHz at a cryogenic temperature of 2 K have reduced considerably the cavity filling (and decay) time. Using higher currents in the SC cavities increases the cavity beam loading and therefore reduces the loaded Q and thus lowers even further the filling time constant. In the normal-conducting section, higher currents increase the RF efficiency on account of a higher ratio of beam power over dissipated power. Taking all of these effects together, the average power consumption of the RF system for 'neutrino' (4 MW) operation could be reduced from 24 MW to 17 MW. At the same time, thanks to the lower cryogenics duty cycle, the power needed for the cryo-compressors could be reduced by more than 50%. The disadvantage of using higher currents is that higher RF peak power needs to be installed. However, considering that a) thanks to the development of fast phase and amplitude shifters (see Section 4.5.2.2), tetrodes are no longer needed for the medium-β SC section, and that b) purpose-built 704 MHz 5 MW pulsed klystrons are foreseen, rather than 352 MHz 1 MW CW klystrons from LEP, the overall number of RF systems could even be reduced. A full list of the general SPL operational parameters is given in Table 2.2 together with the major changes with respect to CDR1.

Table 2.2: Main linac parameters and changes from CDR1 to the revised design (CDR2)

	CDR1	**CDR2 (neutrino)**	**CDR2 (ISOL)**
Energy [GeV]	2.2	3.5	3.5
Length [m]	690	430	430
Average beam power [MW]	4	4	5
Average RF power† [MW]	24	17	21
Average cryogenics power [MW]	9.6	3.6	4.4
Repetition rate [Hz]	75	50	50
Beam pulse length [ms]	2.2	0.57	0.71 + 0.014
Average pulse current (after chopping) [mA]	11	40	40
Peak bunch current (after 3 MeV) [mA]	18.4	64	40
Beam duty cycle (after chopping) [%]	16.5	2.9	3.6
Injection turns (into ISR)	660	176	–
Peak RF power [MW]	32	162	162
No. of 352.2 MHz tetrodes (0.1 MW)	79	3	3
No. of 352.2 MHz klystrons (1 MW)	44	14	14
No. of 704.4 MHz klystrons (5 MW)	–	44	44
Cryo-temperature [K]	4.5	2	2

† Without 30% margin for Lorentz detuning.

The main differences with respect to CDR1 can be summarized as follows:

- energy increase by 60% and reduction in linac length by 45%;
- reduction in pulse length by almost a factor of 4;
- 30% lower RF power consumption, $>$ 50% lower cryogenics power consumption;
- higher RF peak power, from 32 MW to 162 MW;
- more flexible design in terms of pulse length, beam energy, pulse current;
- more design flexibility for accumulator/compressor rings;
- only two families of SC cavities instead of four;
- bulk-niobium SC cavities instead of Nb/Cu;
- higher RF frequency (704.4 MHz) from 90 MeV onwards;
- only one RFQ (95 kV–3 MeV, before the chopper line) instead of two RFQs (45 kV–3 MeV and 3 MeV–7 MeV, before and after the chopper line);
- higher transition energy between the normal and superconducting part of the linac, 180 MeV instead of 120 MeV.

Chapter 3

Applications

3.1 A neutrino facility at CERN

Recent ideas and developments in the USA [37], in the UK and in Japan [38] have made obsolete the initial CERN scenario. All schemes are still based on the use of muons produced by a high-power proton beam hitting a target, but promising new techniques are nowadays considered for capture and bunch rotation of the muon beam, as well as for muon acceleration. The analysis of these options is the subject of the International Scoping Study [39], which should end in 2006 with the selection of preferred scheme(s) and their comparative assessments.

The main evolution for the proton driver concerns the optimum energy, which is now estimated to be between 5 GeV and 10 GeV. The results of the HARP experiment [40] which are expected during the first half of 2006 will be crucial to refine this estimate. A superconducting proton linac like the SPL remains an excellent solution for efficiently providing a high-power proton beam at such energies. The specific time structure for the beam hitting the target will have to be obtained by an adequate design of the necessary ring(s) accumulating the linac burst and compressing the bunches. The details of the linac pulse sequence will also be tailored to these needs.

3.1.1 Neutrino physics objectives and facility considerations

The International Scoping Study (ISS) [39], currently being carried out by BENE (Beams for European Neutrino Experiments) [41], defines the physics potential of accelerator-based neutrino facilities as follows [41, 39]. Neutrino oscillations are now proven to exist and their mixing angles and mass differences should now be precisely measured. They may also permit the first observation of the Charge-conjugation Parity (CP) symmetry in the leptonic sector and provide support to the concept of a CP-violating mechanism (leptogenesis) by which the antimatter was removed from the early Universe. Massive neutrinos may also play an important role in the formation of large-scale structures in the Universe. Precision measurements of neutrino oscillations are required to develop a complete description of the properties of the neutrino and to elucidate the mechanisms that give rise to neutrino mixing and neutrino mass.

Two facilities are under consideration.

- A neutrino factory, based on a high-brilliance muon beam aiming high-energy electron neutrinos (up to 20–50 GeV) at magnetic detectors $\approx$ 700–7000 km away. This facility is the preferred tool to perform high-precision unambiguous measurements of oscillation parameters, neutrino mass hierarchy, CP violation and tests of universality in the neutrino sector.
- A neutrino beta-beam facility [1] in combination with a conventional muon-neutrino beam (superbeam) [2] of the same energy. The beta-decay of specific ions would provide a very clean beam of electron (anti)neutrinos up to $\approx$ 2 GeV. The large detectors that are required may be the same as those needed for proton decay and astrophysical neutrinos. Together with a superbeam, beta-beams could provide interesting sensitivity in the search for leptonic CP and T violation.

Both options would extend considerably the knowledge of neutrino masses and mixings and offer appreciable synergies with other fields within and outside particle physics. Precision measurements of neutrino mixing angles and mass hierarchy provide a very strong physics case, independent of the explorations at high-energy colliders.

3.2 Radioactive nuclear beam facility

Radioactive Ion Beams (RIBs) can be produced either by the ISOL (Isotope Separator On-Line) method or by the complementary 'in-flight' method. The proposed new infrastructure EURISOL [12], the next-generation ISOL RIB facility in Europe, aims at the provision of high-intensity beams of radioactive nuclei with variable energy, from a few keV to greater than 100 MeV per nucleon. These beams of exotic ions will be orders of magnitude more intense than those currently available. EURISOL will provide a facility for research that addresses the major challenge of the fundamental understanding of nuclear structure in terms of the underlying many-body interactions between hadrons. Descriptions of nuclei having more than a few nucleons are semi-phenomenological in origin and cannot be reliably applied to nuclei far from stability. It is therefore crucial to measure the properties of nuclei at the extremes of stability such as the evolution of shell structure, $T = 0$ and $T = 1$ pairing, and collective phenomena such as halo effects and pygmy resonances.

3.2.1 EURISOL physics objectives

EURISOL also aims at understanding the Universe through its history of stellar activity and galaxy formation where nuclear reactions play essential roles. In particular, in the violent maelstrom of explosive processes such as novae, X-ray bursters and supernovae, the heavy elements are made in complex networks of reactions (r- and rp-processes) on unstable nuclei and beta decays. To understand these processes quantitatively and identify the astronomical sites where they occur requires a wealth of information on unstable nuclei. EURISOL, with its broad range of beams, will allow us to study many of the key reactions. Further applications of EURISOL to fundamental tests of the Standard Model, to the application of unique probes for surface science and condensed matter studies, and to other fields can be found in the report for EURISOL prepared within the RTD contract in the Fifth Framework programme [42]. EURISOL will have applications that benefit society in many different areas and have strong impact on other fields of science, as illustrated in the NuPECC reports of the Working Groups *Impact, Applications and Interactions of Nuclear Science* [43].

A capability of EURISOL that has been recently identified is the beta-beam facility, which will address the main challenges of neutrino physics: the measurement of the mixing angle Θ_{13} of the Maki–Nakagawa–Sakata–Pontecorvo matrix (a fundamental parameter of the Standard Model of interactions) and the search for CP violation in the lepton sector. These measurements, which require intense neutrino beams of defined flavour accompanied by large detectors located at a distance corresponding to the maximum of the observed oscillations, will provide the key ingredient of leptogenesis scenarios for explaining the matter–antimatter asymmetry in the Universe.

3.2.2 The EURISOL facility

Historically, nuclear science has progressed through the application of numerous complementary investigative techniques to a broad range of nuclear species. EURISOL will allow European scientists to apply this heritage to vast—hitherto unexplored—regions of the nuclear chart made accessible through the development and implementation of challenging novel techniques. The EURISOL facility will provide a uniquely broad range of radioactive ion beams with intensities on average three orders of magnitude larger than current ISOL installations and with unrivalled flexibility in final energy between a few eV and 100 MeV/nucleon. In this energy domain, unmatched beam quality will be offered so that our knowledge of nuclei far out towards the drip-lines can approach the precision of that of the stable nuclei. This advancement of performance compared to present-day ISOL facilities will be accomplished through major technical breakthroughs concerning several key components.

– Unequalled primary beam power of 5 MW protons of up to a few GeV energy, as well as heavy ions of $A/q = 2$ up to $500\,A$ MeV and possibly also ions with $A/q = 3$ or larger up to $100\,A$ MeV.

– A choice of newly designed production targets: (a) a direct target accepting up to 100 kW beam intensity; (b) a multimegawatt target station based on Hg liquid proton-to-neutron converter and UCx production target; a high-Z solid converter will also be investigated.
– A CW linear post-accelerator for heavy ions delivering a continuous choice of energies up to 100 MeV/nucleon. This will also permit fragmentation of the RIBs to produce even more exotic, neutron-rich nuclei.

Based on the EURISOL RTD report, one may expect final intensities of approximately 10^9 pps of ^{11}Be or 10^{12} pps of ^{132}Sn after post-acceleration, for example.

3.2.3 The EURISOL design study

The European Union is supporting a design study for EURISOL within the Sixth Framework programme. The study started on 1 February 2005 and will run until the end of 2008. It will result in a technical design report for the facility and, in addition, a conceptual design report will be delivered for the beta-beam facility. In total 21 research institutes and universities are participating in the study, which has a total budget of €32 million with €9 million coming from the European Union. In addition, 21 institutes and universities are participating as contributors.

3.2.4 The SPL as EURISOL driver accelerator

For EURISOL it is proposed to operate four target stations in parallel: three low-power (< 200 kW), direct proton-target stations and one high-power (5 MW) two-stage spallation neutron target station. The primary proton beam incident on such a facility will be required to meet constraints imposed by the characterization and operation of these target stations, their lifetime and the sharing of the primary beam between targets. The SPL provides many features that are compatible with the EURISOL primary proton beam.

Important considerations when choosing beam parameters are target stability and lifetime. All four targets would benefit from continuous beam operation, with smooth, constant proton-beam currents. In practice, proton beams are pulsed and deposit energy within the target volume in short bursts leading to thermal shocks and shock-wave effects which affect the target lifetime. Targets can be heated to mitigate the damage caused by thermal shocks. A drop in incident beam power can then be compensated for by an increase in target heating, although this can only be done on timescales much larger than the pulse length. It is important to design a system where the deposition of energy in the targets is as constant in time as possible.

Experience of operating targets at ISOLDE under pulsed proton-beam conditions can help to place limits on the type of pulse that could be acceptable. The following arguments for a 1 ms pulse width were arrived at independently for the development of EURISOL targets:

– suited for measurements of release properties of targets,
– reduced thermal stress on the 5 MW target,
– equivalent to the amount of energy delivered currently at ISOLDE over 920 ns,
– suited for operation as a 5 kW average beam if necessary, with one pulse every 1 s.

At any given time the high-power target station will be operated continuously in parallel with one or two of the low-power targets. This is the most likely scenario since the low-power targets need to be changed every three weeks, so that every week one of the three low-power target stations will be out of action whilst the used target is removed and a new target is installed. The most convenient way of switching between the high-power target station and one of the low-power target stations involves switching within a given pulse. Assuming an SPL pulse of 0.82 ms, the high-power target would receive a bunch train for 0.71 ms, which would be followed by a gap of 0.1 ms during which the pulse would

be switched to a low-power target for the remaining 14 μs. This implies a change in the microstructure originally planned for SPL, where a pulse consisted of 2×10^5 bunches organized in 2.5×10^4 cycles of eight bunches, with five filled bunches and three empty bunches. For EURISOL, the modified pulse structure would consist of $\approx 2.5 \times 10^5$ filled bunches sent to the high-power target, followed by $\approx 3.5 \times 10^4$ empty bunches during which the beam is switched to the low-power target, and finally $\approx 5 \times 10^3$ filled bunches sent to the low-power target as depicted in Fig. 2.2.

The operation procedure for targets will include an initial period during which the target is exposed to short bursts of a fraction of the total proton-beam power for which it is rated (Fig. 3.1). This initial period is required for target characterization where release and yield measurements for various isotopes are undertaken and the burst width and time between consecutive bursts would be determined by the release, effusion, diffusion and half-life of the particular isotope to be analysed. Target characterization can then be followed by target warming-up with a ramping up of the beam power to its final nominal value for operation. Some flexibility of the primary proton-beam power will therefore be required. Under the current scheme, the direct (low-power) target will receive a 14 μs pulse with an associated instantaneous power deposition of 143 MW. This could be reduced by introducing partial laser stripping of the long pulse to feed a fraction of the 0.71 μs pulse to the direct targets, leading to the same average power but a factor 50 lower peak power deposition.

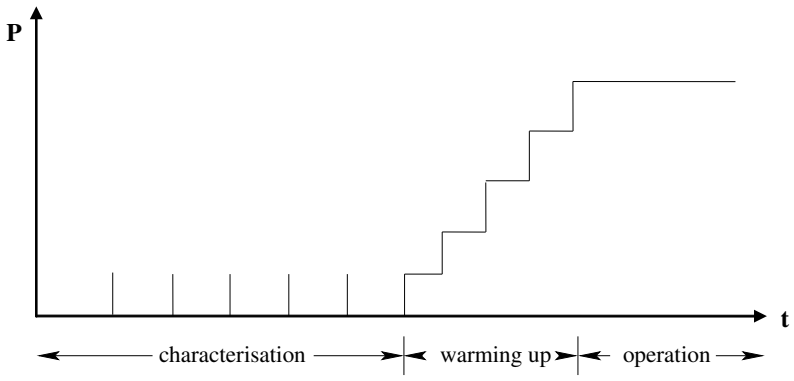

Fig. 3.1: Operation of a target at EURISOL

Lowering of the beam power can be achieved, for example, by reducing the number of pulses incident on the target, by decreasing the pulse length, by altering the pulse microstructure, by reducing the proton energy, or by reducing the beam current. A reduction in the beam current (by a factor 10) is the most favourable scenario for targets, although this is difficult to achieve in practice. It is more likely that either the length of the pulse will be adapted or the low-energy beam chopper will be used to reduce the average current during the pulse.

3.3 LHC upgrade and other CERN applications related to PS injection

3.3.1 PS injection and beam dynamics

Modifications limited to the hardware handling the injection process are sufficient for the PS to benefit from the SPL beam. These have been described in a previous report [44] and mostly involve removing the present 1.4 GeV fast injection system and replacing it with a charge-exchange injection set-up in straight section 78.

The SPL will supply H^- to the PS with a repetition rate of $\approx$ 1 Hz, meaning that only one pulse in 50 is sent to the PS for the needs of the CERN complex of high-energy accelerators. The duration of these pulses and their fine time structure are completely defined by the PS needs for each specific cycle in the PS super-cycle. Most SPL beam pulses therefore remain available for high-power users like EURISOL or a neutrino facility. As outlined in Chapter 2, the low-energy beam chopper can be

used to modify the time structure of the linac pulses and it thus becomes possible to supply pulses to the PS with up to ≈ 0.7 ms length and average pulse currents of up to 40 mA. Furthermore the chopper can be used to 'cut' a gap into the otherwise continuous bunch train long enough to switch the high-energy beam to different users (e.g., the existing ISOLDE facility at CERN, compare also the foreseen EURISOL operation scheme in Fig. 2.2). This means that more than one user can be supplied with a 50 Hz repetition rate and with different beam power levels.

The main limitation of the PS machine for high-intensity, high-density beams comes from space-charge detuning at low energy [45], given by

$$\Delta Q_{x,y} \propto \frac{I_\mathrm{p}}{\varepsilon^*_{x,y}\beta\gamma^2} \tag{3.1}$$

where $\Delta Q_{x,y}$ is the incoherent (self-field) detuning in the horizontal (x) and vertical (y) planes, I_p is the bunch peak current, $\varepsilon^*_{x,y}$ are the normalized emittances, the ratio $I_\mathrm{p}/\varepsilon^*_{x,y}$ is the beam brightness, and β and γ are the usual relativistic factors. As an injector for the PS machine, replacing the present Linac2 and PS Booster, the SPL increases the minimum energy in the PS from 1.4 GeV to 3.5 GeV, which reduces the space-charge detuning $\Delta Q_{x,y}$ by a factor of 3.8 (instead of 1.9 for CDR1 [3]). The beam brightness $I_\mathrm{p}/\varepsilon^*_{x,y}$ can then be quadrupled while keeping the same $\Delta Q_{x,y}$. This means that the space-charge detuning at injection is no longer a limitation for the acceleration of high-intensity, high-brightness beams in the PS.

H^- injection allows control (by painting) of the particle density in the transverse phase planes. The fast chopper at the SPL front end gives the possibility to optimize the population of the longitudinal phase plane, and in particular to use the harmonic number and the number of bunches that are best matched for each specific PS beam user.

3.3.2 Performance improvement for the LHC

A higher space-charge tune shift than in the nominal scheme using the PSB [46] can be tolerated because the beam stays a much shorter time at the injection energy (the 'ultimate' intensity is accumulated in $\approx$ 30 turns or 60 ms instead of 1.2 s when using the PSB). Combined with the gain resulting from the higher injection energy (see Section 3.3.1), we extrapolate from a previous study [45] that the ultimate intensity for the LHC can probably be achieved with a transverse emittance smaller than 1 π mm mrad (rather than the present 3 π mm mrad). The brilliance, at the PS exit, will then be up to four times higher than nominally specified [46], which makes it compatible with all foreseen scenarios of LHC luminosity upgrade, although other limitations in the PS are likely to become dominant (collective effects like instabilities, to be addressed with aggressive damping systems). The main beam parameters at the injection energy in the PS are summarized in Table 3.1.

Table 3.1: Tentative parameter list of LHC 'ultimate beam' at low energy in the PS machine at $W = 3.5$ GeV, $V_\mathrm{RF} = 50$ kV, $h = 21$ (only 18 buckets filled), $N_\mathrm{t} = (h-3)N_\mathrm{b} = 1.5 \times 10^{13}$ protons per pulse, assuming 8% transmission to the LHC

N_b [10^{11}]	ε_l [eV s]	τ_b [ns]	ε^*_x [π mm mrad]	ε^*_y [π mm mrad]	ΔQ_x	ΔQ_y
8.5	0.6	60	1	1	0.12	0.2

The fast PS filling process also has the advantage of reducing the PS cycle length from 3.6 s to 2.4 s, which shortens the injection flat-top in the SPS from 7.2 s to 4.8 s and reduces the LHC filling time accordingly.

3.3.3 Performance improvement for SPS fixed-target physics

With the same arguments as for the LHC beam (see previous section), we estimate that the transverse emittances of a PS beam of, for example, 4×10^{13} protons will be $4\,\pi$ mm mrad in the horizontal and $6\,\pi$ mm mrad in the vertical plane (at present $17\,\pi$ mm mrad and $7\,\pi$ mm mrad, respectively) while keeping the tune shifts around 0.1. This will eliminate one of the major limitations for achieving a higher intensity (e.g., for the CNGS beam) in the SPS machine which comes from the limited SPS transverse acceptances at injection energy. The estimated parameters for this beam at injection energy in the PS are given in Table 3.2.

Studies aimed at a new type of 'continuous-transfer' extraction to reduce the high losses currently related to this operation have been fully demonstrated and are now giving the possibility to increase beam intensity without irradiating the accelerators equipment more. The complete operational implementation is expected to take place before 2009.

Table 3.2: Tentative parameter list of a high-intensity SPL beam at low energy in the PS machine at $W = 3.5$ GeV, $V_{\mathrm{RF}} = 50$ kV, $h = 16$, $N_{\mathrm{t}} = hN_{\mathrm{b}} = 4 \times 10^{13}$ protons per pulse

N_{b} [10^{12}]	ε_{l} [eV s]	τ_{b} [ns]	ε_x^* [π mm mrad]	ε_y^* [π mm mrad]	ΔQ_x	ΔQ_y
2.5	0.8	75	4	6	0.11	0.11

3.3.4 Performance improvement for the high-intensity beams used by nToF and AD

Keeping acceptable tune shifts (0.24 in both planes), the nToF bunch intensity can be increased to 10^{13} protons per pulse (ppp) (0.7×10^{13} at present) by adjusting the horizontal and vertical emittances to $6\,\mu$m and $8\,\mu$m, respectively. Note that for this beam the longitudinal emittance should not be made smaller than 2.8 eV s to avoid beam break-up instabilities at transition and not higher than 3 eV s to maintain a short bunch at extraction. The intensity of the antiproton beam could also be increased to 2×10^{13} ppp (at present: 1.5×10^{13}).

3.3.5 Other advantages and potential improvements

The high proton flux and the fast cycling rate of the SPL decouples the PS and the ISOLDE operations. The PS does not compete with ISOLDE for particles from the injectors, in contrast to the present situation with the PSB.

Using the SPL as the injector, the PS is no longer linked to the present linac and PSB repetition rate (i.e., multiples of 1.2 s), and in principle magnetic cycles of 'any length' can be envisaged. This should bring some gain in the duty factor of the PS by reducing the dead time between cycles. However, a significant improvement can only be achieved if the $\mathrm{d}B/\mathrm{d}t$ in the bending magnets is noticeably increased, which implies major hardware changes.

The most interesting solution to get the full benefit of the SPL for high-energy physics is to equip the PS with a new synchrotron, optimized for injection at 3.5 GeV and accelerating up to 50 GeV. Such a new accelerator is currently under study [47]. It would solve the problem of ageing PS components and remove the bottleneck at injection in the SPS, preparing for LHC luminosity (and possibly energy) upgrades.

Chapter 4

Design

4.1 Main design choices

The choice of technologies is closely related to the parameter choices in Chapter 2, the technological feasibility of accelerating structures, as outlined in the following sections, and the possibility to re-use equipment from CERN (e.g., LEP RF) or other sources (e.g., IPHI RFQ). While the technology of the superconducting section completely changed from CDR1 to CDR2, the main technological choices for the normal-conducting section (up to 90 MeV) remain valid.

Any modern high-intensity linac injecting into a circular machine relies on H^- charge-exchange injection and implies the use of an H^- source. Moreover, a low-energy beam chopper is required to reduce capture losses during the ring injection. For the H^- source development at CERN, it was decided to further develop the existing DESY RF volume source (Section 4.2.1), improving its performance to reach the SPL specifications. After a magnetic LEBT (two solenoids), an RFQ accelerates the beam from 95 keV to 3 MeV. It is foreseen to re-use the RFQ of the French IPHI Collaboration (Section 4.2.2). Originally foreseen for CW operation, this device is under construction and will be tested first in France and then at CERN in the 3 MeV test stand [48] which is currently being prepared. Following the RFQ a beam chopper allows gaps to be created in the bunch train corresponding to the transitions between RF buckets of a subsequent circular machine, reducing the injection losses to tolerable levels. In order to avoid partially filled bunches which can yield losses in the linac itself, the rise-time for the deflecting field has to be less than 2 ns. Furthermore the chopper can also provide gaps for the ring ejection kicker, and/or gaps which allow fractions of the full energy beam to be deflected to different users (see the proposed EURISOL operation scheme in Section 2.2). A performance test of H^- source, LEBT, IPHI RFQ, and chopper is foreseen partly within the European HIPPI Collaboration [50, 49] and then in a dedicated 3 MeV test stand at CERN [48].

The RF frequency of 352.2 MHz for the normal-conducting part of the linac is determined by the existing LEP klystrons. From 90 MeV onwards, 704.4 MHz klystrons are foreseen to power the normal-conducting Side Coupled Linac (SCL) up to 180 MeV. From there, 704.4 MHz superconducting elliptical multi-cell cavities raise the beam energy up to its final value of 3.5 GeV. The higher frequency reduces the size (and cost) of the structures. It allows higher RF gradients to be used in the SCL and it is well suited for bulk-niobium cavities in the superconducting part.

After the chopper line, a classic Alvarez Drift Tube Linac (DTL) is used to accelerate the beam to an energy of 40 MeV. Because of the demands of high current and low losses, short focusing periods are imperative in this energy range. Having its maximum shunt impedance at around 20 MeV, a DTL is considered the most suitable structure for this section (see also Section 4.3.1). From 40 MeV onwards, longer focusing periods can be accepted and one can separate the quadrupoles from the RF structure. This measure slightly raises the 'real estate' shunt impedance and, more importantly, simplifies considerably the construction and alignment of the structures. Therefore a Cell-Coupled DTL (CCDTL) was chosen to cover the energy range from 40 MeV to 90 MeV (Section 4.3.2). At higher energies, drift tubes in DTL-type structures become very long and it becomes more efficient to use RF structures with a gap distance of $\beta\lambda/2$ rather than $\beta\lambda$ as used in DTL-type structures. Switching at the same time to a higher frequency, the structures become small enough, so that they can be machined out of solid copper at a reasonable price. For the SPL baseline design an SCL was chosen to accelerate the beam up to 180 MeV. However, as the construction is still relatively expensive and since the shunt impedance that can be reached is still relatively low (see Section 4.3.3), it is of interest to consider a superconducting alternative for future revisions of the design. Above 180 MeV the technology of superconducting bulk-niobium elliptical multi-cell cavities is well established (see Sections 2.3, 4.3.4.1), and considered to be

the most economical approach to reach high-intensity, high-energy beams. For the SPL it is foreseen to use two families of five-cell elliptical cavities ($\beta = 0.65$, and $\beta = 1$) to cover the energy range from 180 MeV to 3.5 GeV. This approach will reduce the amount of R&D as well as the production costs for these structures.

Transfer lines transport the beam from the linac to the various users (i.e., the PS machine, an accumulator/compressor ring, ISOLDE/EURISOL). At 3.5 GeV a minimum bending radius of ≈ 200 m has to be observed for these lines to keep H^- stripping at an acceptable level (see Section 6.1). An additional design constraint may be considered for the operation as a EURISOL driver: depending on future target studies it may be desirable to extract a fraction of the beam at lower energy. In this case one can use fast kickers at the energy level in question and divert part of the beam to a transport line running in parallel to the main linac. This option has not been studied in full detail but is considered to pose no significant technical challenge.

4.2 Front end

4.2.1 H^- source and low-energy beam transport (LEBT)

Today there are two major types of H^- source: surface and volume sources. A review of their technical principles, advantages and disadvantages is given in Ref. [51]. Not all of these ion sources are well suited for accelerator operation where intensity, short- and long-term stability, reliability, and easy maintenance are of major importance. Reference [52] gives an overview of operational sources and source developments for high-intensity accelerators.

The technology of existing sources raises a number of questions. In many cases caesium is used to produce high H^- currents, but caesium pollution of the beam can give rise to voltage holding problems in the following accelerator structures. And the caesium injection lines can be clogged by caesium hydride, leading to lifetime limitations. The source emittance is defined mainly by the source structure and the principle of the H^- creation and can only be influenced to a small extent. For a fully optimized source there is a lower limit of the emittance that can only be overcome by cutting the beam intensity at the same time. The lifetime of filaments, cathodes or antennas inside the plasma chamber is a limiting factor for the reliability.

The requirements of 80/40 mA H^- current, 0.57/0.8 ms beam pulse, 50 Hz repetition rate, and 0.25 π mm mrad normalized r.m.s. emittance for neutrino/EURISOL operation cannot be met by one of the existing operational sources. For the H^- source development at CERN, it was to decided to start with an existing successful source design like the DESY RF volume source (Fig. 4.1) [53, 54] and then try to improve the design up to the SPL specifications.

The DESY source routinely delivers 40 mA of H^- at an extraction voltage of 35 kV. The present pulse length is 0.1 ms, the repetition rate 5 Hz and the emittance 0.18/0.16 π mm mrad (r.m.s. normalized). The source runs without caesium and has a lifetime of up to 25 000 hours. Currents of 54 mA have already been extracted in experimental set-ups [53]. At the moment the pulse length is limited by the available RF generator. Further tests will show if there is a physical limit to get longer pulses. A collaboration with DESY has to be set up to exchange information and knowledge about the source. Development work of other groups with similar source types (e.g., at SNS) will also supply a valuable input. To meet the SPL duty cycle specifications a major re-design will be necessary (e.g., for the source cooling).

Since the extraction voltage of the DESY source is lower than the 95 kV necessary for the injection into the IPHI RFQ, there are two possible ways to adapt the source. The first would be a re-design of the extraction system for 95 kV and the second, and so far more favourable one, is post-acceleration from 35 kV to 95 kV.

The source and the LEBT have to be considered together from the early design stage. Two-solenoid LEBT designs as for the CERN RFQ2 injector [55] are well proven and allow a precise matching

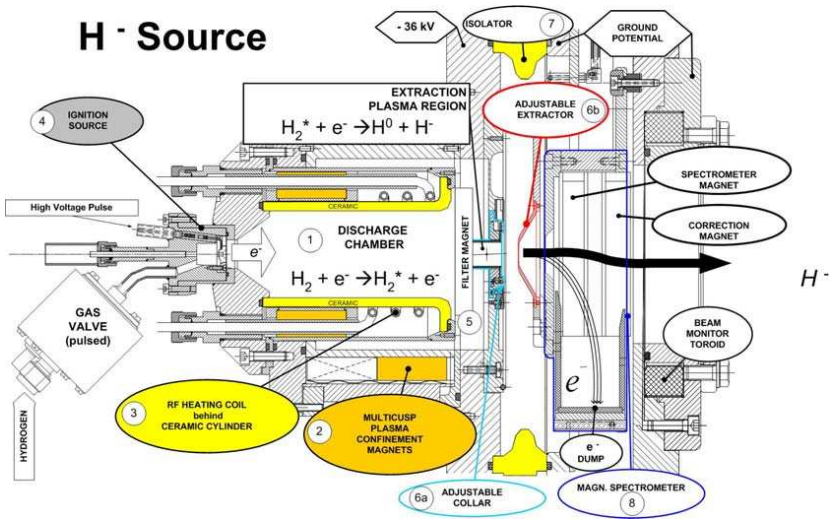

Fig. 4.1: The DESY volume H^- source [54]

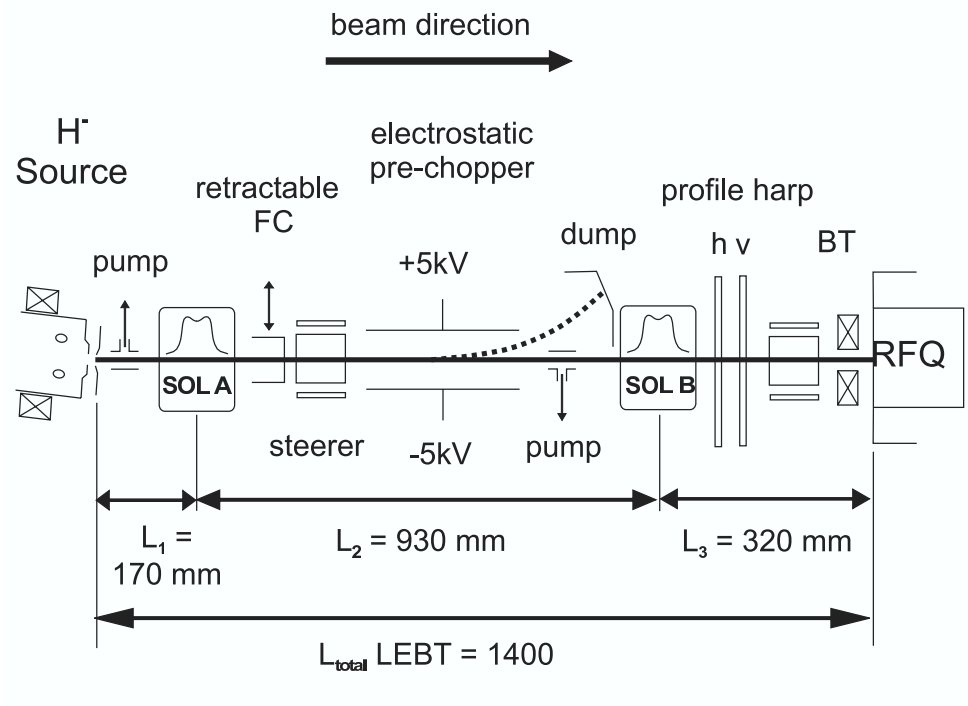

Fig. 4.2: LEBT scheme [56] (FC – Faraday cup, BT – beam transformer)

to the RFQ, leaving enough space in the line for beam diagnostics and other equipment. A pre-chopper for shaping the pulse at low energy may also be necessary.

A possible design for the Linac4 LEBT based on available equipment (two solenoids and their power supplies) is shown in Fig. 4.2 [56]. The LEBT for the SPL will need new DC magnets and the design has to be based on the final SPL H^- source and experience with the Linac4 LEBT. With a pressure in the range of 10^{-5} mbar, space-charge compensation in excess of 90% should be achieved, leading to a transverse emittance growth of only 2%. However, at this pressure, stripping losses of $\geq$ 8% have to be expected. The gas pressure and type can be optimized to maximize the transmission to the RFQ within its acceptance.

4.2.2 Radio frequency quadrupole (RFQ)

After the ion source and the LEBT, an RFQ will perform the beam capture and bunching and will accelerate the beam from 95 keV to an energy of 3 MeV which is considered as the optimum for beam chopping. The IPHI (Injecteur de Protons de Haute Intensité) RFQ that is foreseen for operation in Linac4 and the SPL is the result of a CEA and IN2P3 joint effort to develop a CW injector [57] for high-intensity applications. A collaboration agreement has been signed with CERN, specifying that the RFQ will be transferred to CERN after high-intensity tests with a proton source at CEA Saclay. The RFQ, which operates at 352.2 MHz, is 6 m long and consists of three segments that are resonantly coupled by means of two coupling cells. Each segment is built with two modules of 1 m length that are mechanically coupled to each other (Fig. 4.3). The end of the third segment, the RFQ output, houses a fringe field cell.

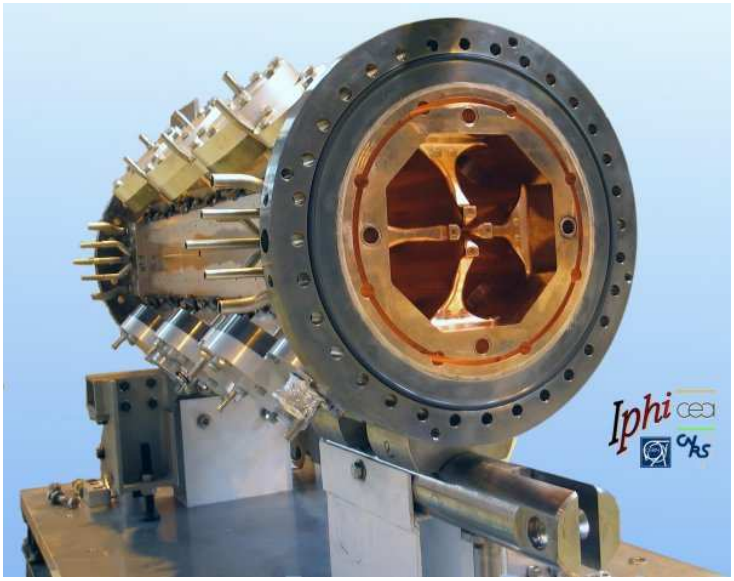

Fig. 4.3: One of six modules of the IPHI RFQ

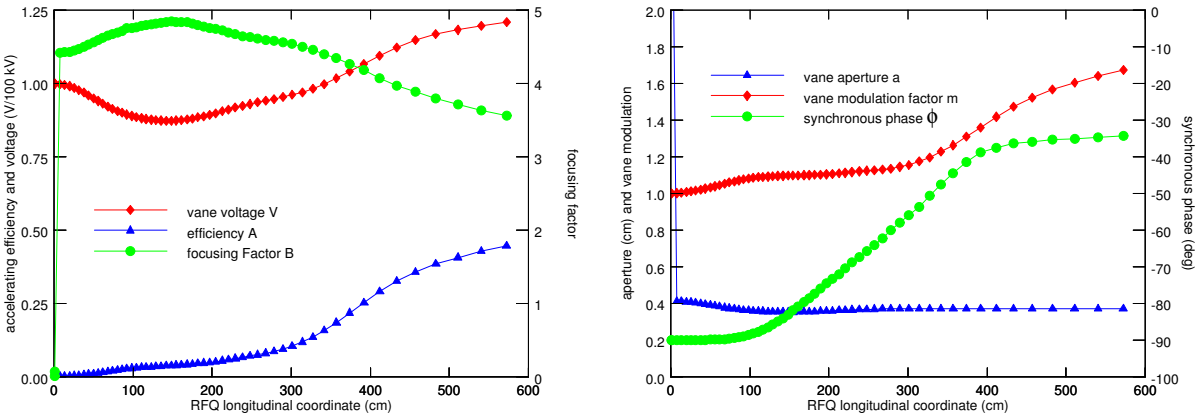

Fig. 4.4: (a) Vane voltage, acceleration efficiency, and focusing factor; (b) aperture, modulation, and synchronous phase

The evolution of the main parameters all along the RFQ is shown in Figs. 4.4 (a) and 4.4 (b). The vane voltage varies between 87 kV and 122 kV in order to keep the surface field at a constant value of

31 MV/m (1.7 kilpatrick) all along the structure. The RFQ has been designed for 100 mA beam current and, in order to assure the best beam transmission, the 'gentle bunching' section extends over most of the accelerator length. For the SPL current requirements of ≈ 70 mA, 99.5% of the beam is transmitted (see Fig. 4.5). The overall power dissipation within the pulse is depicted in Fig. 4.6, assuming a maximum beam current of 70 mA to be accelerated within the pulse.

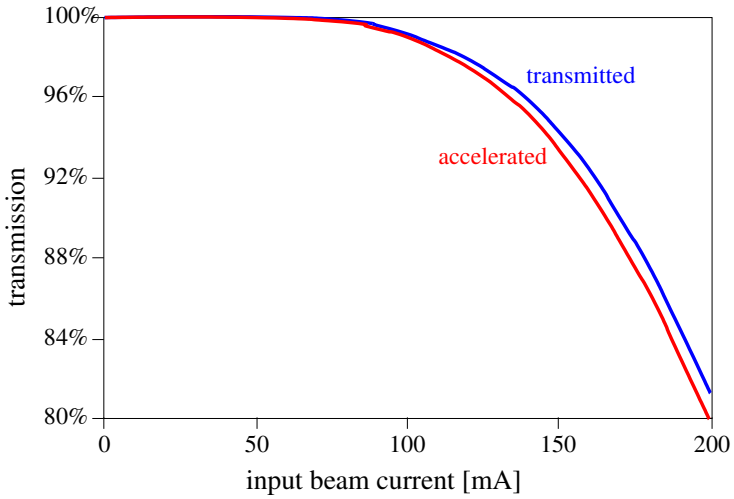

Fig. 4.5: Transmitted and accelerated beam in the RFQ as a function of the input beam current

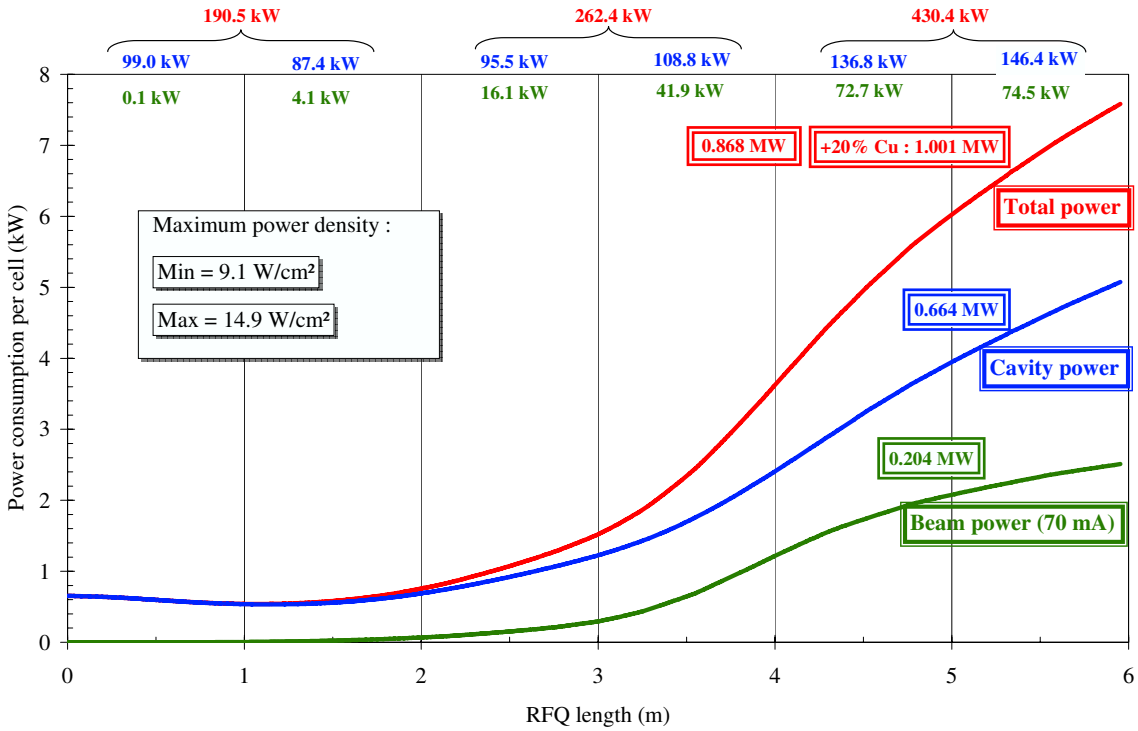

Fig. 4.6: Power consumption as a function of the RFQ length. The power dissipated in copper (based on SUPERFISH simulation) and the beam power are detailed at the level of the module.

In order to minimize the impact on the beam dynamics, the presence of multi-polar components in the focusing field has been studied with PARMTEQM. The ratio between the dipole component of the

field, responsible for the beam defocusing, and the main quadrupole mode in the RFQ cavity has been kept below 4.5%. The length of the RFQ requires that the resonator be split into three resonantly coupled segments. The two coupling cells, placed every two metres, are critical for the beam dynamics, since in this area the electric field is 5–10% lower with respect to the adjacent vanes. The small emittance growth, which can be observed in the RFQ, is located around these coupling cells. Nonetheless, the perturbation of the beam remains localized and the multiparticle simulations performed with LIDOS.RFQ [58] do not show any relevant deterioration of the beam characteristics at the RFQ output. A summary of the main RFQ parameters can be found in Table 4.1.

Table 4.1: Main RFQ characteristics

Frequency	352.2 MHz
Total length	5.954 m
Electrical length	7 λ
Number of resonating segments	3
Number of coupling cells	2
Number of cells	560
Aperture radius	3.721–4.129 mm
Modulation	1.00–1.6923 m
r_0	3.69–5.139 mm
Vane voltage	87.32–121.61 kV
Peak electric field	1.7 kilpatrick
Power in copper (SUPERFISH + 20%)	808 kW
Beam power	210 kW
Total power	1018 kW

4.2.3 Low-energy beam chopping

The beam chopper has to establish the required micro-pulse structure by deflecting part of the RFQ output beam onto a dedicated beam dump. The structure is located between the RFQ and DTL, both operating at 352.2 MHz, and the transfer energy of 3 MeV has been chosen as a compromise between the demands of beam dynamics and the chopper amplifier. While lower beam energies reduce the voltage requirements for the chopper amplifier, they increase the space-charge forces and generally yield more emittance growth. The bunches are spaced by 2.84 ns and come in 0.57 ms pulses repeated at 50 Hz, which means that in order to avoid partially chopped bunches the chopper rise-time has to be of the order of 2 ns (assuming a maximum bunch phase length of $\pm 45^\circ$ at 352.2 MHz). The deflector itself consists of two 50 Ω transmission lines facing each other, which are driven by two pulse amplifiers with opposite polarity signals (500 V).

The most challenging mode of operation is foreseen when the SPL injects into an accumulator and compressor ring. To avoid losses at injection and assuming a 44 MHz RF frequency in the ring, the chopper has to remove three out of eight bunches, while for Linac4 the chopper has to provide repetition rates of $\approx$ 1 MHz. For operation in EURISOL mode a section of $\approx$ 0.1 ms has to be removed from each linac pulse. In all modes of operation the chopper can also be used to remove the first 20–30 μs of the pulse, which are generally not very stable during the start-up of the source.

A 3D technical drawing of the chopper line is shown in Fig. 4.7. The elements of the complete line are (from left to right, downstream) matching section (four quadrupoles plus buncher cavity), beam chopper (two quadrupoles with chopper plates inside), buncher cavity plus quadrupole plus dump (for the chopped beam), matching section (four quadrupoles plus buncher cavity).

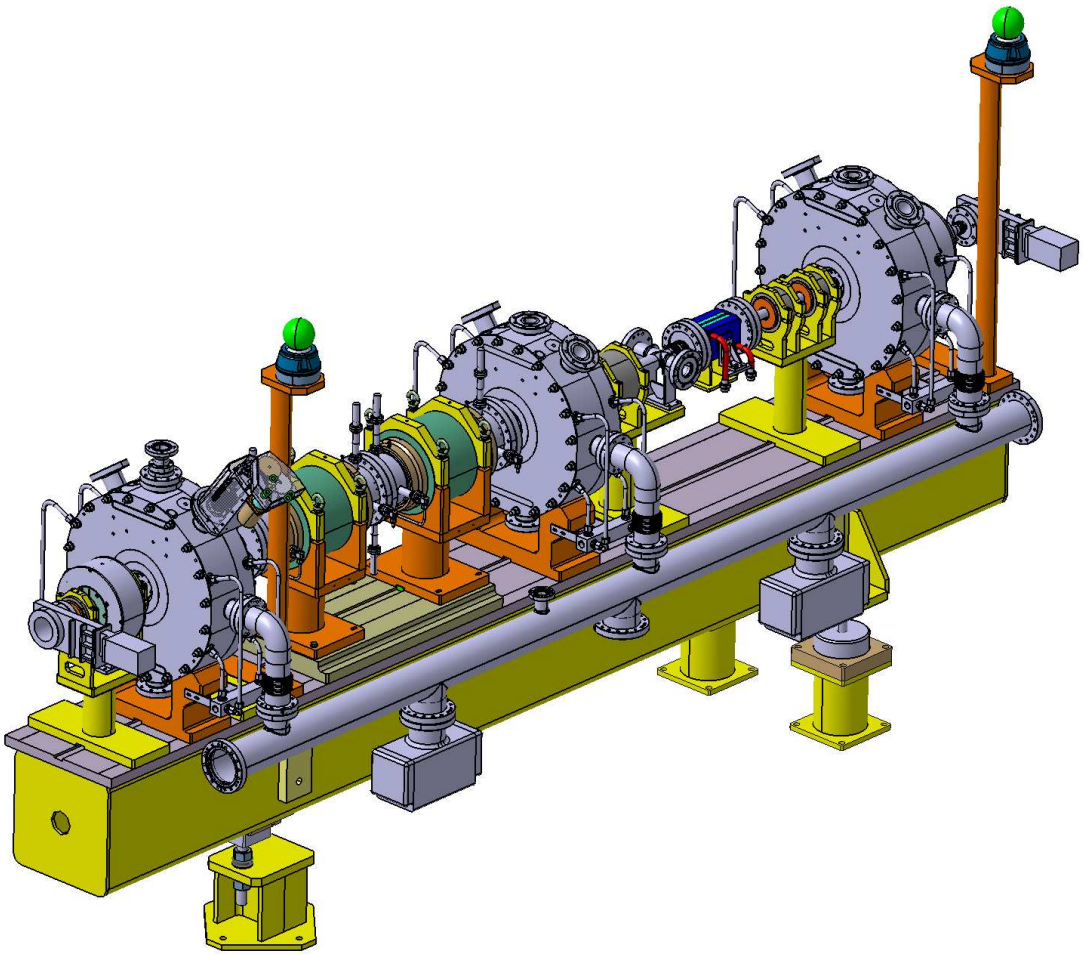

Fig. 4.7: 3D image of the chopper line with support structure

The beam dynamics of the entire CERN chopper line is designed to minimize the plate voltage by increasing the deflection via beam optics (see Section 4.4.4, Fig. 4.29). On the other hand, there is an effort to keep the actual chopper structure as short as possible in order to minimize emittance blow-up during long drifts. At present a 3 MeV test stand is under construction at CERN [48], comprising an H^- source, the IPHI RFQ (see previous section), and the complete chopper line equipped with newly developed diagnostics to test the proposed chopping schemes (see Section 4.5.3). A list of the elements is given in Table 4.2 and the performance requirements are listed in Table 4.3.

Chopper structure

Short rise-times in the nanosecond range can be obtained by using travelling-wave stripline structures, where the striplines are meander-folded in order to match the speed of the travelling wave to the beam velocity (see Fig. 4.8).

In the present design, a section of 1.2 m is foreseen to accommodate two chopper units of 0.5 m, each housing two deflecting plates of 0.4 m length. To minimize the total length of the chopper line, the chopper units are designed to fit into the bore of existing quadrupoles (see Fig. 4.9). The deflecting plates are driven simultaneously in opposite polarity and water cooling is employed to handle heating from beam losses as well as from the deflecting signal. Since the striplines do not completely cover the deflector plates, one has to apply an 'effective surface coverage factor' for the electric field seen

Table 4.2: Elements in the chopper line

Element	**Number**	**Length** [mm]	**Value**	**Comment**
Long quadrupole I	2	255	$G = 0.8$–1.2 T/m	With chopper plates inside
Long quadrupole II	1	450	$G = 1.4$ T/m	
Short quadrupole I	4	56	$G = 15$–28 T/m	
Short quadrupole II	4	100	$G = 11$–15 T/m	
Chopper plates	2	400	Distance: 20 mm	
Dump	1	200		Conical hypervapotron
Buncher cavities	3	200	$V = 100/140$ kV	$P = 17.7/16.3$ kW (measured values)

Table 4.3: Beam chopper main parameters

Beam energy	3 MeV
Overall length	3.7 m
Number of chopper structures (inside quads)	2
Number of quadrupoles	11
Chopper plate length	400 + 400 mm
Chopper plate distance	20 mm
Separation chopped/ unchopped beam	15 mm
Chopper structure rise-and fall-time (10–90%)	< 2 ns
Chopper voltage pulse (per plate)	500 V
Effective chopper voltage pulse	400 V
Remaining voltage for unchopped beam	$< 2\%$
Max. chopper frequency	44 MHz
Min. pulse length	8 ns
Max. chopping factor (duty cycle)	40%
Repetition rate	1–50 Hz
Chopper deflection angle	5.3 mrad

by the beam. In our case this factor amounts to $\approx 80\%$, which means that for a deflection voltage of ± 500 V (i.e., 1 kV in total, or 800 V effective voltage) at a beam energy of 3 MeV one can achieve a total deflection angle of 5.3 mrad for both units.

As shown in Fig. 4.8, the travelling-wave structure consists of a double-meander stripline matched to a beam velocity of $\beta = 0.08$. The structure is printed on an alumina substrate with 3 mm thickness. The SPL design is related to the SNS chopper structure, which is also a printed meander structure [59] but which uses notched microstriplines with separating ridges in between. While the SNS structure is printed onto glass microfibre PTFE composite material, CERN uses an alumina substrate which is considered to be more stable against ionizing radiation and which has lower vacuum outgassing rates as well as higher heat-transfer coefficients.

Two plates have already been constructed [60] using a MoMn base layer (fired at 1500°C in an H_2/N_2 atmosphere) and several layers of other metals added. Their final shape is determined by a chemical etching process. Results of extensive numerical simulations as well as measurements on the rise- and fall-times and the deflecting efficiency have been presented in Ref. [61].

As an alternative to the MoMn process with chemical etching (done at CERN), a different technique is being proposed by industry. The actual base layer is a silk-screen-printed silver alloy, normally

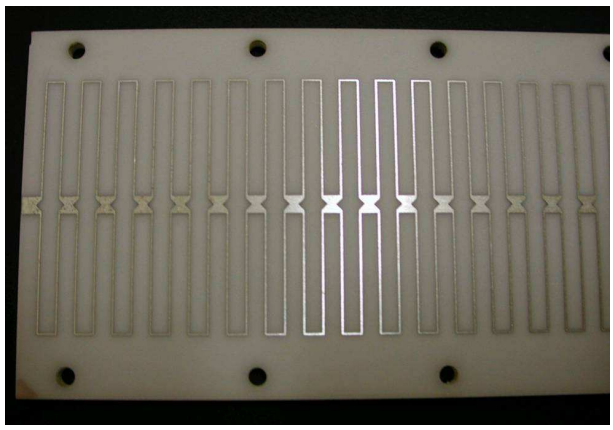

Fig. 4.8: The alumina ceramic plates with printed meander structure (MoMn + 30 μm Ag); mounting holes for screws are at the sides [60]

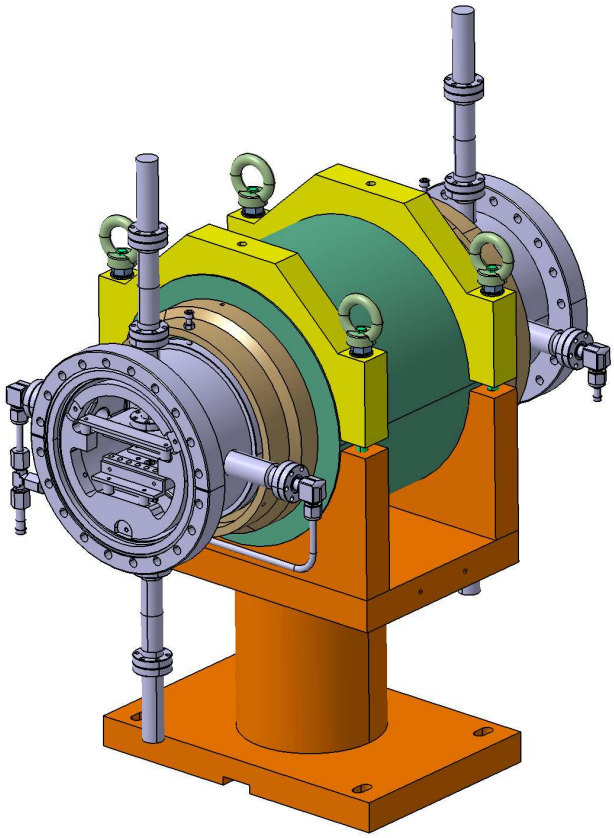

Fig. 4.9: Complete chopper with vacuum tank mounted in a quadrupole on a beam line support [61]

used for brazing ceramic–metal interfaces. This layer (a few microns thick) is fired at high temperature under vacuum and has an adhesion strength $\geq$100 N/mm^2, which is nearly as good as MoMn. Subsequently, the conductor (copper) thickness is increased up to 30 μm by electrochemical deposition, followed by a flash of gold to avoid surface degradation due to contact with air.

A 3D view of the complete chopper with vacuum tank, water cooling system and feedthroughs is shown in Fig. 4.9 and a summary of the main parameters is given in Table 4.3.

Chopper pulse amplifier

The electric field between the two plates must be established or removed within the time separating two bunches (2 ns). The most limiting constraint of the foreseen beam patterns is the one that requires the removal of three out of eight bunches. In this case we need an 8.5 ns pulse repeated at 44 MHz. To avoid the displacement of the baseline (0 V for the unchopped beam) across the output pulse mean value, the low-frequency cut-off must practically be DC, which is difficult to achieve with available technology. To relax the low-frequency response and make use of a band-pass amplifier, the bunch removal scheme shown in Fig. 4.10 will be used, where three out of eight bunches can be dumped using the superposition of two 22 MHz square waves with 18% duty cycle (8.5 ns pulse), inverse polarity and shifted by a half-period.

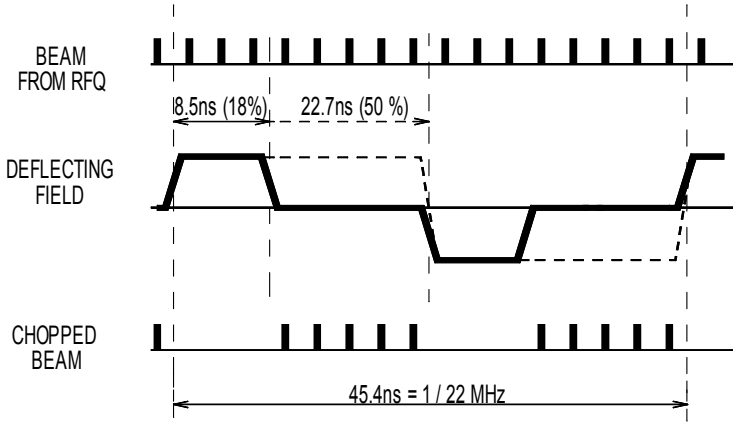

Fig. 4.10: Alternate polarity extraction scheme for the chopper pulse amplifier

The removal of a long sequence of bunches is possible by simply increasing the duty cycle for each amplifier to 50% and switching from one polarity to the other. The exact number of extracted bunches will then be obtained by adjusting the first and/or last cycle pulse length and/or with a slight change of the square wave frequency. In the above-mentioned conditions, to limit the baseline displacement to 2%, the low-frequency cut-off must be set around 140 kHz while the required 2 ns rise-time imposes a high-frequency response extending to above 175 MHz. To achieve such a wide band response and to manipulate the high required power (5 kW), the pulse amplifier will be based on an ultra-broadband hybrid coupler [62] with a theoretically infinitely high-frequency response independent of the electrical length of the transmission line composing it. Because of the freedom in choosing the line length, the circuit allows the use of any amount of ferrite to shift the low-frequency cut-off to the desired point. Like all hybrid couplers it can be used in *sum* and *difference* modes. The latter mode will be used to sum the signal of two identical amplifiers, obtain the polarity inversion required by the scheme, and thus achieve DC cancellation. Using the same basic configuration, a two-way hybrid and a four-way hybrid have been designed for signal combination. In both cases the –3 dB response goes from below 20 kHz to above 500 MHz. The basic amplifier unit shown in Fig. 4.11 is also built around the hybrid coupler but used in *sum* mode. To limit the number of cascaded stages and to achieve the required bandwidth, MOSFETS with $V_{ds} = 150$ V and low capacitances ($C_{iss} \approx 50$ pF, $C_{rss} \approx 2$ pF, $C_{oss} \approx 20$ pF) have been selected.

The drain circuit high-frequency cut-off is above 300 MHz and the transient time about 1.7 ns. With a DC supply of 100 V the nominal output pulse amplitude of the unit is ≈150 V on 25 Ω (Fig. 4.12).

The gates are driven by commercial drivers requiring TTL levels at the input. To maintain the wide band response of the circuit the DC supply is fed to the MOSFET drains via the hybrid itself from a zero RF point. In this design the ferrite used to increase the transmission line common mode impedance at low frequency is biased by the supply current. This means that on account of the range of operating currents from 0 to ≈8 A, the low-frequency cut-off sweeps from ≈40 kHz to ≈120 kHz, which is just below the

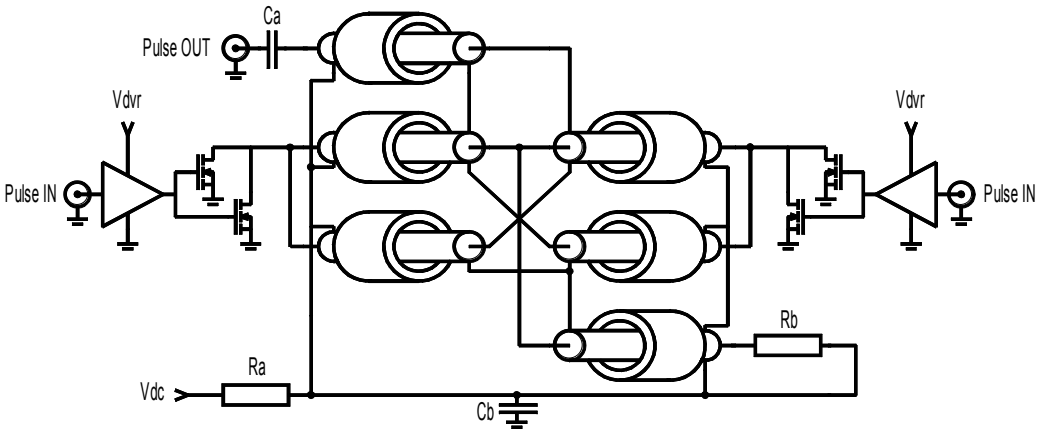

Fig. 4.11: Basic chopper pulse-amplifier unit (simplified schematic)

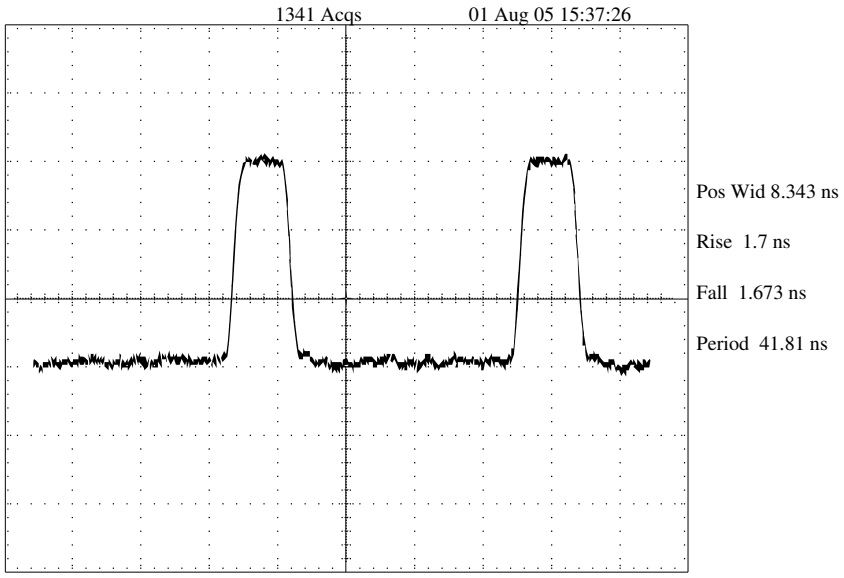

Fig. 4.12: Basic chopper pulse-amplifier unit output signal (50 V/div)

maximum cut-off frequency of ≈140 kHz. Two such units are combined with a two-way hybrid into a 50 Ω, 300 V module. Sixteen modules are then used to achieve the specified ±500 V (Fig. 4.13) [63].

4.3 Accelerating structures

4.3.1 Drift tube linac (DTL), 3–40 MeV

Following the chopper line at 3 MeV, three Alvarez DTL tanks at 352.2 MHz accelerate the beam up to an energy of 40 MeV. The first tank is powered by one klystron, whereas tanks 2 and 3 each use two klystrons (with one power coupler per klystron) in order to minimize the number of transitions between structures. Beam dynamics simulations with different beam currents show that the chopper line provides enough flexibility to match different currents into a DTL with fixed magnetic gradients. Therefore permanent magnetic quadrupoles (PMQs) were chosen to provide the transverse focusing because they reduce the cost of the focusing system, simplify the assembly of the drift tubes, and raise the shunt impedance by enabling smaller drift tube diameters. A relatively high accelerating gradient has been adopted (3.3 MV/m in the first tank and 3.5 MV/m in tanks 2 and 3) in order to reduce the linac length, benefiting from the availability of the old LEP klystrons to provide the higher RF power.

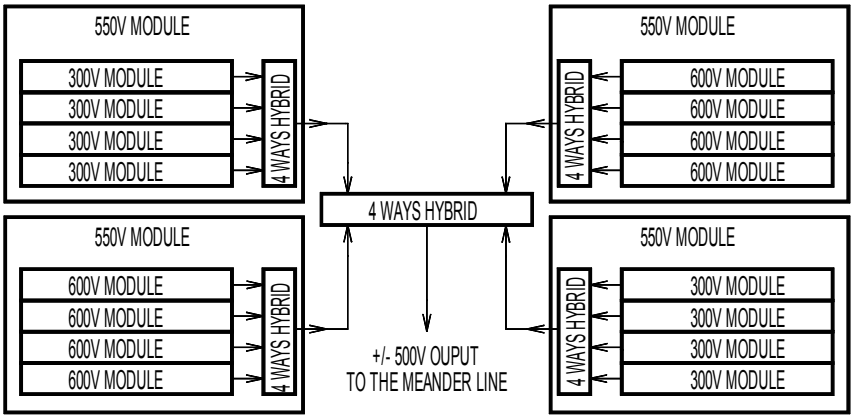

Fig. 4.13: Combining scheme for four 500 V chopper pulse-amplifier units

To further reduce the length of the DTL and to ease the RF tuning, the field ramp of the original tank 1 design in CDR1 [3], [64] has been eliminated without affecting the beam dynamics. In order to avoid too strong focusing at the beginning of tank 1, the initial synchronous phase was raised from $-44°$ to $-30°$ and the transit time factor was reduced by shortening the gaps. Towards the end of tank 1 the synchronous phase reaches its maximum value of $-20°$, which is then kept constant for tanks 2 and 3 as well as for the remaining normal-conducting linac. The value of $-20°$ is a compromise between beam stability and acceleration efficiency. The impact on beam stability of choosing $-20°$ rather than the more standard $-25°$ has been studied with respect to the development of phase and energy jitter [65] and with respect to r.m.s. emittance growth versus different longitudinal input emittances. In both cases no deterioration of the beam quality could be observed [32]. The missing longitudinal focusing between the tanks is compensated for by lowering the synchronous phase in the first and last accelerating gaps in the tanks. Post couplers are used to stabilize the field and a combination of fixed and movable plungers is used to adjust the frequency of the tanks. The main DTL parameters are summarized in Table 4.4.

Table 4.4: DTL main parameters

	tank 1	**tank 2**	**tank 3**
Output energy [MeV]	9.8	25.1	40
RF frequency [MHz]	352.2	352.2	352.2
Gradient E_0 [MV/m]	3.3	3.5	3.5
Synchronous phase [deg]	$-30 \rightarrow -20$	-20	-20
Lattice	FOFODODO or FODO		
Max. surface field [kilpatrick]	1.6 – 1.7	1.4 – 1.6	1.4 – 1.6
Aperture radius [mm]	10	10	10
Tank diameter [m]	0.52	0.52	0.52
Drift tube diameter [mm]	90	90	90
Length [m]	2.63	5.20	5.02
Peak RF power [kW]	700	1570	1550
Max. design duty cycle [%]	14	14	14
Klystrons	1	2	2
Quadrupole length [mm]	45	80	80
No. of gaps	28	33	24
No. of post couplers	9	16	23

A high-power prototype of tank 1, which could eventually be upgraded to be used in the final installation, is being built in Russia under a collaboration funded by the International Science and Technology Center (ISTC). The collaborating institutes are ITEP, Moscow (RF design and PMQ technology) and VNIIEF Sarov (mechanical design and construction). Although the basic design parameters were decided by CERN, the collaborating institutes elaborated the detailed mechanical design and defined technological solutions suited for their production facilities.

The drift tubes are mounted on a girder which is decoupled from the tank and are independently supported (Figs. 4.14, 4.15). The drift tubes are connected to the girder by bellows, which allow their precise alignment. This solution, already adopted for the old Linac2 at CERN, complicates the mechanics but avoids the use of O-rings in the drift tube assembly.

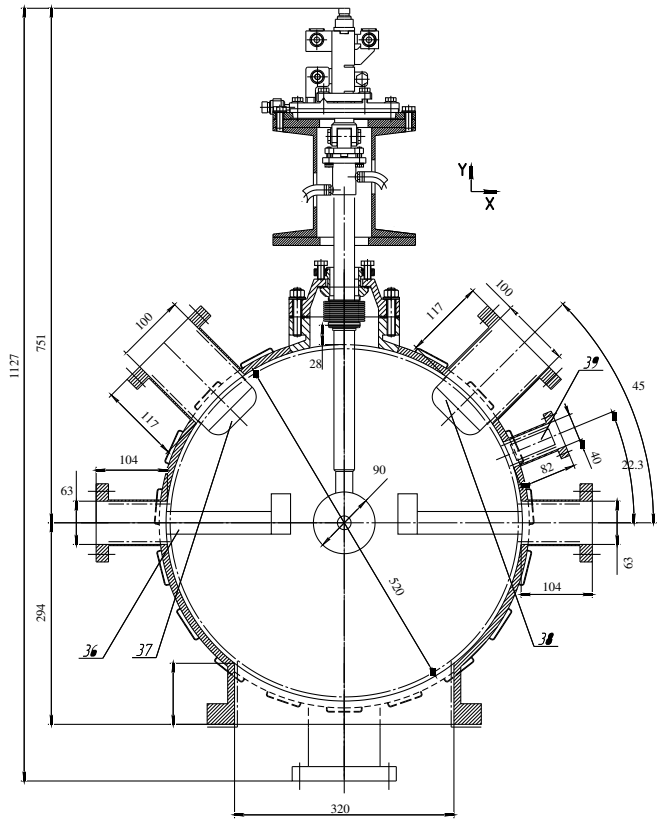

Fig. 4.14: Cross-section of DTL tank manufactured by VNIIEF, Sarov

Between the tanks are transition elements which are under vacuum and which allow space for diagnostics.

An elaborate adjustment unit (Fig. 4.16), developed by VNIIEF, allows the precise alignment of the drift tubes with respect to the girder. After the alignment the drift tube is fixed in position with a solid filling and the adjustment unit can be used for the subsequent drift tube. Should a re-alignment become necessary, the filling can be mechanically removed and replaced by a new one.

4.3.2 Cell-coupled drift tube linac (CCDTL), 40–90 MeV

A layout based on short 352 MHz DTL-like tanks containing two drift tubes (three accelerating gaps) has been selected for the energy range between 40 MeV and 90 MeV. The frequency of this section is kept at 352 MHz in order to use the LEP klystrons and to make possible a simple mechanical construction of the small tanks based on the same technology as the DTL. The tanks are made of copper-plated, stainless-

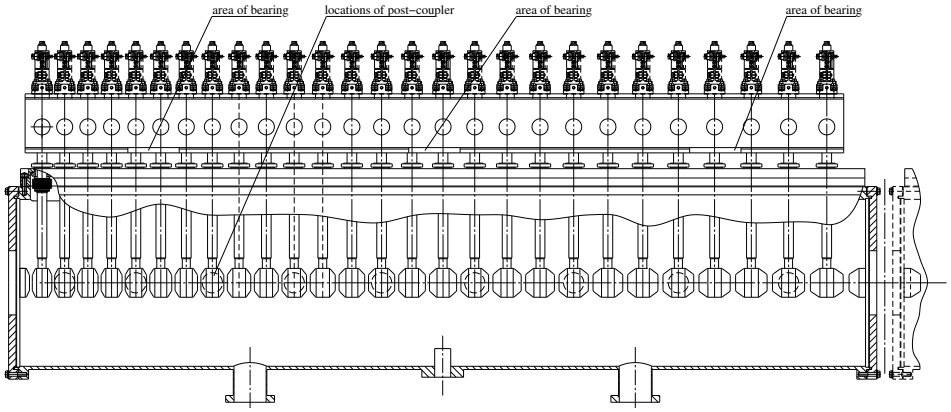

Fig. 4.15: Side view of DTL tank manufactured by VNIIEF, Sarov

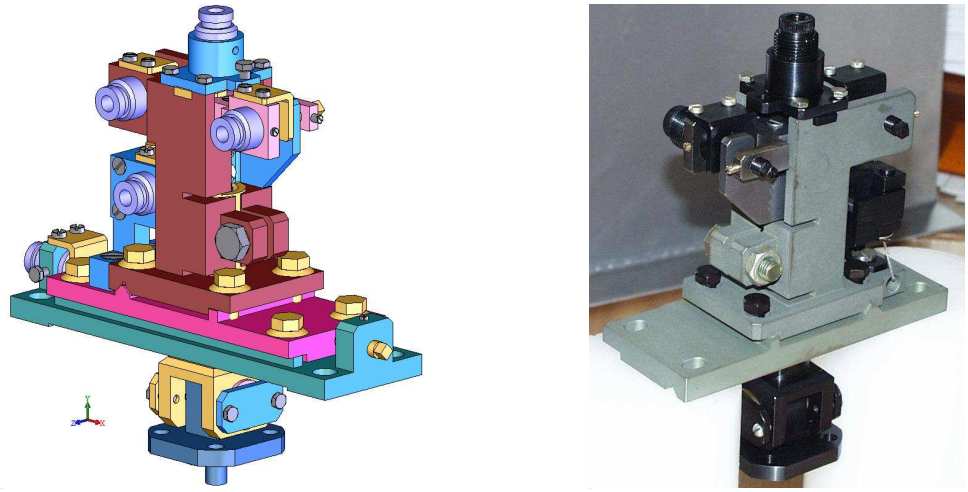

Fig. 4.16: Adjustment unit for the alignment of the drift tubes (left: drawing, right: photo)

steel elements connected by spring-loaded RF and vacuum joints. In order to avoid a complex power distribution system from the 1 MW klystron to the tanks and to allow simple setting of tank phase and amplitude, the DTL tanks are resonantly coupled by off-axis coupling cavities, leaving sufficient space for quadrupoles between the tanks. The resulting structure, shown in Fig. 4.17 and called Cell-Coupled Drift Tube Linac (CCDTL), is essentially a low-frequency symmetric version of a structure developed at LANL for the APT project [66]. For the chosen inter-tank distance, the resulting focusing period is $7\beta\lambda$, short enough to provide acceptable phase advance per period at the starting energy of 40 MeV. A string of three tanks forms one RF module, which is fed by a 1 MW klystron. The resulting module is a chain of five coupled resonators (three tanks and two coupling cells) operating in $\pi/2$ mode. Under normal operating conditions there is no field in the coupling cells. RF power is fed into the central DTL tank by means of an iris coupling to the side of a waveguide short-circuited at $\lambda/4$ from the iris.

The overall layout of the CCDTL is shown in Table 4.5, and Table 4.6 summarizes the main parameters of the CCDTL section. The gradient in each of the eight modules is adjusted in order to divide the RF power evenly between the klystrons, at a power per klystron of 800 kW. As a consequence, the accelerating gradient decreases from 3.9 MV/m to 2.8 MV/m, and the peak surface field decreases correspondingly from 1.6 to 1.3 times the Kilpatrick limit. Figure 4.18 shows the computed shunt impedance of the CCDTL section, compared to that of the DTL and SCL. The transition to the CCDTL allows a partial compensation of the characteristic decrease in shunt impedance of DTL structures.

Table 4.5: CCDTL layout (three gaps per tank, three tanks per module)

Module	E_0 [MV/m]	P_{klystron} [kW]	**Energy** [MeV]
1	3.89	800	46.4
2	3.61	800	52.8
3	3.37	800	59.2
4	3.19	800	65.7
5	3.05	800	72.2
6	2.95	800	78.7
7	2.87	800	85.2
8	2.81	800	91.7

Table 4.6: CCDTL main parameters

Input energy	40 MeV
Output energy	91.7 MeV
RF frequency	352.2 MHz
Gradient E_0	2.8–3.9 MV/m
Synchronous phase	−20 deg
Number of tanks	24
Lattice	FODO
Max. surface field	1.4–1.7 kilpatrick
Aperture radius	14 mm
Length	25.2 m
Peak RF power	6.4 MW
Max. design duty cycle	14%
Klystrons	8
No. of gaps	72

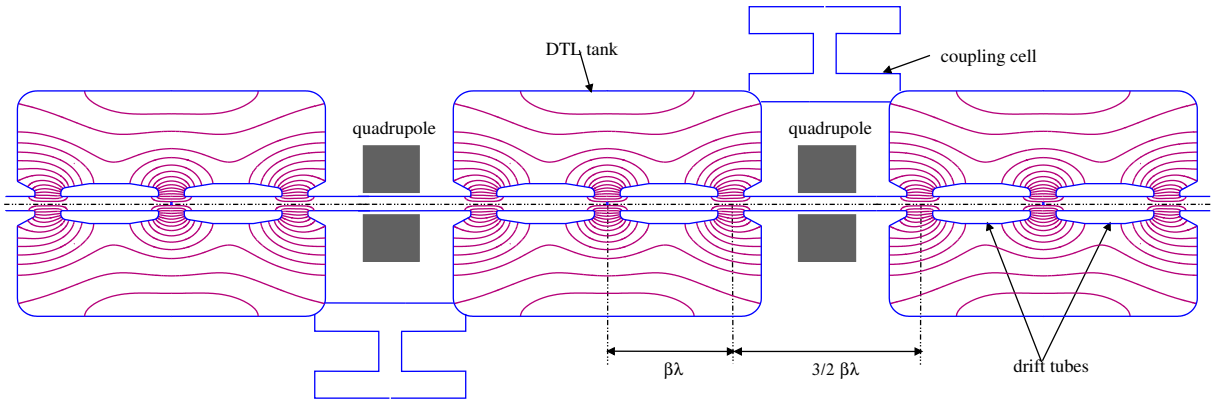

Fig. 4.17: Outline of the CERN cell-coupled DTL, showing electric field lines in one three-cavity module

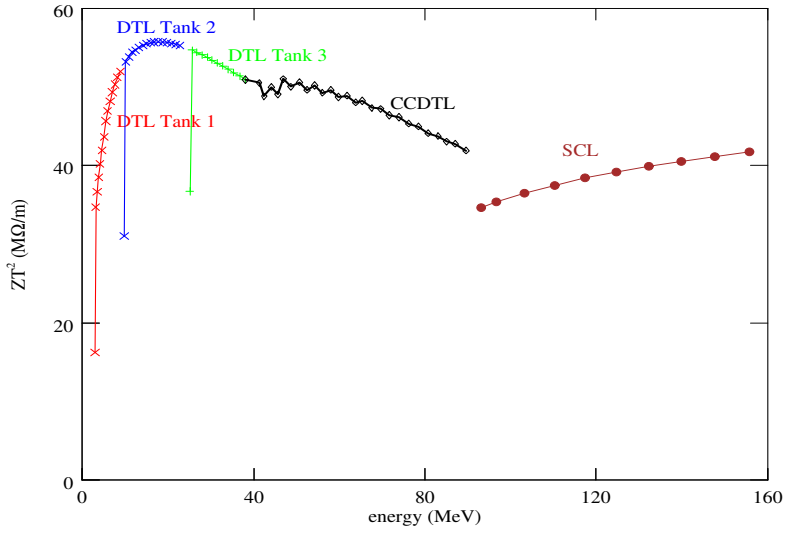

Fig. 4.18: Computed shunt impedance (linac definition) of DTL, CCDTL, and SCL

The development of this particular CCDTL structure took place at CERN during the last four years [35, 67]. After detailed beam dynamics and 3D RF simulations, a high-power prototype made of two half-tanks and one coupling cell was designed and built (Fig. 4.19). It has validated the construction technology, the resonant coupling principle, and the RF coupler design. High-power RF tests foreseen in the SM18 test stand will allow testing of the cooling circuits and will define the RF conditioning procedure. In the frame of an ISTC-funded collaboration, BINP, Novosibirsk and VNIIEF, Snezinsk are currently constructing a complete CCDTL prototype module, whose design is shown in Fig. 4.20.

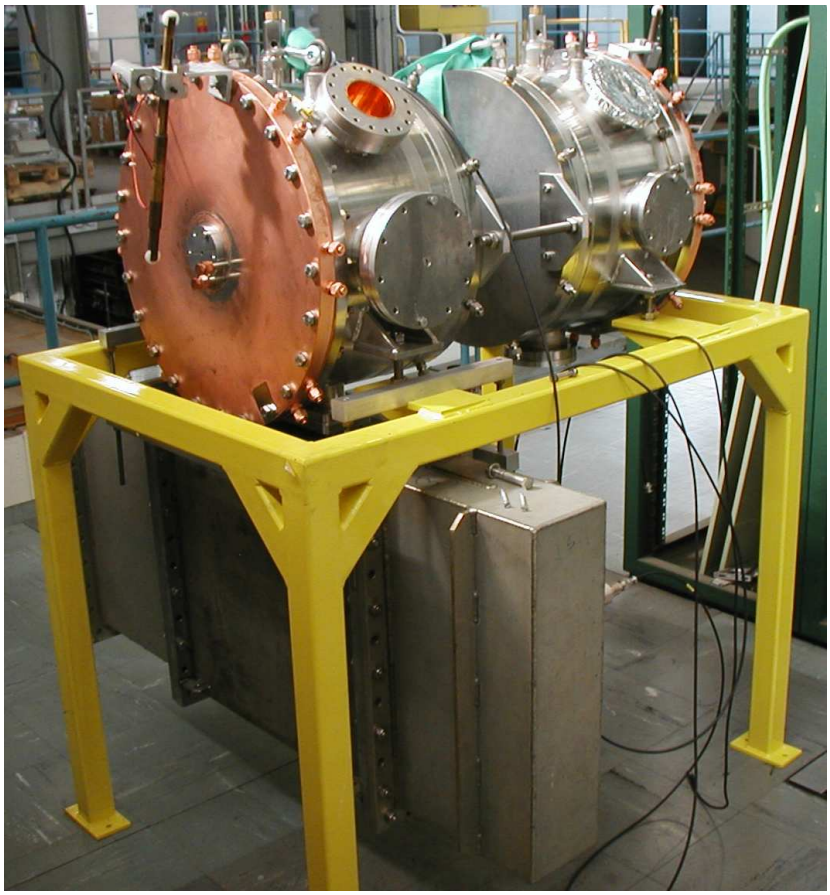

Fig. 4.19: The CERN CCDTL prototype including power coupler at the bottom during low-level RF tests

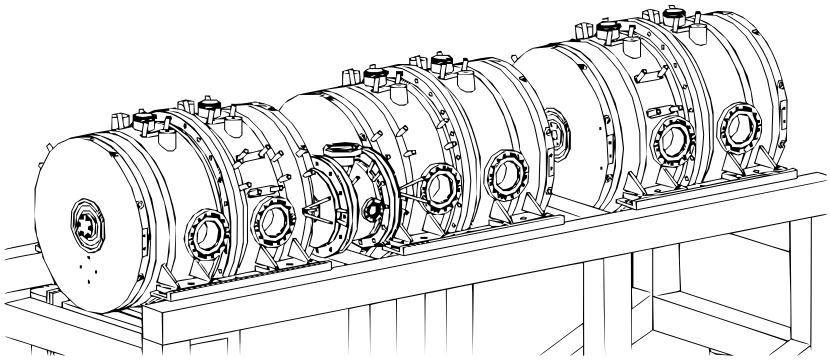

Fig. 4.20: The CCDTL full-module prototype under construction in Russia

4.3.3 Side-coupled linac (SCL), 90–180 MeV

From an energy of ≈100 MeV onward, the shunt impedance of DTL-like structures decreases drastically. To maintain a reasonable RF power efficiency, it is convenient to replace the DTL with a π-mode structure (i.e., with 180° phase difference between the fields in two subsequent gaps) at a higher harmonic of the basic frequency. For the SPL a standard Side-Coupled Linac (SCL) has been chosen at twice the basic frequency (704 MHz) starting from a transition energy of 90 MeV [68]. This particular type of π-mode structure, developed at LANL in the 1960s, has been used for many linac projects worldwide. A prototype SCL at higher frequency has already been built at CERN and tested with beam in the frame of the TERA project.

The SCL is made of sequences of accelerating cells, coupled via slots to coupling cells placed alternately on both sides of the accelerating cells. Eleven cells are grouped in tanks, spaced by focusing quadrupoles (Fig. 4.21). Multiple tanks can be fed by a single klystron, and are coupled together by bridge couplers, additional short chains of cells joining tanks across the quadrupoles. The coupling cells are needed to resonantly couple the single accelerating cells, transforming the operating mode into the stable $\pi/2$ mode, which ensures a uniform longitudinal field distribution even in the presence of mechanical and tuning imperfections [69].

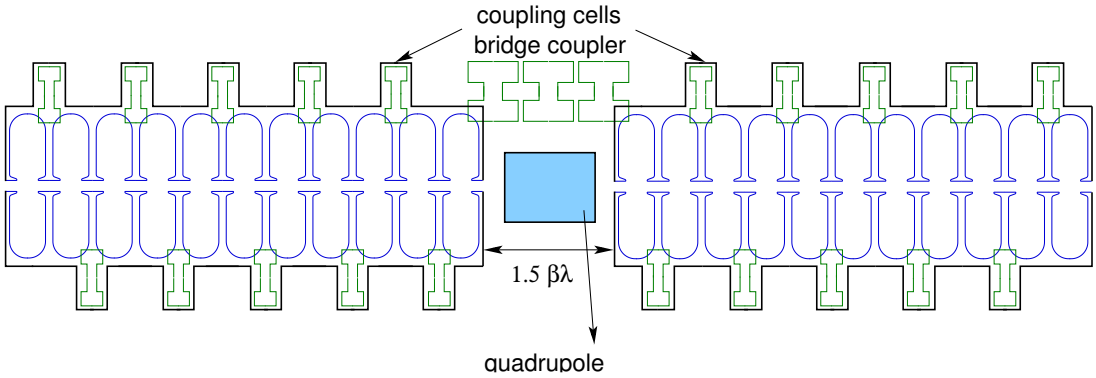

Fig. 4.21: Side-coupled linac (SCL) structure for Linac4/SPL

The increase in frequency with respect to the previous sections provides higher shunt impedance, and allows the dimensions of the structure to be reduced. However, the larger power dissipation per unit surface requires a different construction technology than for DTL structures. The SCL cavities of the SPL are made of stacks of brazed copper cells.

For beam dynamics stability, the same type of focusing (FODO) as in the preceding CCDTL is maintained throughout the SCL lattice, with single quadrupoles between tanks. The aperture radius is 16 mm, about eight times the r.m.s. beam size. The slots between cells provide a cell-to-cell coupling of 3%, sufficient for the required field stability, and it is foreseen to re-machine the slots individually to minimize the effect of machining errors on the coupling factor. The distance between tanks is fixed to 1.5 $\beta\lambda$ to allow sufficient space for quadrupole, bellow, flanges, and some diagnostics. Tanks will be connected by three-cell bridge couplers. Klystrons delivering 4 MW are foreseen, each feeding a module of five tanks. The accelerating gradient has been fixed to $E_0 = 4$ MV/m, providing a good compromise between length of the structure and RF power consumption, while keeping the peak surface fields below 1.6 kilpatrick. With this gradient, only five klystrons are needed to cover the energy range between 90 MeV and 180 MeV, the last module being made of four tanks. The SCL layout is presented in Table 4.7, and the main parameters in Table 4.8.

The development of the SCL is being carried out inside the HIPPI Joint Research Activity, co-funded by the European Union. The RF design is being jointly developed between CERN and the IN2P3

Table 4.7: SCL layout (11 cells per tank)

Module	E_0 [MV/m]	P_{klystron} [MW]	**Energy** [MeV]	**No. of tanks per module**
1	4	3.00	107.42	5
2	4	3.06	125.16	5
3	4	3.15	144.16	5
4	4	3.24	160.07	5
5	4	2.64	181.00	4

Table 4.8: SCL main parameters

Input energy	92 MeV
Output energy	180 MeV
RF frequency	704.4 MHz
Number of tanks	24
Gradient E_0	4 MV/m
Synchronous phase	-20 deg
Lattice	FODO
Max. surface field	1.1–1.2 kilpatrick
Aperture radius	16 mm
Length	34.4 m
Peak RF power	15.1 MW
Max. design duty cycle	14%
Klystrons	5
No. of gaps	264

LPSC Laboratory in Grenoble, while the analysis of the behaviour of long SCL chains is being made by INFN Naples. The thermal analysis of the SCL cells is done in Grenoble. A brazed technological copper model, intended for vacuum and low-level RF tests, is going to be built by BINP Novosibirsk as a part of a project funded by ISTC.

4.3.4 Superconducting linac

Since the development of the LEP superconducting cavities, involving niobium sputtered onto copper, there has been considerable progress in the technology of bulk-niobium SC cavities (compare also Section 2.3). In the SPL, two families of bulk-niobium elliptical cavities with a geometrical β of 0.65 and 1.0 have been chosen to cover the energy range from 180 MeV to 3.5 GeV using a frequency of 704.4 MHz (compare Section 4.3.4.3). In the following we review recent progress in this technology and we motivate the chosen accelerating gradients of 19 MV/m and 25 MV/m for the $\beta = 0.65$ and $\beta = 1.0$ sections.

Since the cryo-module design has an important influence on the real-estate (accelerating) gradient, the decision was taken to follow mainly the Tesla Test Facility (TTF) approach, which minimizes the number of cold/warm transitions and uses cold quadrupoles within the cryo-modules. The motivation for this choice and the preliminary parameters are presented in Section 4.3.4.2.

4.3.4.1 Cavity technology

The choice of bulk-niobium, multi-cell, superconducting elliptical cavities operating at a temperature of 2 K implies the use of the following technologies [20]:

- Proper grade material (niobium sheets with Residual Resistance Ratio (RRR) values in the range 200–300).
- Proper treatment techniques: thermal treatments for stress annealing and hydrogen degassing at 600–800°C; deep chemical etching with Buffered Chemical Polishing (BCP) techniques for removing 100–200 μm of material from the surface; High Pressure Rinsing (HPR) with ultra-pure water to remove any contaminants from the surface.
- Proper handling procedures (mainly 'cleanliness', meaning that all work around a cavity and its ancillaries should be performed in a clean room).

The performance limitations of superconducting cavities are basically caused either by field emission or by the intrinsic limitations of the superconductor material. In the first case the surface electric field on the cavity walls is responsible for the electron emission starting from surface contaminants or protrusions, while in the latter the effect is dominated by the magnetic field level at the cavity surface.

Elliptical cavities designed for particle velocities smaller than the speed of light (medium-β cavities) have, for the same frequency, smaller volumes with respect to cavities designed for relativistic particles ($\beta = 1$). This is mainly because the cell length of a π-mode structure has an active length given by $\beta\lambda/2$, while the cell diameter does not depend, to first order, on the design β, but only on the frequency. In other words, the ratio of peak electric (or peak magnetic) field to the cavity accelerating field grows with decreasing design β.

The geometrical shape of the superconducting medium-β structures can be optimized for the application needs by using a proper parametrization, which allows independent tuning of electromagnetic and mechanical characteristics [70], such as peak field ratios, cell-to-cell coupling, R/Q, Lorentz-force detuning coefficients, and mechanical stresses under operating conditions.

Several bulk-niobium, reduced-β, multi-cell cavities at different frequencies have been designed, fabricated and tested in the last decade, for various high-power proton linac applications. The tests of these structures yielded results which are consistent, in terms of peak fields, with those of the extensive experience gained with the TTF production and cavity treatments. The measured electromagnetic characteristics of the cavities listed in Table 4.9 are the basis for the estimated performance of newly developed SPL cavities.

Table 4.9: Medium-β multi-cell cavity parameters (bulk-niobium structures only)

Project	f [MHz]	β	$E_{\mathrm{peak}}/E_{\mathrm{acc}}$	$H_{\mathrm{peak}}/E_{\mathrm{acc}}$ [mT/(MV/m)]	N_{cell}	$(R/Q)/N_{\mathrm{cell}}$ [Ω]	**Ref.**
RIA	805	0.47	3.34	5.94	6	26.67	[26]
TRASCO	704	0.47	3.57	5.88	5	31.60	[22]
SNS medium-β	805	0.61	2.71	5.72	6	46.50	[25]
CEA/CNRS	704	0.65	2.60	4.88	5	63.00	[24]
SNS high-β	805	0.81	2.19	4.72	6	80.50	[25]
TTF	1300	1.00	2.00	4.16	9	115.11	[71]

(R/Q) uses the 'linac' definition.

All the cavities in Table 4.9 have been fabricated, handled, and tested using the procedures briefly outlined in the previous paragraph. Single-cell prototypes, which can be found in the literature, have not been considered. Single-cell cavities have much lower values of $E_{\mathrm{peak}}/E_{\mathrm{acc}}$ because of the electric field penetration in the large bore of the end tubes, and they are less sensitive to field emission effects during tests. In addition, the chemical and rinsing procedures are more effective for these simpler geometries. As a consequence, single-cell structures generally reach higher accelerating fields than the corresponding multi-cell structures [72].

Figure 4.22 shows the design peak (electric and magnetic) field ratios (with respect to the accelerating field) for the cavities listed in Table 4.9, as a function of the cavity design β. It illustrates the increase of the $E_{\mathrm{peak}}/E_{\mathrm{acc}}$ and $H_{\mathrm{peak}}/E_{\mathrm{acc}}$ factors with the decrease of the design β of the structure.

Figure 4.23 shows the behaviour of the geometrical R/Q value per cell of the cavities in Table 4.9. We have used the *linac definition* of the shunt impedance definition [$R = (\Delta V_{\mathrm{c}})^2/P_{\mathrm{c}}$], where ΔV_{c} is the voltage provided by the cavity (at the nominal β) and P_{c} the power dissipated on the walls. Again, the geometrical R/Q value per cell decreases almost linearly with β.

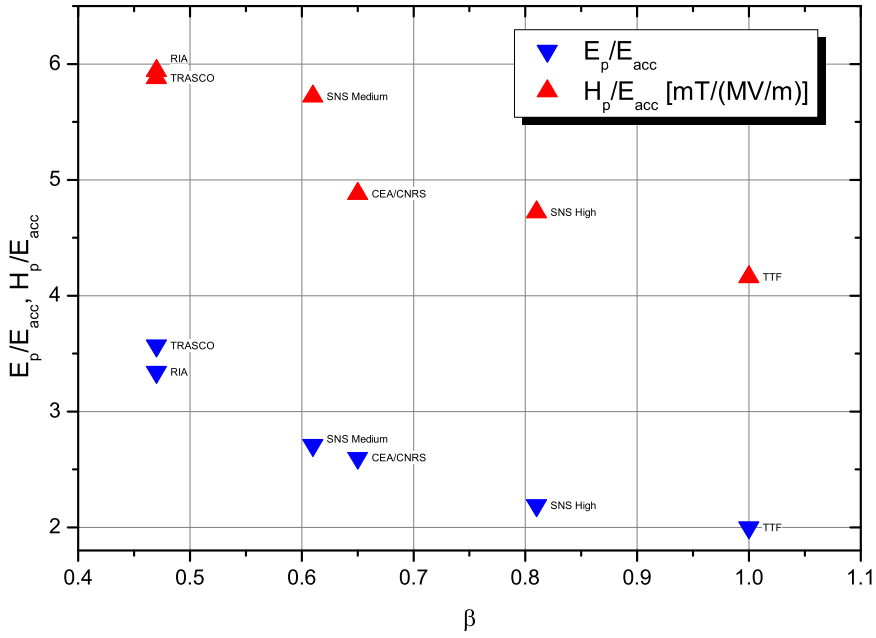

Fig. 4.22: Peak field ratios for the cavities listed in Table 4.9

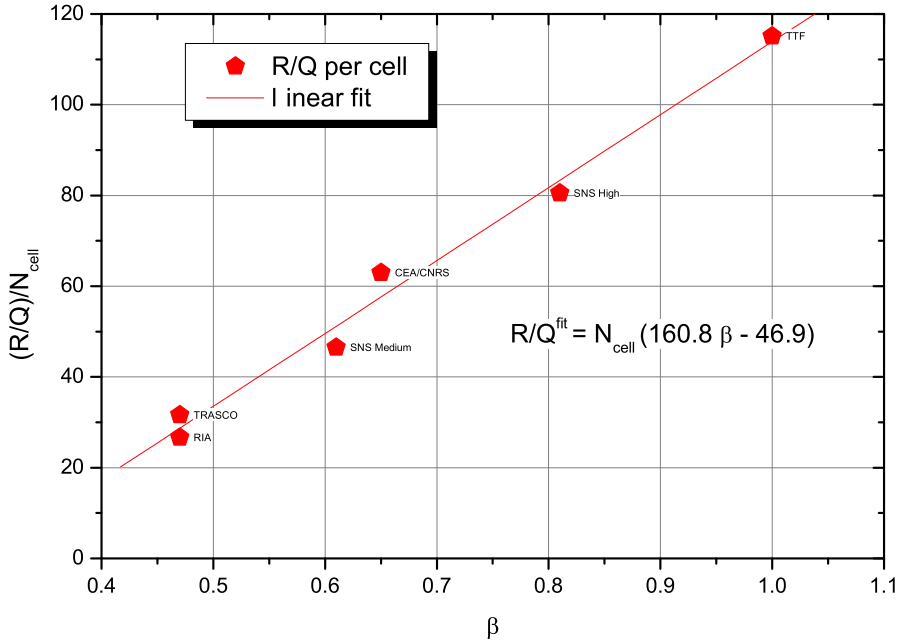

Fig. 4.23: Geometrical factor R/Q (linac definition) per cell of the cavities in Table 4.9

It is not straightforward to make a complete comparison of the TTF experience (which started 15 years ago and produced industrially in four production batches a total of more than 100 multi-cell cavities, performing hundreds of CW vertical tests at the DESY facilities) with the results of the very few cavity prototypes built by the other programmes listed above, except for SNS, for which a comparable number of resonators have been built and tested [73].

An analysis of the TTF cavity data [74] shows a definite 'learning curve' effect on the achieved cavity performances during the first three production batches [75]. As the performance goal of the TTF

Collaboration was shifted to higher accelerating gradients (in the range of 30–35 MV/m) in view of the TESLA Linear Collider scale (and now of the global design effort for the International Linear Collider [76]), the standard chemical treatment of the TTF cavities was switched to etching by electrolytical polishing (EP), a surface preparation method which yields smoother surfaces with respect to the BCP procedure and is more promising for achieving performances closer to the material limitations in terms of surface magnetic fields [77]. Nonetheless, the RF performances of the BCP-treated cavities of the third production batch of the TTF cavities achieved a maximum accelerating field of 28.3 MV/m, with an r.m.s. spread of 1.3 MV/m and an average field emission onset greater than 22 MV/m.

In the following comparison with the performance of other cavities, the TTF cavities are accounted for in an operation extending between 22 MV/m and 28 MV/m average maximal accelerating field. It should be noted, however, that chemically etched cavities already reached accelerating fields in excess of 30 MV/m, and electro-polished cavities were capable of reaching even higher fields, up to nearly 40 MV/m in the absence of field emission (only considering BCP chemical etching).

Concerning SNS, the performance data on the cavity prototypes was described in Ref. [25] (with 17 MV/m and 20 MV/m of E_{acc} for $\beta = 0.61$ and 0.81, respectively). More recent data, with production statistics, has been presented in Ref. [73] and is summarized in Table 4.10. The main limiting factor

Table 4.10: SNS cavity performances

Cavity	$E_{\mathrm{acc}}^{\mathrm{max}}$ [MV/m]	**Field-emission onset** [MV/m]	**Number tested**
$\beta = 0.61$	16.4	10.7	35
$\beta = 0.81$	18.7	6.2	48

reported from the SNS production experience, and the main cause of the relatively high rejection rate experienced in the production phase, is an early field-emission onset (the SNS acceptance value asks for a peak field of 27.7 MV/m without field emission).

Other medium-β elliptical structures for which RF test data is available and is included in Table 4.9 are the TRASCO five-cell cavities (two $\beta = 0.47$ structures [22]), the RIA six-cell cavities (three $\beta = 0.47$ structures [26]), and the CEA/CNRS five-cell $\beta = 0.65$ cavity [24]. Figure 4.24 shows their surface electric field corresponding to the maximum gradients and field-emission onset.

It is worth noting that, in terms of peak surface electric field, the prototypical medium-β proton cavities considered show comparable performances to the average TTF cavity production of the third batch. The standard TTF cavity preparation procedure (chemical etching followed by high-pressure rinsing stages with ultra-pure water) seems to be suitable for the reduced-β geometries in this range (down to the extremely compressed 0.47 structures). Moreover, no indications for any dependence of the peak surface field on the cavity frequency seem to be evident from the data.

Figure 4.25 shows the data for the same set of cavities in terms of peak surface magnetic field. Owing to the stronger dependence of $E_{\mathrm{peak}}/E_{\mathrm{acc}}$ as a function of β with respect to the ratio $H_{\mathrm{peak}}/E_{\mathrm{acc}}$ (see Fig. 4.22), the electric field limitations are more rapidly reached in the lowest β structures, and the larger spread seen in the data for the $\beta = 0.47$ structures does not come from magnetic field limitations, but from electric field limitations.

The fact that the lower-β structures are more sensitive to electric field effects than to magnetic ones is explained by the behaviour of the ratio $H_{\mathrm{peak}}/E_{\mathrm{peak}}$, shown in Fig. 4.26 as a function of the structure β. As seen from the figure, the lowest-beta structures tend to be penalized by the drastic reduction of the cavity capacitive volume, which implies that generally the field emission limitation is reached well before the magnetic limitation.

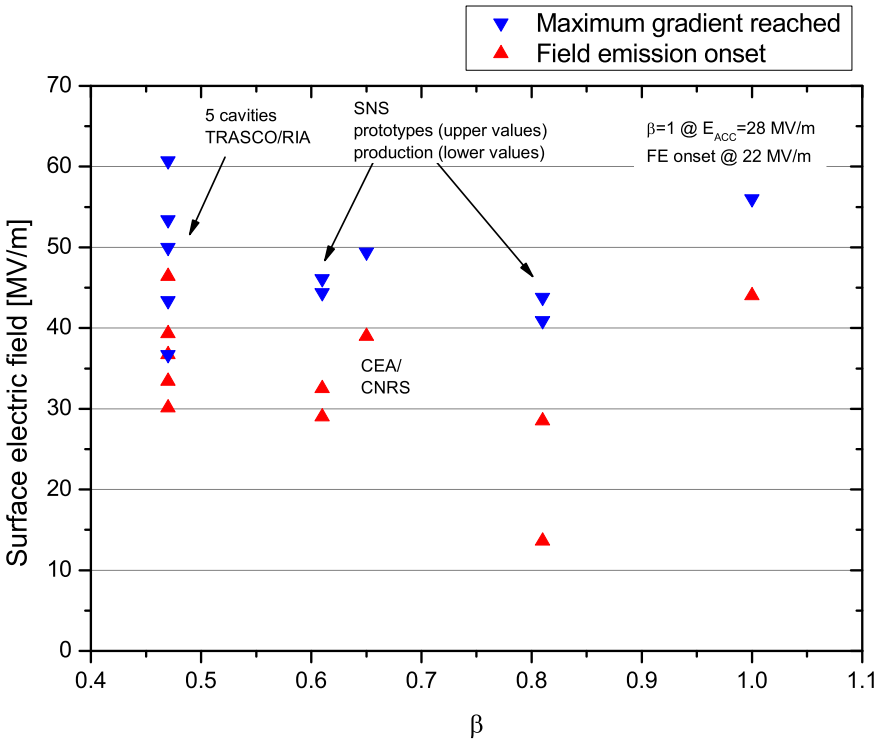

Fig. 4.24: Peak surface electric field (MV/m) corresponding to the maximum gradients reached in the cavity tests (down triangle) and to the onset of field emission, FE (up triangle)

The analysis presented here takes into account the wide experience accumulated in the last 15 years by the TESLA Collaboration on the reliable production and operation of high-gradient multi-cell structures, the ongoing work performed both for the XFEL Project and the ILC Collaboration for reaching even higher performance goals, and the learning curve observed during the TTF production. Considering these experimental results, we base the design of the superconducting SPL section on the assumed parameter values given in Table 4.11.

Table 4.11: SPL superconducting linac design parameters

Maximum peak surface electric field	50 MV/m
Maximum peak surface magnetic field	100 mT
Cavity quality factor at 2 K	$\geq 10^{10}$
Accelerating gradient ($\beta = 0.65$)	19 MV/m
Accelerating gradient ($\beta = 1.0$)	25 MV/m
R/Q ($\beta = 0.65$)	290 Ω
R/Q ($\beta = 1.0$)	570 Ω
Frequency	704.4 MHz
Number of cells	5

We also conclude that the maximum peak fields show only little dependence on the operating frequency, meaning that there is no motivation to introduce a third frequency step (e.g., to 4×352.2 MHz) in the SPL.

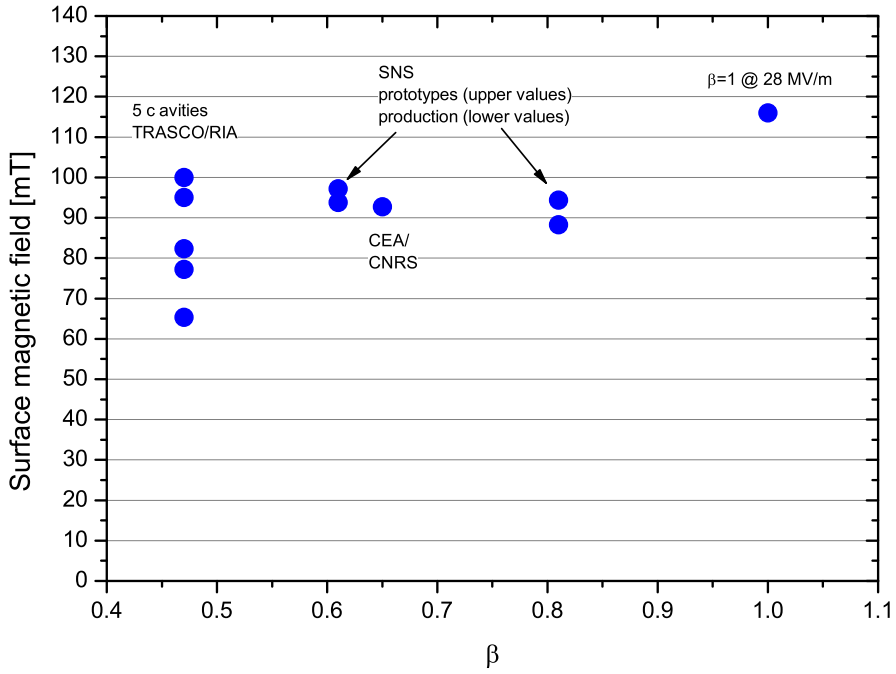

Fig. 4.25: Peak surface magnetic field (mT) corresponding to the maximum gradients reached in the cavity tests

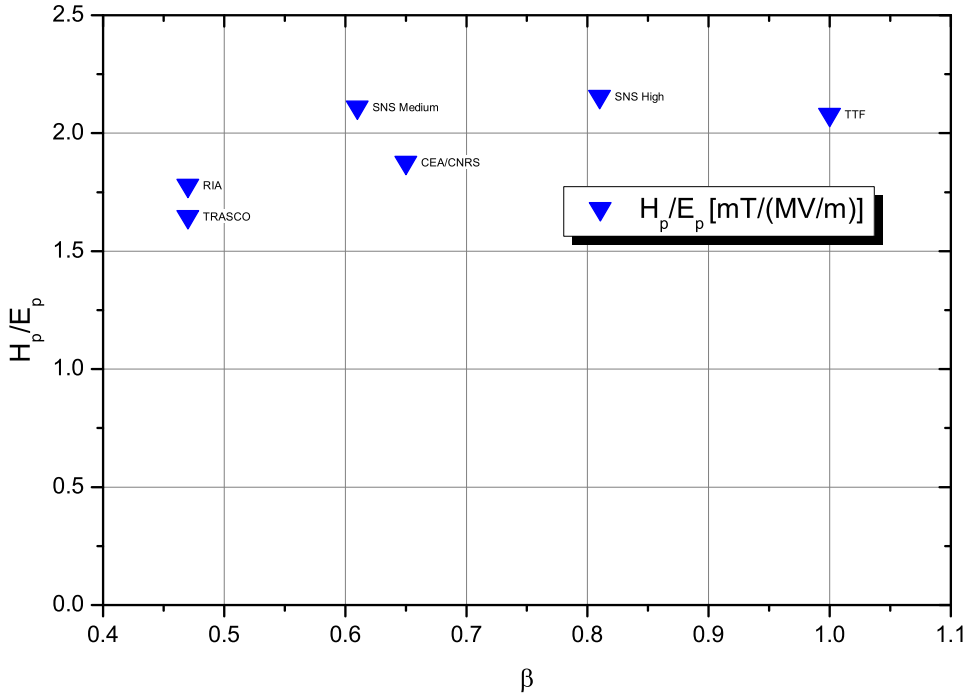

Fig. 4.26: Ratio of peak magnetic to peak electric fields

4.3.4.2 Criteria for cryo-module design

The real-estate gradient of a 2 K superconducting linac does not depend uniquely on the RF structure accelerating gradient, but more importantly on the technological choices that determine the layout of the cryo-modules. Each cold-to-warm transition at the beam-line level requires a certain length and reduces the overall filling factor. Currently, there exist two proven designs, with different relative merits, for a GeV-sized 2 K superconducting RF accelerator: the TTF/TESLA/ILC [78] and the SNS cryo-modules [79].

The TTF module has been conceived as the building block for a TeV-sized superconducting electron linac. Thus, the design aims for very low static losses (due to the huge size of the accelerator with 20 000 superconducting RF structures), high filling factors (to minimize the linac length), and low cost. The module contains eight cavities, a superconducting magnet package for beam focusing every three modules, and integrates the distribution lines of the cryogenic fluids. Tens of modules are connected together to form independent strings from the vacuum and cryogenic point of view, limiting the number of cold-to-warm transitions along the beam line. These choices imply that the substitution or opening of a single module leads to a warm-up/cool-down cycle for the whole string, and hence high reliability needs to be guaranteed in the cold mass. The TTF concept is still the baseline for the ongoing ILC cryo-module design [80].

The SNS module, on the other hand, hosts few (3–4 in the two beta sections) cavities, does not contain any focusing elements—the quadrupole doublets are located in the warm sections between modules—and has been designed to be quickly disconnected from the beam line (in less than a day a SNS linac module can be exchanged). These design criteria, together with the moderate energy of the SNS superconducting linac (extending from 200 MeV to 1 GeV), led to a much lower filling factor than the TTF case.

For the 3.5 GeV SPL linac at the CERN site, filling factor considerations play an important role, and this strongly motivated the choice to base the linac design on long interconnected modules with several (6–8) cavities and cold focusing magnets in each unit. By using such a layout, the 180 MeV – 3.5 GeV energy range can be covered with the two $\beta = 0.65$ and $\beta = 1$ sections in approximately 350 m.

At the high duty cycle envisaged for the SPL linac, the main heat loss contribution at the 2 K level is given by the RF dynamic losses on the cavity walls. As in the TTF module, a 50–75 K thermal radiation shield, with Multi-Layer thermal Insulation (MLI), screens the inner mass from the 300 K environment of the vacuum vessel and provides thermalization of penetrations (i.e., couplers, supports and cabling) at high temperatures. A second inner shield, operating at 5–8 K with MLI insulation, further shields the cold mass from the thermal radiation of the outer shield and provides a further possibility of thermalization of the penetrations. A preliminary estimation for the main heat loads on the cryogenic circuits in the two modules is given in Table 4.12.

The static loads reported here are scaled from the measured values in the TTF modules [19], increasing the thermal radiation contribution (amounting to approximately 1/3 of the total) in the higher temperature circuits to take into account the larger cross-section needed to accommodate the larger 704 MHz cavities.

The dynamic RF load at a 6% duty cycle has been calculated by using the cavity parameters reported in Table 4.11, according to the extrapolation given in Fig. 4.23. A dynamic load at 2 K accounting for a beam loss level of 1 W/m has been included. The heat load summarized in Table 4.12 represents a preliminary estimation and contains only a rough estimation of the dynamic load contribution from couplers and Higher Order Mode (HOM) absorbers, for which a detailed design, and corresponding calculations, are still missing. The results from the SNS linac commissioning will provide experimental data allowing these estimations to be refined for the high duty cycle case of the SPL. Considerations on the cryogenic system architecture needed for the superconducting section of the SPL linac are expressed in Section 4.7.

Table 4.12: First estimations on heat losses in the SPL modules assuming a 6% duty cycle

$\beta = 0.65$ module (six cavities, 11.45 m length)			
Heat load	2 K [W/m]	5–8 K [W/m]	50–75 K [W/m]
Static load	0.3	1.3	7.7
Dynamic RF load	1.9		
HOM†	0.75	0.5	9.1
Coupler‡	0.06		
Beam losses	1	–	–
$\beta = 1$ module (eight cavities, 14.26 m length)			
Heat load	2 K [W/m]	5–8 K [W/m]	50–75 K [W/m]
Static load	0.3	1.3	7.7
Dynamic RF load	4.2		
HOM†	1.7	0.4	7.2
Coupler‡	0.13		
Beam losses	1	–	–

† Estimated to be $\approx$ 40% of the dynamic RF load (see Section 4.7.2).

‡ Estimated to be $\approx$ 3% of the dynamic RF load (see Section 4.7.2).

4.3.4.3 Layout of the superconducting section

The transition energy between normal and superconducting structures was chosen to be 180 MeV. Above this energy the real-estate gradient of currently available superconducting elliptical cavities is substantially higher than for normal-conducting structures. Below this energy, we consider that there is still need for R&D before superconducting structures can be used at low cost in a pulsed high-power proton linac.

The different cavity types and transition energies are derived from the optimization of length and cost. To minimize development costs, complexity of maintenance and stock of spare parts, only two different cavity shapes will be used, one for the medium-energy range with a geometrical β of 0.65 and one for the high-energy range with $\beta = 1$. The operating frequency is 704 MHz for both structures and the gradients correspond to the values in Table 4.11. The optimization process considers several combinations of different architectures taking into account cavity length, transitions between cavities, number of cells, and achievable gradients.

The longitudinal phase advance at zero current per lattice must be lower than the transverse one to avoid emittance exchange between the planes due to space-charge resonances. The phase advance per metre is kept smooth along the superconducting linac in order to achieve a current-independent structure. This condition also simplifies the beam matching at transitions. The setting of the synchronous phase ensures the continuity with the preceding normal-conducting section and provides sufficient acceptance for the injection into the superconducting linac. The synchronous phase varies linearly from -20° to -15° with the final value being reached at 50 m. It has been estimated that -15° provides enough stability to manage static and dynamic errors of the RF system. The optimization procedure converges to the architecture given in Table 4.13.

Quadrupoles are included in the cryo-modules. For the medium-energy section one cryo-module contains two focusing periods, whereas in the high-energy part one period is housed in one cryo-module. In addition to the reduced cryogenic losses, the reduction of cold-to-warm transitions minimizes the length of the linac. This choice, coupled with the high gradients, yields a linac length of 342 m. The maximum power per coupler is 543 kW for the first section and 1.018 MW for the second section [Fig. 4.27(a)]. Symmetric five-cell cavities maintain field flatness over a wide tuning range in both sections by providing an identical deformation of both end-cells. Their large apertures minimize the risk of inadequate damping of higher order dipole modes which could be excited by the beam. Stiffening

Table 4.13: Layout of the superconducting sections assuming five cells per cavity

Sections	W_{in} [MeV]	W_{out} [MeV]	**Cavities per module**	**No. of cav.**	**No. of klystr.**	**Cryo-modules**	**Aperture** † **radius** [mm]	**Length** [m]
$\beta = 0.65$	180	643	6	42	7	7	42.5	85.8
$\beta = 1.0$	643	3562	8	136	32	17	45	256.1
Total				178	39	24		341.9

† Used for loss calculations.

rings are welded between cells in order to minimize the Lorentz-force detuning. The main characteristics of the medium- and high-β cavities are listed in Table 4.11 and the evolution of the real-estate gradient is shown in Fig. 4.27(b).

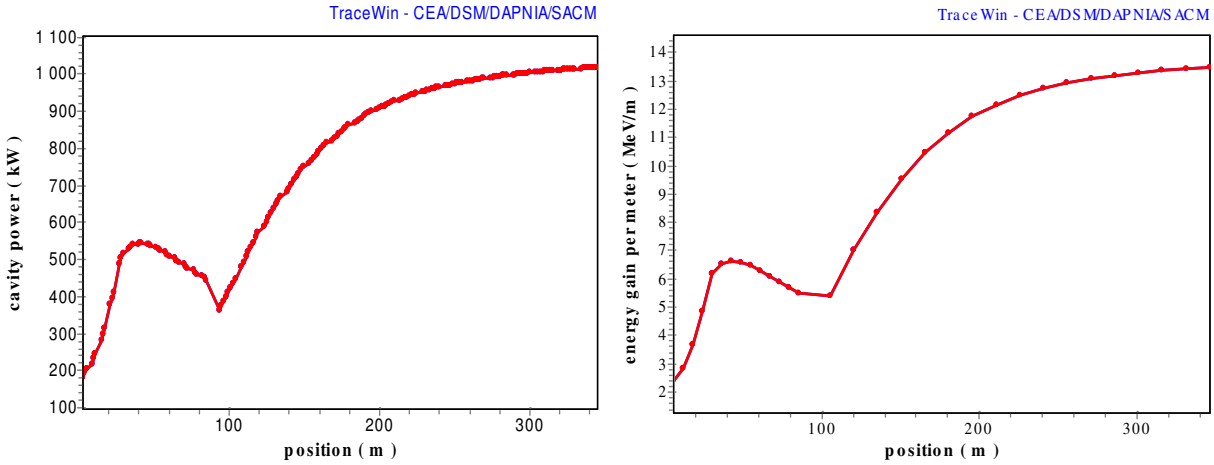

Fig. 4.27: (a) Power per coupler/cavity in the SC linac (b) Real-estate electric gradient in the SC linac

The dimensions of the cryo-modules in Table 4.14 include all cold components [cavities, helium vessel, tuner, superconducting quadrupoles, Beam Position Monitors (BPMs), steerers, etc.]. The superconducting quadrupoles operate with integrated magnetic field gradients lower than 4 T for an aperture radius of 100 mm and a length of 450 mm (see Fig. 4.28).

Table 4.14: Lengths in the superconducting linac (m)

Section	**Cavity**	**Quadrupoles**	**Cryo-module**	**Between cryo-modules**	**Period**
$\beta = 0.65$	0.692	0.45	11.450	0.8	6.125
$\beta = 1.0$	1.064	0.45	14.262	0.8	15.062

4.4 Beam dynamics

4.4.1 General approach

Beam dynamics considerations have influenced the choice of the structure parameters from the first conception stage onwards. The main guidelines have been the control of losses and the minimization of r.m.s. emittance growth ($\Delta\varepsilon_{\text{r}}$) and halo development. In order to implement these guidelines, much care has been taken to keep the following constraints: a) a zero-current phase advance always below 90°, for stability; b) a longitudinal-to-transverse phase advance ratio (with current) between 0.5 and 0.8 in order to avoid resonances; and c) a smooth variation of the transverse and longitudinal phase advance per metre.

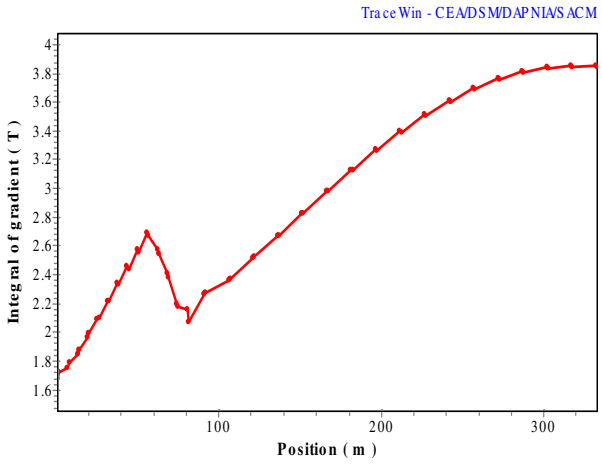

Fig. 4.28: Integrated magnetic gradient for all SC quadrupoles

The accelerator optimization has been conducted in sections while an end-to-end simulation has validated the choices and has allowed transitions to be smoothed wherever needed. Particular attention has been paid to the matching at each transition point: an initial envelope-type matching has been subsequently refined by a multi-particle type matching on a cloud of particles generated at the low-energy end.

The starting point of the simulations is the Low-Energy Beam Transport (LEBT) between the source and the first stage of RF acceleration. In this section the space-charge electric field of the quasi-DC beams is partly compensated for by the trapping of positive ions. These are created by ionization of residual gas molecules, and the rapid expulsion of the free electrons by the electric field of the beam. This partial beam neutralization influences the emittance growth and halo development, and it can significantly change the beam distribution at the start of the acceleration.

When simulations from the source were not available, two different distributions were tracked through the accelerator: a 4D waterbag and a Gaussian. The different evolution of these two distributions is expected to give a boundary to the behaviour of the 'real' beam.

Most of the simulations have been computed with 50 000 macro-particles, giving therefore an accuracy for any global quantity reported in this section of about 0.5%. The figures of merit for the beam dynamics are the losses, the r.m.s. emittance growth, and the sensitivity to errors. In the following a description of the beam dynamics in each linac section is given. Unless otherwise indicated, matching and beam transport are performed with the code packages TraceWin/Partran [81] using 3D space-charge routines. The quadrupoles are simulated with a hard-edge linear formalism. The fields in the cavities are computed via a sophisticated multi-gap model to take into account the effect of a finite bore radius. The radial dependence of the field is extrapolated with a Bessel function. Most of the simulations have been cross-checked with other codes.

4.4.2 LEBT (95 keV)

The LEBT must ensure the matching of the beam from the source to the RFQ, while minimizing the emittance growth. The choice has been made to employ magnetic lenses rather than electrostatic ones for the following reasons: a) to avoid the high-tension discharge problems of electrostatic lenses; b) the possibility of space-charge compensation; c) the positive experience with magnetic lenses in the Linac2 LEBT; and d) the availability of spare pulsed solenoid lenses from Linac2.

Simulations of the beam transport in the LEBT have been peformed with the multi-particle code PATH [82], using calculated field maps of solenoid magnets. Beam input conditions have been based on measurements of the H^+ ECR SILHI source at CEA Saclay, which had an increased emittance of

0.25 π mm mrad (normalized, r.m.s.). The beam is created with uniform density in the transverse plane, and the space-charge forces are calculated using the SCHEFF routine, imposing a circular symmetry of the space-charge field. Calculations use a linear compensation of the beam intensity to simulate the effect of space-charge neutralization. Several groups have reported successful use of this compensation model to explain measurements of beam transport lines. However, understanding and limiting the creation of beam halo will require the understanding of the non-linear aspects of the compensation process [83]. These simulations have yielded the following results:

1. The nominal beam ($\varepsilon_r = 0.25\,\pi$ mm mrad, 70 mA) can be transported and matched to the RFQ with no losses.
2. With full space-charge, emittance growth can be limited to 25% by limiting the dimension in the solenoids to avoid lens aberrations, which in turn would lead to a strongly non-linear space-charge field. Such a requirement leads to a short distance between the source and the first solenoid.
3. With 90% space-charge compensation, the emittance growth can be limited to 2%.
4. There is negligible emittance growth due to misalignments of the beam or solenoids, up to 2 mm and 20 mrad. It is required that the beam be steered into the acceptance of the RFQ.

From the simulations it is evident that beam neutralization plays a very important role in the LEBT. Calculation and measurement of the beam potential, ion oscillations, and electron oscillations by Soloshenko [84] suggest working at a pressure close to or slightly below the critical pressure (corresponding to the pressure at which the beam potential is zero). As this critical pressure is estimated to be in the region of 5×10^{-5} mbar, it is proposed that a gas injection system into the LEBT be foreseen to allow the pressure to be varied independently. The time (τ) for the production of sufficient ions through beam impact ionization is given by $\tau = 1/n\sigma v$, where n, σ, and v are the residual gas density, the beam-molecule ionization cross-section, and the beam velocity, respectively. Typical cross-sections for H_2 ionization by 100 keV protons are 2×10^{-16} cm^{-2} [85], leading to a compensation time of approximately 8 μs at 5×10^{-5} mbar. This relatively high pressure will lead to gas stripping of the H^- beam. The measured cross-sections for electron detachment of H^- to H_0 or H^+ (see Refs. [86], [87]) are shown in Table 4.15 for some gases for 100 keV H^- ions.

Table 4.15: H^- single gas stripping cross-section (in 10^{-16} cm^2) for selected gas types, for ion energies of 100 keV

	H_2 [86]	He [86]	N_2 [86]	Ar [86]	Ne [87]	Kr [87]	Xe [87]
$\sigma_{-1,0}$	4.06†	2.01	9.23	8.40	4.2	11.5	11.3

† Value from interpolation of data at 50 keV and 150 keV in Ref. [86].

The mean free path is then of the order of $\lambda = kT/\sigma P = 8.1$ m for a cross-section of 1×10^{-15} cm^2, and a pressure of 5×10^{-5} mbar at $T = 293$ K, with k being the Boltzmann constant. A 1.42 m long LEBT would then have stripping losses of >15%. If the pressure required for good compensation is of the order of 1×10^{-5} mbar, the losses would be reduced to < 4%, and lower still if low cross-section gases are used. An emittance measurement at the end of the LEBT could indicate the optimum pressure settings.

Data also exist in the same references for the double electron detachment cross-sections from H^- to H^+, but these are typically an order of magnitude smaller at these low energies, and hence are ignored. However, the double detachment from H^- to H^+ will produce a low-intensity beam of protons. If the detachment occurs outside a solenoid field, the protons will be focused into the RFQ (unless there is a strong steering force). The effect of such a beam composing less than 1% of the H^- current should not be ignored for the SPL.

4.4.3 RFQ (95 keV to 3 MeV)

The RFQ used in the SPL set-up is the RFQ of the IPHI project, which has been extensively documented in Refs. [57], [88], and [89]. The main feature of this RFQ is the capability of accepting a CW beam with varying beam current up to 100 mA. In our particular case, the reference peak beam current is 70 mA and the input r.m.s. normalized emittance is 0.25 π mm mrad.

4.4.4 Chopper line and matching to the DTL (3 MeV)

After the first stage of acceleration it is necessary to introduce a section capable of removing a few of the micro-bunches in the pulses. This operation is done at low energy with the aim of removing micro-bunches that would eventually be lost at the injection in a circular machine with a typical operating frequency of the order of some tens of megahertz. This operation is done by a fast-switching electrostatic field provided by the chopper (see Section 4.2.3). On account of the conflicting needs of high voltage and fast rise-time, the chopper is a relatively long object compared to the focusing periods in the RFQ and DTL. Housing it in the beam line implies an abrupt modification of the phase advance per metre. In order to disrupt as little as possible the continuity of the phase advance, the chopper is integrated in a FODO period with a length of 1.6 m. A total of four FODO periods assure the matching from the RFQ to the chopper and from the chopper to the DTL. The FODO period housing the chopper is also essential for the chopping action, as it amplifies the effective kick of the chopper (5.3 mrad kick for 400 V effective voltage) by adjusting the appropriate phase advance for the beam centre (almost 90° from the centre of the chopper to the middle of the dump). With 11 quadrupoles, already existing at CERN, and three new buncher cavities in the chopper line, the beam can be chopped with only 0.3% of the particles remaining in the empty bunches and with an emittance increase of $< 20\%$ in the three planes of the unchopped beam. The losses of the unchopped beam take place partly on the chopper plates (1%) and partly at the dump (6%). It should be noted that the dump can be used also as a rudimentary collimator to limit the emittance growth to a few per cent at the expense of increased beam loss at the dump (12%). The envelope of the chopped and unchopped beam is shown in Fig. 4.29.

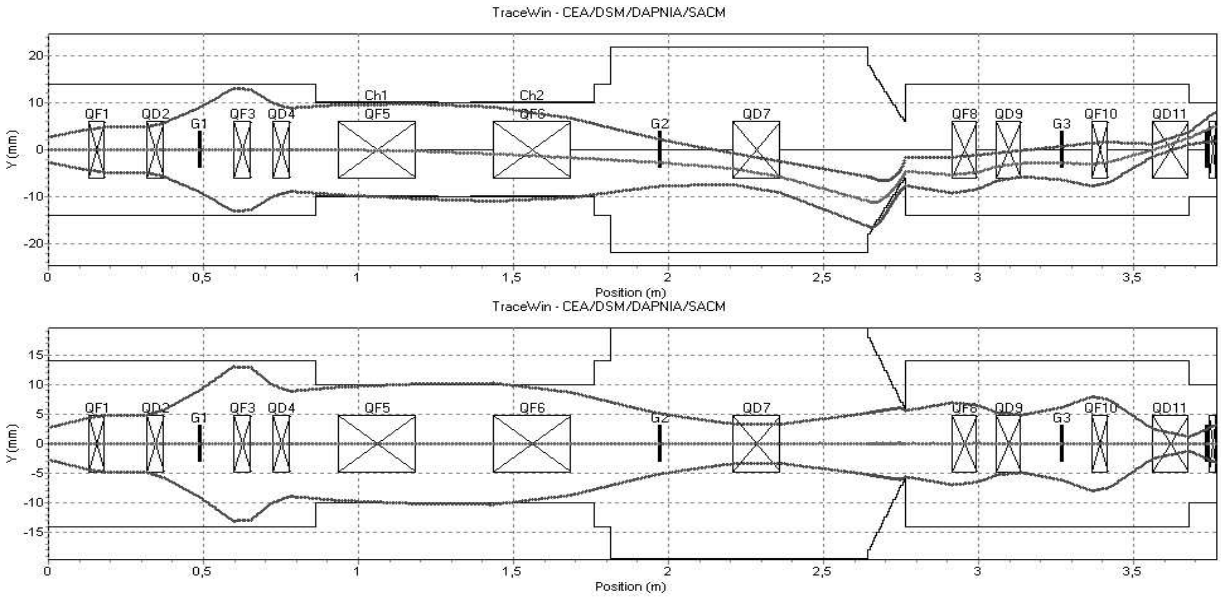

Fig. 4.29: Beam envelope in the chopper line: chopped beam (top) and unchopped beam (bottom)

4.4.5 DTL, CCDTL and SCL (3 MeV to 180 MeV)

The dynamics and the structure parameters of the acceleration section between 3 MeV and 180 MeV have been optimized as a whole, although this part is composed of three different RF structures. We have designed the three structures globally, taking into account that a variation of parameters in one of them must be followed by the others. The longitudinal phase is ramped up in the first two metres of the DTL from $-30°$ to $-20°$ and then kept constant until the end of the SCL. At the transition between tanks and/or structures where one or more gaps are 'missing', the phase of the neighbouring cavities is adjusted to cope with the transition and to ensure a smooth variation of the longitudinal phase advance. The transverse confinement and matching is provided by a system of quadrupoles, using an FFDD configuration in the first DTL tank (2.56 m) and an FD configuration afterwards ($>$ 10 MeV). The period length changes from $2\,\beta\lambda$ at low energy to $11\,\beta\lambda$ at 90 MeV. The reason for starting with an FFDD configuration is purely technical and is due to the difficulties of achieving a strong enough integrated gradient in the limited space available for the quadrupole in the first drift tube (45 mm mechanical length available for a quadrupole). A scheme with FD configuration everywhere has been studied and it gives some advantages with respect to sensitivity to beam errors [90]. However, since it is not the baseline scheme, it will not be presented in this report.

The transverse and longitudinal (phase) r.m.s. envelopes for a matched Gaussian beam generated at the entrance of the DTL are shown in Fig. 4.30. The transitions between focusing structures preserve the continuity of the phase advance per metre.

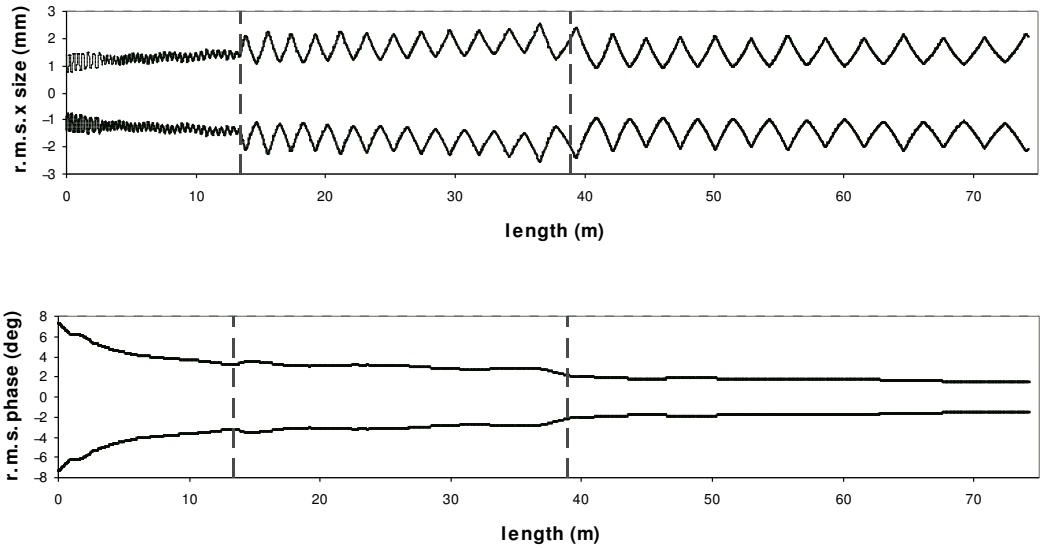

Fig. 4.30: Transverse, x (top) and phase (bottom) r.m.s. envelopes along DTL, CCDTL, and SCL. The dotted lines mark the transition between structures.

At all times during the acceleration (except at one point), the ratio of transverse to longitudinal phase advance is chosen to respect Hoffmann's stability criterion [91]; hence the emittance exchange during acceleration is under control. Table 4.16 summarizes the r.m.s. emittance growth in each section for a Gaussian and a uniform input beam distribution without errors.

4.4.6 Superconducting section (180 MeV to 3.5 GeV)

To minimize r.m.s. emittance growth and halo formation, several techniques have to be combined to compute the parameters of the channel. For this purpose, the same principles as introduced in the normal-conducting part are applied for the superconducting section: a) the phase advance per metre (average beam size) has to be kept as smooth as possible to maintain the equilibrium of the beam; and b) the

Table 4.16: r.m.s. emittance increase between 3 MeV and 180 MeV for initially uniform and Gaussian beams

	Plane	DTL [%]	CCDTL [%]	SCL [%]	Total [%]
Gaussian	x	5.5	0.1	2.8	8.4
	y	4.3	1.8	2.6	8.7
	z	4.6	1.4	0.3	6.3
Uniform	x	1.4	0.14	0.7	2.2
	y	−1	3.3	0.3	2.6
	z	4	1.1	0.6	5.7

r.m.s. beam parameters have to be matched at each transition to avoid mismatching, which would induce emittance growth. The evolution of the phase advances per metre are shown in Fig. 4.31 (a). The focusing lattice is FDO.

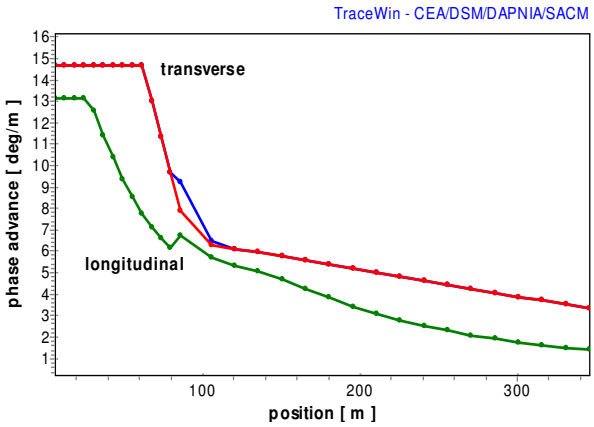

Fig. 4.31: (a) Transverse and longitudinal zero-current phase advance per metre

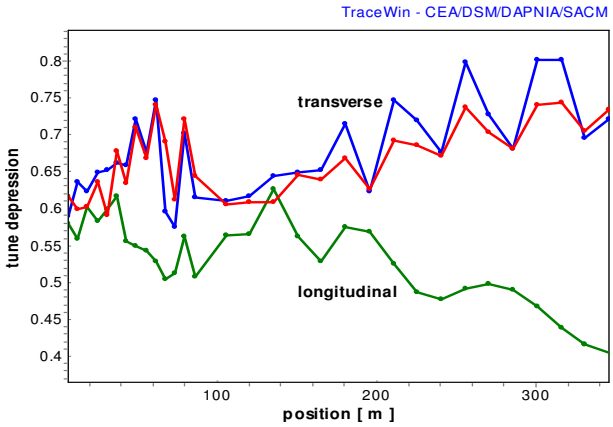

(b) Transverse and longitudinal tune depression for 65 mA

A Gaussian distribution cut at 4 σ with a transverse normalized r.m.s. emittance of 0.32 π mm mrad and a longitudinal normalized r.m.s. emittance of 0.47 π mm mrad is used at the entrance of the superconducting linac. The evolution of the beam is simulated from 180 MeV to 3.5 GeV using macro-particles. The peak current is 65 mA for a bunch frequency of 352.2 MHz. No significant r.m.s. emittance growth is observed in the simulations. Figure 4.32 shows the evolution of the 4-σ envelopes.

4.4.7 End-to-end simulations

End-to-end simulations have been carried out from 95 keV to 3.5 GeV. As the effect of beam neutralization on the low-energy end is still not completely understood, the end-to-end simulations start with a generated matched beam at the RFQ input. The beam contains 50 000 macro-particles carrying a current of 70 mA, at an energy of 95 keV with an r.m.s. relative energy spread of 0.5%, a value that we expect from the source extraction voltage jitter. The transverse emittance is assumed to be 0.25 π mm mrad (normalized, r.m.s.), with the beam being symmetrical in the two planes. Two distributions have been generated: 4D waterbag and Gaussian. We expect the behaviour of the beam to be bound between the evolution of these two distributions. The results of the tracking, without errors, are reported in Tables 4.17 and 4.18.

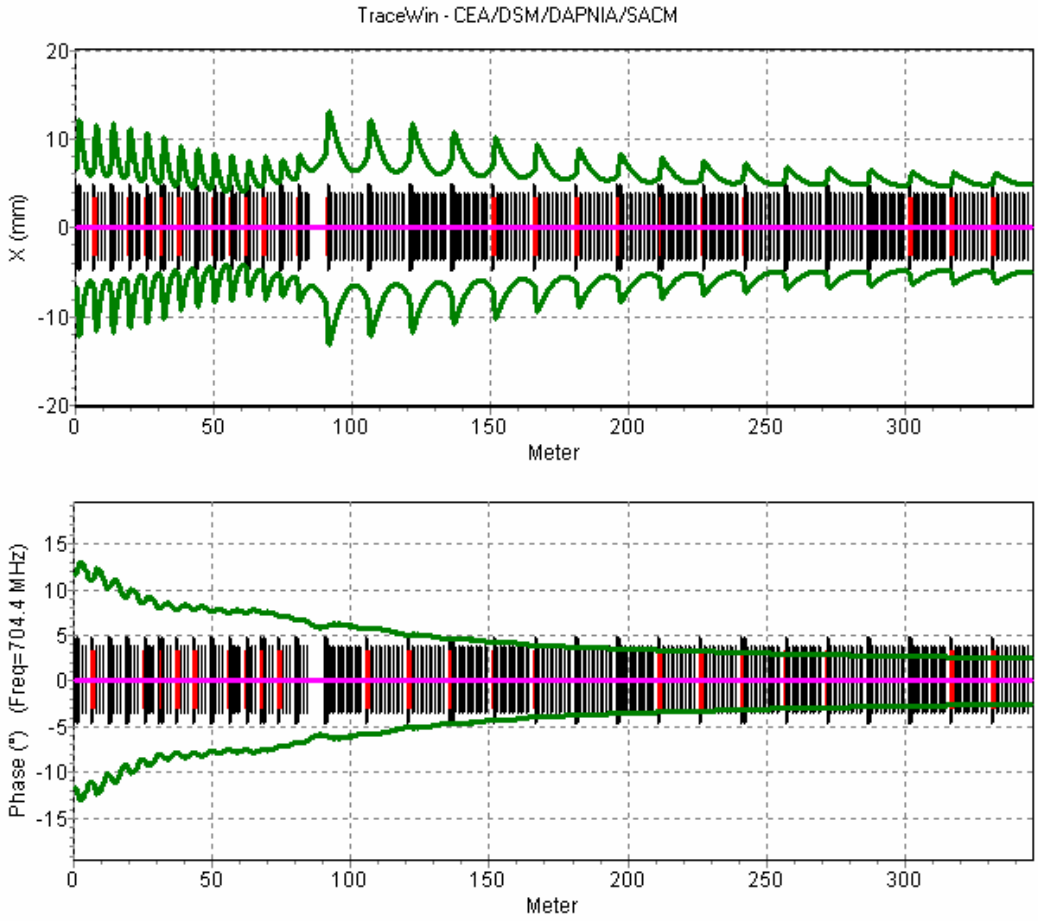

Fig. 4.32: 4-σ beam envelopes in the horizontal (x) and longitudinal (phase) plane

Table 4.17: r.m.s. emittance growth and losses for an initially uniform distribution (end-to-end simulation)

	RFQ	**Chopper**	**DTL**	**CCDTL**	**SCL**	**SC**	**Total**
Output energy [MeV]	3	3	40	90	180	3500	–
ε_x growth [%]	9.3	19.5	3	–0.4	1.5	0.3	36
ε_y growth [%]	8.4	5.8	11	2	7.7	0.4	39.7
ε_z growth [%]	–	14.7	8.2	0.5	1.3	4	26.4
Transmission [%]	99.9	93.3	99.9	99.9	100	100	93.1
Length [m]	6	3.7	13.4	25.2	34.2	341.8	425.5

Table 4.18: r.m.s. emittance growth and losses for an initially Gaussian distribution (end-to-end simulation)

	RFQ	**Chopper**	**DTL**	**CCDTL**	**SCL**	**SC**	**Total**
Output energy [MeV]	3	3	40	90	180	3500	–
ε_x growth [%]	8.5	29.7	–2.4	0.7	0.75	0.3	40
ε_y growth [%]	10.6	1.1	20.7	1.5	8.8	0.4	49
ε_z growth [%]	–	9	11.9	0.3	0.9	4	25
Transmission [%]	99.6	91.1	99.9	100	100	100	90.7
Length [m]	6	3.7	13.4	25.2	34.2	341.8	425.5

4.4.8 Error studies

The gradient and alignment errors quoted in the following are based partly on the experience at CERN and partly on already measured results of prototypes. They also correspond well to the error margins used for the SNS project [15].

4.4.8.1 Method

Two families of errors have to be considered.

- *Static errors*: the effect of these errors can be detected and cured with appropriate diagnostics and correctors. For example, beam position measurement coupled with steerers can compensate for quadrupole or cavity misalignments. The correction strategy should be known to be able to estimate the impact of static errors on beam dynamics. The effect of the static errors depends on the control system.
- *Dynamic errors*: the effect of these errors is assumed to be uncorrected. Fortunately, they usually have lower amplitude than static errors. There are, for example, the vibrations or the RF field variations (in phase or amplitude). They are responsible for beam oscillations around the corrected orbit.

For both static and dynamic errors a uniform distribution was chosen with estimated maximum error amplitudes of $\pm A$. The r.m.s. value is then given by $A/\sqrt{3}$. If the real distribution of errors turns out not to be uniform, one should consider the study valid for the equivalent r.m.s. value.

For reasons related purely to the availability and the location of manpower, the error study has been made for the normal-conducting and superconducting sections independently. The outcome of the error study of the normal-conducting part has been taken as an input beam jitter for the superconducting part. The results of each part (normal-conducting and superconducting) are reported in the following.

4.4.8.2 Normal-conducting section

The error study for the normal-conducting part has been done by tracking a Gaussian distribution, containing 50 000 particles over 1000 different linacs with random errors uniformly distributed within the values given in Table 4.19. No correction scheme has been implemented. The results are reported in Table 4.20.

Table 4.19: Total error amplitudes used in the normal-conducting section

Quadrupole gradient	$\pm 0.5\%$
Quadrupole displacement	± 0.1 mm
Quadrupole rotations (x,y)	± 0.5 deg
Quadrupole rotations (z)	± 0.2 deg
Cavity field phase	± 1.0 deg
Cavity field amplitude	$\pm 1.0\%$

Table 4.20: Sensitivity to errors in the normal-conducting section, average r.m.s. emittance increase, r.m.s. energy jitter assuming 4 MW beam power

	$\Delta\varepsilon_x/\varepsilon_x$ av. [%]	$\Delta\varepsilon_y/\varepsilon_y$ av. [%]	$\Delta\varepsilon_z/\varepsilon_z$ av. [%]	ΔE r.m.s. [keV]	$\Delta\phi$ r.m.s. [deg]	**Losses** [W]
All errors	10.4	12.7	17.3	± 262	± 1.7	0.3

4.4.8.3 *Superconducting section*

The transport of 10^5 macro-particles has been simulated for each of 500 different linacs in order to compute statistics and to get a cumulative distribution of the beam which is represented by more than 5×10^7 macro-particles. For each linac, all the errors, whose amplitudes are listed in Table 4.21, are combined. In a first stage, no input beam error is assumed.

Table 4.21: Total error amplitudes used in the superconducting section

	Static	**Dynamic**
Quadrupole gradient [%]	±0.5	±0.05
Quadrupole displacement [mm]	±0.5	±0.01
Quadrupole rotations (x,y) [deg]	±0.25	±0.005
Quadrupole rotations (z) [deg]	±0.5	±0.05
BPM accuracy [mm]	±0.1	
Cavity displacement [mm]	±0.5	±0.01
Cavity rotations (x,y) [deg]	±0.08	±0.005
Cavity field phase [deg]		±1.0
Cavity field amplitude [%]		±1.0

For the transverse alignment, two (horizontal and vertical) steerers are located in the second quadrupole of each doublet. They are associated with two Beam Position Monitors (BPMs), located in the middle of the following doublet, which measure the beam centre in both planes. This scheme is repeated for each period. No longitudinal correction has been assumed. Assuming a normal-conducting front-end without errors one finds that:

(a) the r.m.s. residual orbit along the machine due to dynamic errors and BPM imperfections (misalignments and measurement errors) is limited to 0.28 mm;
(b) no losses are observed;
(c) the r.m.s. emittance growth, relative to a linac without errors, amounts to an average of 27%, 26%, and 6% in the x, y, and z planes, respectively;
(d) the r.m.s. output energy and phase jitter are 1.24 MeV and 0.52°, respectively.

The above study has been repeated including a beam energy and phase jitter at the linac input. This is supposed to simulate the residual longitudinal errors from the normal-conducting part. Different error sets have been simulated to establish a limit for the jitter coming from the normal-conducting part. For each of the 500 linacs, the jitter values are randomly set between $\pm k\Delta E_\mathrm{m}$ and $\pm k\Delta\phi_\mathrm{m}$ with ΔE_m and $\Delta\phi_\mathrm{m}$ representing the maximum energy and phase jitter amplitudes at the SCL output, respectively. They have been assumed as $\Delta E_\mathrm{m} = 1.16$ MeV (maximum, uniform distribution) and $\Delta\phi_\mathrm{m} = 12.6°$ (maximum, uniform distribution) at 352.2 MHz. These values turned out to be too pessimistic and thus the parameter k is used to reduce them. The results are summarized in Table 4.22.

In order to avoid any beam loss in the superconducting part of the linac and assuming the errors of Table 4.21, the maximum remnant energy and phase errors at the output of the normal-conducting parts should be lower than 380 keV and 4°, respectively, for a uniform distribution. The equivalent r.m.s. values should be lower than 220 keV and 2.4° (352 MHz), which is more or less fulfilled by the simulation results for the normal-conducting section in Table 4.20. Assuming these limits, the simulations of the superconducting section predict zero beam loss when combining transverse and longitudinal errors. The corresponding energy and phase jitter in this case amount to r.m.s. values of 0.65° and 1.2 MeV.

Table 4.22: r.m.s. emittance growth and losses in the superconducting section due to statistical errors for different values of input energy and phase jitter assuming 4 MW beam power

k	0	0.125	0.25	0.325	0.5	0.625
$\Delta E_{\text{input, max}}$ [keV]	0	145	290	377	580	725
$\Delta\phi_{\text{input, max}}$ [deg]	0	1.56	3.15	4.09	6.3	7.87
ε_x growth [%]	+27	+35	+38	+42	+51	+60
ε_y growth [%]	+26	+35	+38	+44	+56	+71
ε_z growth [%]	+6	+10	+17	+30	+62	+142
Average losses [W]	0	0	0	0	4.35	199.5

4.5 Auxiliary systems

4.5.1 Transfer line

At the end of the superconducting linac section, the bunches are about 15 ps long and have an energy spread of the order of 4 MeV. To reduce space-charge effects and energy jitter at the accumulator injection, the bunch length has to be increased in the transfer line by at least a factor of 10, and the energy spread reduced by the same factor. This is achieved by two bunch rotation systems made of 700 MHz $\beta = 1$ elliptical cavities identical to the ones used in the last section of the superconducting linac. The voltage to be applied for stretching the bunch in phase at the end of the linac depends on the length of the transfer line and the energy acceptance of the accumulator RF system. For the time being we assume injection into the ISR tunnel as detailed in CDR1 [3]. For this scenario, the first bunch rotation system (16 cavities, two cryo-modules) is placed at the linac exit to increase the energy spread in such a way that in the following long drift the bunch length is stretched up to the required value. The second bunch rotation section (two cavities) reduces the energy spread for injection into the RF bucket of the accumulator ring. The voltage on the bunch rotation cavities and their relative position depends on the longitudinal beam emittance at the linac exit. In the final layout, it can be re-adjusted for an effective longitudinal emittance that takes into account the effect of energy and phase jitter (Section 4.4.8). The first bunch rotation section, 29.4 m long, will be placed inside the linac tunnel. The second bunch rotator will be placed after 270 m. The general layout of this line is described in Table 4.23. The beam dynamics is calculated starting with a distribution of 50 000 particles at the entrance of the superconducting linac section. Phase and energy spread are presented in Fig. 4.33 and the corresponding phase-space distributions are shown in Fig. 4.34.

Table 4.23: General layout of the transfer line

Element	**Length** [m]	**No. of cavities**	**No. of focusing periods**	**Cavity parameters**
Bunch rotation 1	29.4	16	2	12.6 MV/m
Drift	272.0		18	
Bunch rotation 2	4.9	2	1	10.7 MV/m
Total	306.3			

As an alternative, we have designed a transfer line which does not make use of the first bunch rotation but lets the beam de-bunch under the effect of the initial energy spread. This approach results in a longer line but saves 16 superconducting RF cavities. The line would then contain 48 focusing periods over a length of 730 m and only one five-cell cavity with an effective voltage of 11 MV for the final bunch rotation. For the time being there is space foreseen in the linac tunnel to accommodate two more cryo-modules for the active bunch rotation at the end of the linac. However, since it is likely that the location of the accumulator ring will change in future design revisions, the cavities and RF systems needed for the bunch rotation are not included in the parameter lists of this report.

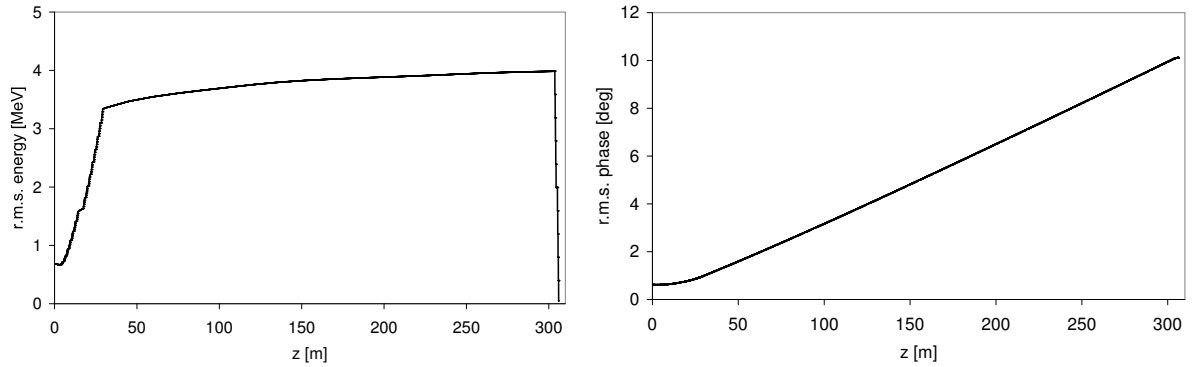

Fig. 4.33: Energy (left) and phase width (right) along the transfer line

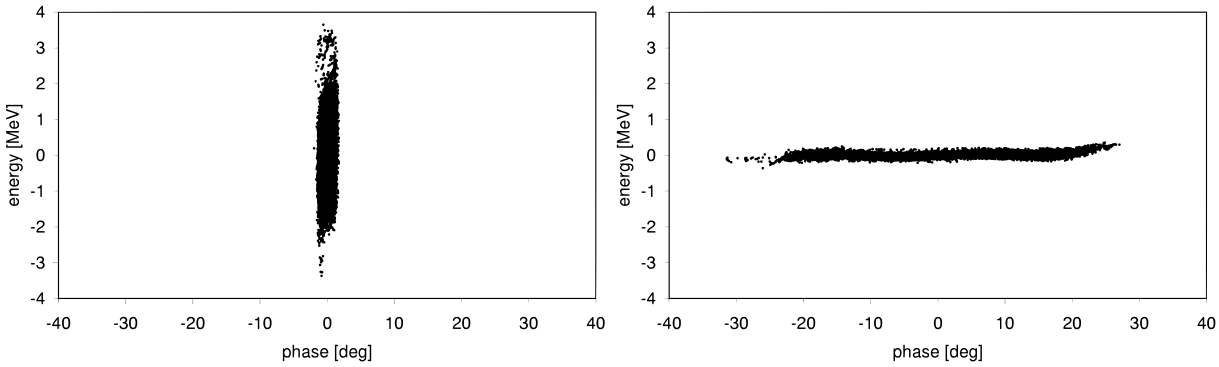

Fig. 4.34: Longitudinal phase space before (left) and after (right) the transfer line

At 3.5 GeV the minimum arc radius to avoid H^- stripping is $\approx$ 220 m. This number assumes a dipole filling factor of 60% in the arc and a loss level due to H^- stripping of 0.1 W/m (compare Chapter 6, Section 6.1.2). The current understanding of H^- stripping due to black-body radiation will require cooling of the transfer-line beam pipes to $\approx$ 150 K (see also Chapter 6, Section 6.1.2).

4.5.2 Pulsed operation and servo-system stability

The studies for the CDR1 [3] addressed most of the principal problems arising from pulsed operation and remain valid for the present revised design of the SPL.

4.5.2.1 Lorentz detuning

In CDR1 [3] it was planned to use cryostats, couplers, and other hardware from the decommissioned LEP superconducting RF system. The cavities were to be modified and fitted with stiffeners to enable medium-β acceleration and operation in pulsed mode. At the time of publication of CDR1, the details of these stiffeners and with it the resulting stiffness along with the mechanical frequencies of the cavity–tank–tuner system (possibly weighted by the couplers) were not known. Since these are key parameters for the mechanical system behaviour, no detailed analysis concerning Lorentz detuning could be undertaken, relying on definite progress in the framework of TESLA [92], now absorbed in ILC [93], and SNS [15] which will very probably pave the way. The same argument holds for the present design.

Once fully equipped prototype cavities really exist and are well characterized in terms of Lorentz-force detuning strength, frequency and mechanical Q-value of the principal mechanical mode(s) of the cavity–tank–tuner system, one can incorporate recent progress in the field of fast piezo-tuners [94] to reduce their effect. At this stage more detailed simulations have to be done. Possible modifications of the mechanical cavity design have to be undertaken if the simulations with all cavity errors and beam

show insufficient performance. For the time being, the developed computer code SPLinac [95], [96] considers only one principal mechanical mode since the LEP cavities were essentially detuning sensitive to the lowest longitudinal mechanical mode around 100 Hz. Should the new cavities have more than one essential mode, the program has to be upgraded for multiple mechanical modes; the same is true if the piezo-tuner corrections cannot be expressed by a simple scaling but show a time domain behaviour of their own. Then detailed measurements with artificial mechanical excitation and pulsed high RF fields have to be done.

In the frame of the HIPPI Collaboration [50], two different $\beta = 0.47$ elliptical cavities will be tested in pulsed mode in a horizontal cryostat at Saclay. At this low beta, the Lorentz-force detuning should be more severe than for the $\beta = 0.65$ and $\beta = 1.0$ cavities, which are foreseen for the SPL, and so the set-up, complete with couplers and tuners, should give a good estimate for the dynamical behaviour of the SPL cavities.

The extra power needed to combat the effects of Lorentz-force detuning is estimated (from SNS) to be in the area of 30%. This additional power is only taken into account for the calculation of the total SPL power requirements, quoted in Table 5.9 and in the parameter list in the Appendix.

4.5.2.2 System errors and noise

In CDR1 [3], simulations [97] were done with SPLinac based on a hypothetical set of test noise configurations. These can be created by vacuum pumps or cryogenic compressors (coherent), ground-movement and cryogenic liquid or gas movements (incoherent), and other sources. It should be noted that the mechanical conditions of the cavity–tank–tuner system combined with information on the noise sources (spectral density for noise, amplitude for discrete lines) are decisive for definite results. The simulations for CDR1 [3] showed that this effect is no major obstacle, hence the same can be expected for the present design. All RF error sources—like scatter in the input coupling strength Q_{ext} of the power couplers (e.g., observed in the LEP superconducting RF system), error distributions in the power splitters, and amplitude and phase errors in the RF vector sum—have to be included in these simulations to determine how far the resulting beam quality is affected with regard to particle losses and longitudinal emittance growth.

4.5.2.3 Control instability for several pulsed cavities with RF vector-sum feedback

Numerical simulations with SPLinac pointed to a control instability that can develop above a certain cavity field level for a pulsed RF system with Lorentz detuning sensitive cavities where more than one cavity is driven by the same high-power source and the vector sum of the cavity fields is fed back for control.

A mathematical analysis [98] using an only slightly simplified model confirmed this chaotic effect and excludes a computer simulation artefact. From this analysis it became clear that the origin of this instability is the lack of control over all individual cavities since we have only a unique ‘knob’, the incident RF wave, but many degrees of freedom, one per cavity. Therefore even for a perfect RF vector sum the distribution of the ‘work-load’ between cavities cannot be influenced and may diverge while respecting the sum. To remedy this situation and suppress the possibility for this instability, one ‘knob’ per cavity becomes essential.

A straightforward solution is the use of one transmitter per cavity, but the financial implications become an issue. In keeping a single transmitter for several cavities, one solution consists in the use of high-power phase and amplitude modulators [99] as already tested at CERN [100], [101] (Fig. 4.35), allowing the amplitude to be decreased and the phase of the incident wave to be turned towards an individual cavity in a limited way. The technical price to be paid is a permanent small over-power, finally wasted. In this set-up the main adaptations required to respect the vector sum are still done by the common transmitter, but the modulators compensate for individual cavity deviations from the average.

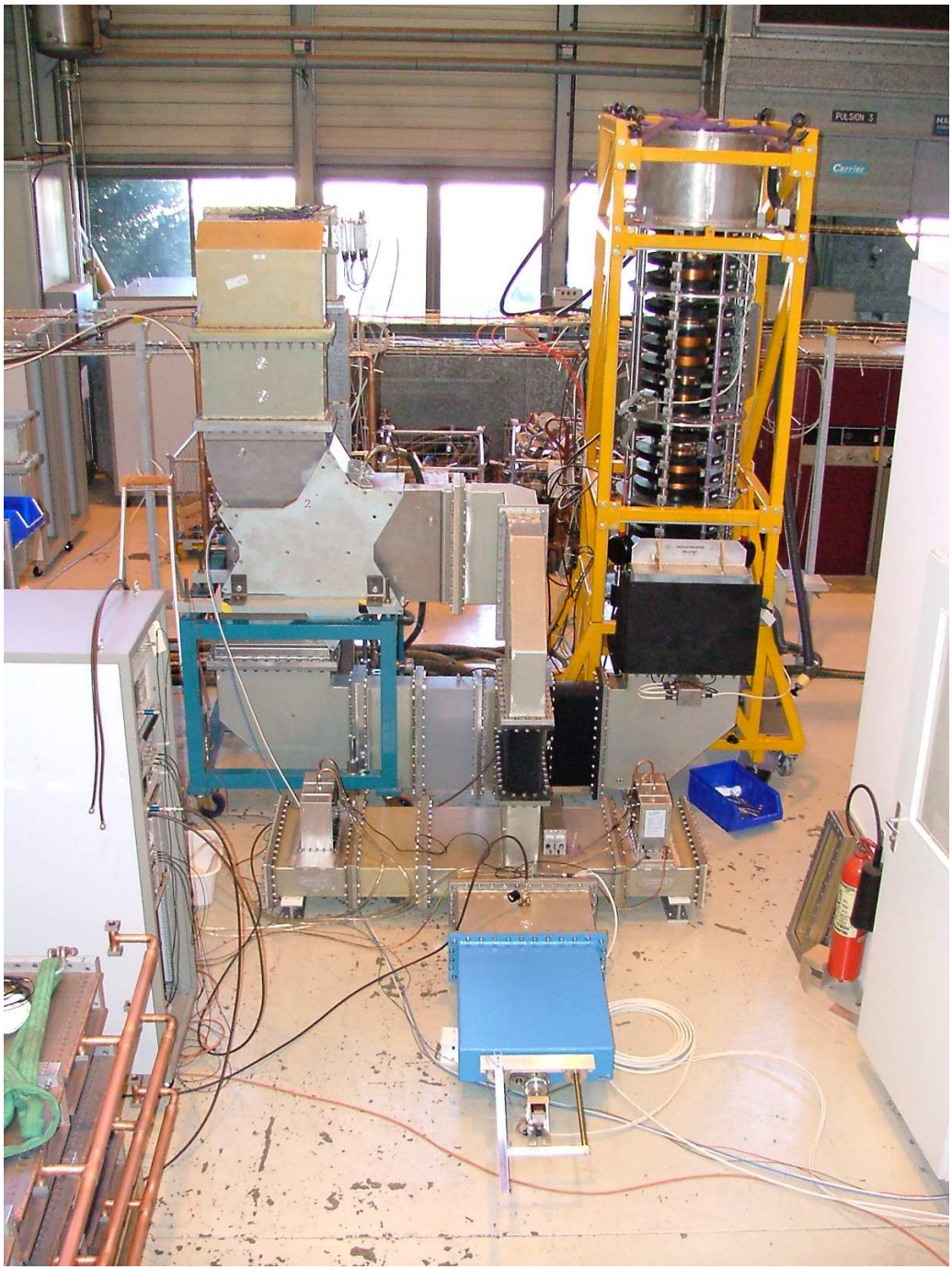

Fig. 4.35: High-power tests of the amplitude and phase modulator, using a 300 kW/400 MHz LHC klystron and a sliding waveguide short circuit as load

This choice has the additional advantage of also allowing the correction of the static errors in the power splitters and Q_{ext} without having to create the possibility for local adjustment.

Fast piezo-tuners will allow compensation of Lorentz-force detuning to a good degree. Once included in the RF chain, they will automatically reduce differences in tuning between cavities and can even be trimmed for this purpose with an additional controller. Therefore they can certainly take over part of the task of the above-mentioned phase and amplitude modulators. However, whether this compensation is sufficient to drop the phase and amplitude modulators completely, while leaving the remaining static errors unchanged, has to be explored by further R&D.

4.5.3 Diagnostics

Instrumentation for the SPL is a highly challenging issue because of two major complications.

1. The acceptable beam loss of 1 W/m requires diagnostics capable of detecting unwanted particles both in the transverse and longitudinal plane with a sensitivity of down to 1×10^3 particles per bunch (at 3.5 GeV).
2. The high beam power is destructive to all intercepting devices.

The first issue is being addressed by developing dedicated diagnostic devices capable of measuring remaining, unchopped beam as well as tails in the transverse distribution (beam halo). The second issue requires beam measurements to be done with a dedicated diagnostic beam ('commissioning' or 'pilot' beam) [102].

During the commissioning of the various sections, transverse and longitudinal emittances need to be measured as well as energy and energy spread in order to adjust phase and voltage for each RF system. For this purpose a dedicated diagnostic line can be re-used from the IPHI project [57]. This line, designed to characterize the beam at the exit of the RFQ at 3 MeV, may be used for the commissioning of the various stages of the normal-conducting linac after modifications for the use at higher beam energy. Figure 4.36 shows the diagnostic line, which comprises time-of-flight energy measurement, wire scanners, beam position monitors, and a spectrometer dipole. The measurement programme has been simulated for the 3 MeV chopper line [103].

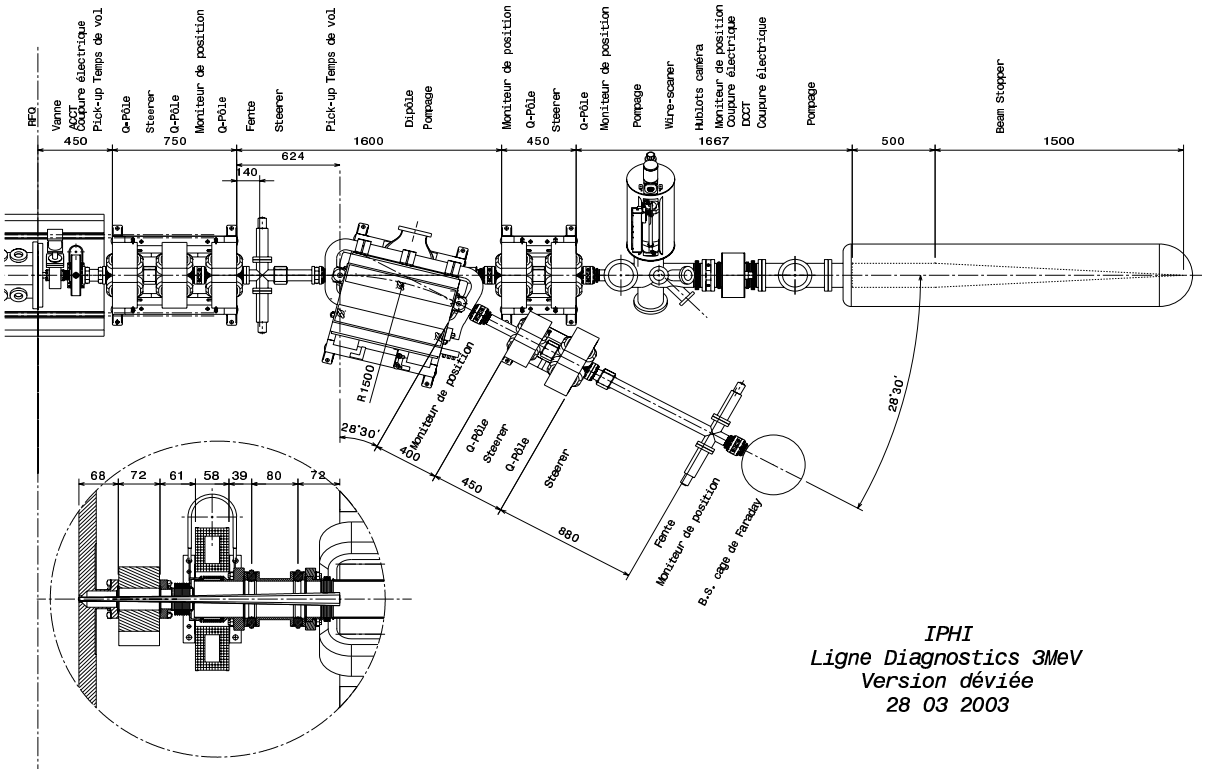

Fig. 4.36: Beam diagnostic line for the 3 MeV front-end provided by the IPHI Collaboration

The source current is measured by means of a retractable Faraday cup. Beam position and size are monitored by a beam profile monitor in the LEBT. The current is measured by a beam current transformer the position of which remains to be defined. The details of the LEBT are given in Section 4.2.1.

The MEBT consists of a beam chopper with matching sections upstream and downstream of the device. Beam current transformers between the first and the last pair of quadrupoles in the matching sections monitor the transmission through the line. A dedicated halo monitor (see Fig. 4.37) has been developed to verify the correct operation of the chopper and to provide a transverse image of the beam [104]. In the transverse plane, the high dynamic range of 10^6 allows the simultaneous measurement of the thinly populated beam halo and the beam core populated with 10^8 ions. The halo monitor is at present in the final stages of construction and testing.

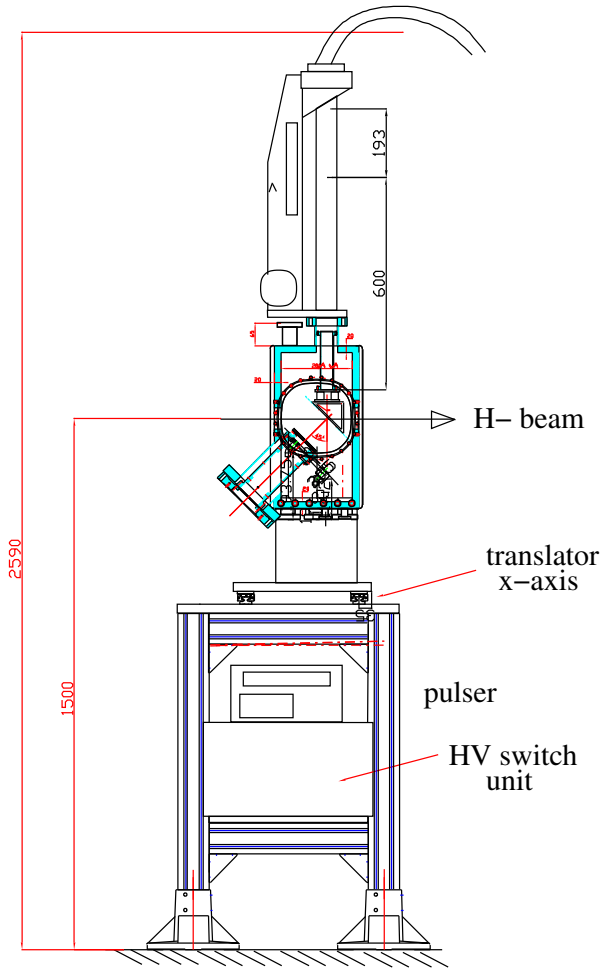

Fig. 4.37: Side view of the beam shape and halo monitor. The system is based on the production and imaging of secondary electrons that are produced as the H^- beam passes through a thin carbon foil.

The normal-conducting part of the linac, consisting of drift-tube linac (DTL), cell-coupled drift tube linac (CCDTL) and side-coupled linac (SCL), requires diagnostics for the setting-up of each section as well as permanently installed equipment for day-to-day operation. During operation, we require a measurement of beam current, position and profile at various locations along the normal-conducting linac. This is accomplished by beam current transformers and either secondary electron emission monitor (SEM) grids or wire scanners. The following locations have been identified for these standard diagnostics. For the DTL, we require a measurement after each of the three tanks. In the CCDTL, a measurement after each of the eight modules appears appropriate. For the SCL, we foresee a set of measurements after each of the four modules. This yields a total of 15 locations for current, profile, and position measurement. The possibility of designing an emittance measurement line at the end of the warm linac is under study.

Measurements of the transmission as well of beam shape and position will also be required in the superconducting part of the linac. Unlike the SNS linac, where each cavity is housed in its own cryostat and the diagnostics is installed in the warm sections in between, the SPL layout is based on long cryostats. This requires most of the diagnostics to be housed inside the cryostats, as is the case for the International Linear Collider (ILC) design. A wealth of beam diagnostics for superconducting linacs has been designed in the frame of the ILC study [105]. Various options for beam position monitors working at cryogenic temperature appear viable, while diagnostics with movable parts (e.g., laser wire scanners) need to be installed in warm sections.

4.6 Radio frequency sources

The SPL will use two different RF frequencies: 352.2 MHz up to an energy of 90 MeV and 704.4 MHz for the rest of the linac. For the 352.2 MHz section, parts of the decommissioned LEP RF system have been put into storage, including 20 LEP klystrons together with waveguide distribution systems, RF loads, and circulators. The LEP klystrons were originally used in CW operation and are specified for an average RF power of 1.3 MW. First tests of pulsing these klystrons have been successfully performed at CERN [106] using the original LEP power converters (4 MW, 100 kV DC, 40 A). For future operation in Linac4 and SPL, new, more compact pulsed power converters are foreseen, which are currently under development at CERN in collaboration with the Centre for Advanced Technology (CAT, Indore, India). After the successful testing of fast phase and amplitude shifters at CERN [101], [107], the decision was taken to use multi-megawatt klystrons at 704.4 MHz to feed several superconducting cavities via waveguide splitters and to adjust phase and amplitude for individual cavities with these devices.

High-power ($\geq$ 4 MW) long-pulse ($\geq$ 0.1 ms) klystrons at 704.4 MHz can be easily developed starting from similar units used in other projects. Different klystron manufacturers have already provided quotations for devices with peak power of 4–5 MW and 10% duty cycle.

Even though the RF duty cycle for nominal operation at 5 MW beam power only amounts to <6%, the RF sources are specified for 10% duty cycle. This offers an operational safety margin that allows the regular pulse length to be extended in case the source current does not reach its maximum specified value. Assuming a maximum klystron power of 5 MW and standard two-way power splitters, 44 klystrons at 704.4 MHz are needed to cover the peak power of 150 MW for this frequency. In addition, 14 LEP klystrons are foreseen for the 11.3 MW needed at 352.2 MHz for the normal-conducting part up to 90 MeV. Table 4.24 lists the power requirements for the two frequencies and for the normal and superconducting sections [108]. The maximum peak power is dimensioned such that the klystrons still have a minimum safety margin of 25–30% with respect to their maximum rated values. The values quoted in Table 4.24 do not take into account the extra average power needed for the compensation of Lorentz-force detuning in the superconducting cavities. For this purpose an extra 30% margin is added in Table 5.9, which lists the total power requirements for the SPL. On average the 5 MW klystrons have to deliver 3.4 MW. Each klystron is protected by a circulator from the reflected power during charging and discharging of the superconducting cavities.

In addition to the klystrons, three tetrodes will be used for the buncher cavities in the chopper line. For this purpose five 50 kW CW tetrodes (Thomson TH571B) have been recovered from the SPS, including three control systems. In pulsed mode one can expect up to 100 kW from these devices, which will have to deliver only $\approx$ 20 kW for each of the buncher cavities.

4.7 Cryogenic infrastructure

4.7.1 General considerations

The design of the superconducting linac has changed considerably since the publication of CDR1 [3], which was based on the LEP superconducting cavities. As a consequence, the overall cryogenic system was reviewed for this report. The main difference for the cryogenic installations is the use of new super-

Table 4.24: RF sources for the SPL (without margin for control power)

No. of 352.2 MHz tetrodes	3
No. of 352.2 MHz LEP klystrons	14
No. of 704.4 MHz klystrons	44
Efficiency klystrons (η_{kl})	0.5
Efficiency power supplies (η_{ps})	0.85
Efficiency wave guide transmission (η_{wg})	0.95
Maximum no. cavities per klystron	8
Total RF peak power	161.6 MW
Average RF plug power 'neutrino baseline'†	17.0 MW
Average RF plug power 'EURISOL baseline'†	20.8 MW
Normal-conducting (NC) section	
Peak power at 352.2 MHz (copper + beam)	7.7 + 3.6 MW
Peak power at 704.4 MHz (copper + beam)	11.5 + 3.6 MW
RF duty cycle 'neutrino baseline'	3.4%
RF duty cycle 'EURISOL baseline'	4.5%
Average NC power 'neutrino baseline'	0.9 MW
Average NC power 'EURISOL baseline'	1.2 MW
Superconducting (SC) section	
Peak power at 704.4 MHz (beam)	135.2 MW
RF duty cycle $\beta = 0.65$ 'neutrino baseline'	4.3%
RF duty cycle $\beta = 1.0$ 'neutrino baseline'	4.4%
RF duty cycle $\beta = 0.65$ 'EURISOL baseline'	5.2%
RF duty cycle $\beta = 1.0$ 'EURISOL baseline'	5.3%
Cryo duty cycle $\beta = 0.65$ 'neutrino baseline'	4.4%
Cryo duty cycle $\beta = 1.0$ 'neutrino baseline'	4.6%
Cryo duty cycle $\beta = 0.65$ 'EURISOL baseline'	5.3%
Cryo duty cycle $\beta = 1.0$ 'EURISOL baseline'	5.5%
Average SC power 'neutrino baseline'†	6.0 MW
Average SC power 'EURISOL baseline'†	7.2 MW

† Without margin for Lorentz detuning.

conducting RF cavities working at 2 K, which implies the use of super-fluid helium and sub-atmospheric conditions for the cryogenic system. The SPL II cryogenic system design is based on the LHC project experience [109], on the TESLA Technical Design Report [92] and the ILC Technical Design Report [110].

The SPL II cryo-module is based on the TTF III design containing all cryogenic piping inside the module (Fig. 4.38). Although the design needs to be revised in more detail for SPL II, the TTF III approach gives a good estimate of the cryogenic system based on previous studies for superconducting linacs (TESLA and ILC). However, it is clear that any future revision of the cryostat and distribution system will have a direct impact on the final design of the cryogenic system, which will need to be addressed in coming studies. For this purpose, the list of open issues detailed in Section 4.7.4 needs to be reviewed.

4.7.2 Heat loads

As described in Section 4.3.4, the layout of the superconducting section is based on cavities matched for particle velocities of $\beta = 0.65$ and $\beta = 1.0$. These cavities will be grouped in three different cryogenic sections (or strings) as described in Table 4.25. Two different scenarios, nominal and ultimate, have been

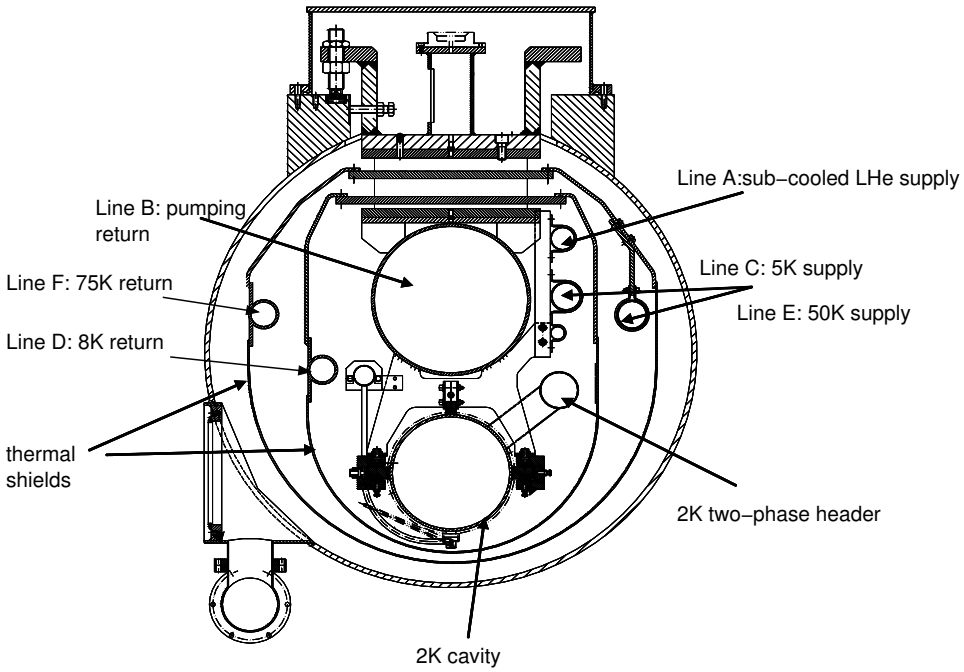

Fig. 4.38: Cryo-module cross-section with operating temperatures

Table 4.25: Nominal and ultimate SC cavity parameters for the dimensioning of the cryogenic system

Section	β	E_{acc} [MV/m] **nominal/ultimate**	Q_0 [10^{10}]	R/Q [Ω]	**Active cavity length** [m]	**Cav. per cryo module**	**No. of cryo modules**	**String length** [m]
1	0.65	19/20.9	1/0.5	290	0.692	6	7	85.8
2	1	25/27.5	1/0.5	570	1.064	8	9	135.6
3	1	25/27.5	1/0.5	570	1.064	8	8	120.5

considered for the RF parameters. These two scenarios will be used to define the maximum installed capacity required for the cryogenic system.

Most of the heat loads should, where possible, be intercepted at higher temperatures in order to limit the heat reaching the lowest temperature level, and thus ease the burden on the refrigeration system. The SPL II cryogenic system has three nominal temperature levels:

- the 2 K temperature of the cavity cold-mass structure,
- a 5–8 K level for heat interception and radiation screening,
- a 50–75 K level for a higher level of heat interception and thermal shielding.

Table 4.26 summarizes the estimated heat loads per cryogenic module for each of these levels of temperature, for the two cavity types, and for the nominal and ultimate scenarios.

The static heat loads have been rescaled from TTF measurements [92]. These measurements give an overall estimation for static losses per module. The figures have been rescaled according to the higher volume and surface of the SPL II cavities.

The RF losses considered at 2 K are proportional to the square of the electric gradient and inversely proportional to the cavity parameters Q_0 and R/Q. A 6% duty cycle has been considered for the dynamic RF losses, slightly higher than the value quoted in Table 4.24. The beam losses, directly intercepted at 2 K, should not surpass 1 W/m.

Table 4.26: Estimated heat loads in watts per module assuming a 6% duty cycle

Temperature	2 K		5–8 K		50–75 K	
Cavity β	0.65	1.0	0.65	1.0	0.65	1.0
Static loss	3.5	4.4	15.2	18.9	88.7	110.4
Beam loss	11.45	14.26	–	–	–	–
RF nom.	21.5	59.6				
HOM nom.	8.6	23.8	6.1		102	
Coupler nom.	0.64	1.79				
Total dynamic nominal	42.2	99.5	6.1		102	
RF ult.	51.9	144.2				
HOM ult.	20.8	57.7	6.1		102	
Coupler ult.	1.56	4.33				
Total dynamic ultimate	85.7	220.5	6.1		102	

In order to cope with the lack of accurate data for the rest of the dynamic load contributions at 2 K, it was decided to take into consideration two main contributions related to Higher Order Modes (HOM) and couplers. In the same way, an overall figure has been given for the dynamic contribution at 5–8 K and 50–75 K. These different contributions to the dynamic load have been calculated from the TTF TDR [92] in the following way.

- HOM and coupler loads at 2 K: the only value we know with sufficient certainty for SPL II is the RF field contribution. Thus we have used the ratios of HOM loads over RF field loads and coupler loads over RF field loads to calculate the HOM and coupler contributions for the dynamic loads of the SPL II. These ratios are quoted as 40% and 3%, respectively.
- Dynamic loads at 5–8 K and 50–75 K: in this case we have used the ratios between the dynamic contributions related to the static contributions at 5–8 K and 50–75 K. This means that the dynamic loads are 40% and 115% of the static loads at 5–8 K and 50–75 K.

The heat load coming from the superconducting magnets is considered to be negligible and does not enter the present estimations.

The installed capacities for each temperature level have been calculated as follows:

$$Q_{\text{installed}} = \max\left\{1.5 \cdot \left(1.5Q_{\text{stat}} + Q_{\text{dyn, nominal}}\right); 1 \cdot \left(1.5Q_{\text{stat}} + Q_{\text{dyn, ultimate}}\right)\right\} . \tag{4.1}$$

The installed capacity is the maximum capacity required of the nominal and ultimate scenarios. An overcapacity factor of 1.5 is applied for static loads for both scenarios. An overcapacity factor of 1.5 is applied for the nominal scenario while no additional overcapacity is applied for the ultimate scenario. Table 4.27 gives the values for the total heat loads at the three temperature levels. The installed capacity corresponds to the maximum capacity required of the nominal and ultimate scenarios.

Table 4.27: Total heat load and installed capacities for a 6% cryo duty cycle

Temperature	2 K	5–8 K	50–75 K
Static [W]	99	427	2497
Dynamic nominal [W]	1986	146	2446
Dynamic ultimate [W]	4348	146	2446
Installed capacity [W]	4496	1180	9290
Equivalent at 4.5 K [kW]		15.8	

The cryogenic system requires a total equivalent refrigeration capacity of 15.8 kW at 4.5 K, which is in accordance with the present state of the art. To compare with the ILC cryo-units (25 kW at 4.5 K), the equivalent refrigeration capacity at 4.5 K is significantly smaller. For the cold compressor system, the required capacity of 4.5 kW at 2 K — quite similar to ILC (4.6 kW at 2 K) — also corresponds to the present state of the art.

4.7.3 Cryogenic system

The SPL II cryogenic system is based on the ILC cryogenic system. The same working principles and process layout have been applied. Scaling factors for the definition of the cryogenic system have been used where possible. However, the description presented here does not include all the technical parameters which need to be addressed for a technical design report.

Figure 4.39 shows the cooling scheme for the superconducting section. The present layout has three main strings of cryo-modules, one for $\beta = 0.65$ cavities and two for $\beta = 1$ cavities (see Table 4.25). The compact layout has been motivated mainly by filling factor considerations.

Both thermal screens at 5–8 K and 50–75 K are cooled in series (lines C–D and E–F, respectively). The cooling at 2 K is supplied in parallel. The cavities are immersed in a saturated super-fluid helium bath filled through the 2 K two-phase header by gravity. The saturated 2 K helium is produced by expansion of the sub-cooled liquid (line A) through a Joule Thomson valve. At the interconnection of each cryo-module, the two-phase header is connected to the pumping return line (line B).

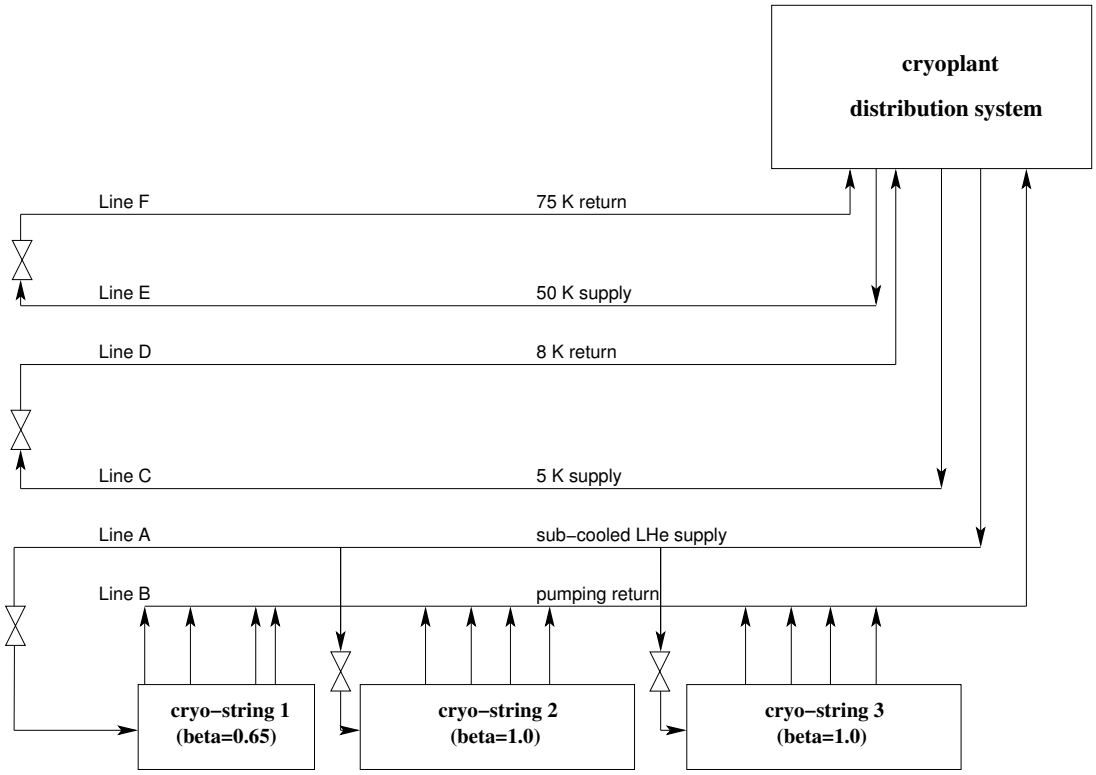

Fig. 4.39: Cooling scheme of the cryogenic system

The cold boxes will be placed in a dedicated building close to the centre of the superconducting section. A standard CERN metallic wall construction of approximately 1000 m^2 is foreseen (building SDH). It contains the two cold boxes, electrical and controls cabinets and some additional space for unloading. A composed distribution cryogenic line is required to link the cold boxes to the cryo-module lines at the higher end of the superconducting linac section. This connection requires a special shaft.

For the compressor, a standard CERN concrete wall construction of about 1650 m^2 is foreseen (building SH). It contains the screw compressors with their oil removal systems (oil separator, coalescers and charcoal adsorber), as well as the electrical sub-stations, the instrumentation air production and some free space for unloading, spare parts storage and work place. The maximum helium inventory is estimated to be 3.6 t. This includes the helium in the cavities, distribution piping and refrigerator. We have considered a scaling factor based on the inventory per metre of ILC. An additional safety factor of 1.5 has been considered to include a higher volume of superconducting cavities and safety margins (no final design of piping and cryostats). To store this inventory, four horizontal medium-pressure (20 bar) storage vessels of 250 m^3 will be required.

Assuming a 6% maximum cryo duty cycle and a power factor of 250 W/W at 4.5 K the electrical input power is about 4 MW, or 4.75 MW when taking into account the electrical efficiency of the compressors. For the design of the cooling water capacity required, a value equal to the nominal power consumption is considered, i.e., 4 MW. This covers the needs for the compressors and the cold boxes. The ventilation required for the compressor building would be about 4% of the nominal power consumption, i.e., 160 kW. A typical 250 Nm^3/h compressed-air unit would suit the instrumentation needs.

4.7.4 Open questions

The main issues are related to heat-load estimations and cryo-module design. The different assumptions considered for the heat-load estimations need to be reviewed in detail. A dedicated study, if possible with experimental data, is needed to better define the different heat loads, especially dynamic effects for RF equipment at 2 K and dynamic heat loads at the 5–8 K and 50–75 K temperature levels. This will have a direct impact on the cryogenic design since the assumption of taking the ILC model may have to be completely reviewed. The distribution cooling scheme should also be reviewed. Considering the size of the cavities, greater than the ILC ones, and the short length of the superconducting section, the possibility of having a simplified cryo-module design with a separated distribution cryogenic line should also be studied. Moreover, the compact design based on three cryo-strings should be reviewed to improve flexibility in case of failure or to accommodate additional components. Sizing of the different cryogenic lines should then be reviewed in order to cope with the final heat loads, required power to be extracted from the cavities, tunnel slope, pressure drops, etc. Additional components such as superconducting quadrupoles and current leads should be considered for the cryogenic design.

Cool-down, warm-up and other transient regimes should also be considered in order to identify possible process constraints. Safety issues like accidental discharge in the tunnel must be addressed as well.

4.8 Vacuum

The vacuum system of the linac facility, which has an overall length close to 700 m, can be divided into three parts with different vacuum requirements and space constraints: the warm section including the source (85 m), the cold section composed of all the superconducting cavities (340 m), and the cooled transfer line (306 m). Owing to the short time that the protons spend in the accelerator, the pressure requirements given by the lifetime considerations are not stringent. On the contrary, the presence of superconducting cavities necessitates producing a clean and dust-free vacuum having all the characteristics of the ultra-high vacuum.

The first section of the SPL machine, which contains the source of protons plus the pre-accelerating RF cavities, will have complex vacuum vessels and probably little space available for pumps. In order to avoid the ‘pollution’ of the superconducting cavities, part of this section will probably be baked to decrease the out-gassing and will be mounted under clean conditions to avoid dust contamination of the vacuum vessels.

The vacuum system of the superconducting-cavity section must ensure the clean and dust-free pumping of the delicate superconducting cavities. It could be a copy of the LEP straight sections as the cavities were operated there. The vacuum system is designed to minimize detrimental gas condensation inside the helium-cooled cavities. The procedures to operate it are defined to avoid the propagation of dust particles during the roughing or the venting of these cavities. They also use ultra-high vacuum standards in order to avoid any contamination of the cavity surface.

The warm vacuum system is a bakeable stainless-steel system with a 100 mm aperture (DN100) using mainly items recovered from LEP. Powerful pumping stations (400 l/s ion pump and titanium sublimation pumps) allow the molecules out-gassed in the adjacent warm parts of the vacuum system to be trapped and their condensation inside the cold modules to be avoided. Inverted magnetron gauges are used in the vicinity of the cold parts to avoid excessive heat loads to the cold system. All metal roughing valves allow the roughing stations to be connected to the vacuum system. Each module is isolated by all-metal gate valves to avoid any contact with the dusty environment of the accelerator tunnel during their installation and transport.

The vacuum system of the transfer line will be rather simple, but the pressure should be low enough to avoid the contamination of the cold cavities upstream. It is therefore recommended to extend the use of UHV standards and to bake out the linac extremity of this transfer line. If possible, the installation of a window should be foreseen.

The vacuum requirements of the linac facility are given in Table 4.28.

Table 4.28: Vacuum requirements for the different linac sections (mbar)

(Ion source) and LEBT	10^{-5}
RFQ	10^{-7}
MEBT (chopper line)	10^{-7}
DTL, CCDTL, SCL	10^{-7}
Superconducting linac	10^{-9}
Transfer line	10^{-8}

Chapter 5

Layout on site

5.1 Radiation protection and shielding

In this preliminary shielding design, a simple model was employed to estimate the lateral shielding required for the SPL, as well as to assess the radiation streaming through the waveguide ducts which will link the accelerator tunnel to the klystron gallery. Complementary Monte Carlo simulations were performed to confirm the shielding estimates [111]. Two situations were considered, namely normal operation and accidental beam loss. Beam losses for normal operation were assumed to be 1 W/m, a generally accepted figure which should keep the induced radioactivity in the machine to a level sufficiently low to permit hands-on maintenance (see, for example, Ref. [112]). An accident scenario considers a full loss of a 4 MW beam at a single point.

If the surface above the linac is not included in the CERN site, it will be a non-designated area according to the CERN Radiation Safety Manual [113], so that the dose must be kept below the limit of public exposure. Outside the fenced areas of the Organization, the dose at any point must not exceed 1.5 mSv per year and the dose actually received by a person must not exceed 0.3 mSv per year. The latter figure includes both external exposure due to stray radiation and internal exposure due to radioactive releases from CERN. In the present study, a constraint of 0.1 μSv/h was taken for the non-designated-area scenario. If the piece of land under which the linac will be installed is acquired by CERN, the dose limit can be higher. We refer here to the area classification as will be given in the new edition of the CERN Radiation Safety Code to enter into force within the next few months. Areas will be classified either as supervised radiation areas or as controlled radiation areas according to whether, under normal working conditions, persons could receive an effective dose exceeding 1 mSv or 6 mSv, respectively, in any consecutive 12-month period (but always staying below the legal annual limit of 20 mSv). Persons will be classified as category A or category B workers depending on whether or not they may be exposed to an effective dose exceeding 6 mSv in a 12-month period. The maximum average dose rates allowed in supervised and controlled areas are thus 3 μSv/h and 10 μSv/h, respectively, to account for the worst-case scenario in which a worker spends 2000 hours per year in the given area. A shielding design is proposed here for each of the three scenarios[1]. The service tunnel housing the klystrons (klystron gallery) is also underground, but as its access is restricted to CERN personnel it will be classified as either a supervised or a controlled radiation area.

In addition to the above requirements, in case of a full beam loss the accelerator control system must be capable of aborting the beam in a time short enough for the integral dose caused by such an accidental condition to remain negligible.

For the normal operation, the shielding calculations were performed at a few selected energies between 25 MeV and 3.5 GeV. The most stringent shielding requirements are imposed at the high-energy end of the accelerator because of the more penetrating component of the secondary neutrons. Below 1 GeV a simple point-source/line-of-sight model was adopted. This model requires the knowledge of the source term (i.e., the number and energy distribution of the neutrons generated by the interaction of the proton beam with accelerator components or a target) and of the attenuation length (which accounts for the shielding properties of the material). At energies above a few GeV the Moyer model was employed, for which there also exists a formulation for a line source [114]. The line-source model was applied above 1 GeV and the results compared with those of calculations made for a point source. Such a comparison has shown that the two calculations give similar results if one assumes a beam loss over a distance of

[1] Given the safety margin included in the present shielding design and considering that the real occupation time of areas with the presence of radiation is well below 2000 hours per year (which is used in the calculations), the above dose-rate constraints are positively conservative.

about 7 m concentrated at a single point. To be on the safe side, in the present assessment calculations for all energies (from 25 MeV to 3.5 GeV) were made assuming 10 W point losses every 10 m. This assumption was recently validated with FLUKA simulations and adopted for the shielding design of Linac4 [115, 116].

Table 5.1 gives the thicknesses of the concrete shield as a function of proton energy that are required to meet the design dose rates of 0.1 μSv/h for a non-designated area, 3 μSv/h for a supervised radiation area, and 10 μSv/h for a controlled radiation area. Source terms and attenuation lengths used for the calculations are taken from Ref. [117] (for copper rather than niobium, but this is a minor source of error) for the energy interval 25–800 MeV and from the Moyer model for 1 GeV and above.

Table 5.1: Minimum shielding thickness required to reduce the dose rate to below 0.1 μSv/h (limit for public exposure), 3 μSv/h (supervised radiation area), and 10 μSv/h (controlled radiation area)

Beam energy	**Intensity (protons per**	**Required shielding (metres of concrete)**		
[MeV]	**second) per 10 W loss**	**Public**	**Supervised**	**Controlled**
25	2.5×10^{12}	1.6	1.2	1.1
50	1.3×10^{12}	1.8	1.4	1.2
100	6.2×10^{11}	2.7	2.0	1.8
200	3.1×10^{11}	4.1	3.1	2.8
300	2.1×10^{11}	4.8	3.6	3.2
400	1.6×10^{11}	5.2	4.0	3.5
600	1.0×10^{11}	5.7	4.3	3.8
800	7.8×10^{10}	6.1	4.6	4.0
1000	6.2×10^{10}	6.5	4.9	4.3
2000	3.1×10^{10}	6.6	5.0	4.4
3500	1.8×10^{10}	6.6	5.0	4.4

A simplified model of the SPL was implemented with the FLUKA Monte Carlo code in order to validate the analytical calculations [111]. Four beam energies were investigated: 300 MeV, 600 MeV, 1 GeV, and 3.5 GeV. The supervised radiation area scenario was chosen as the representative scenario amongst the three discussed above. A total of nine cavities were modelled in FLUKA as 0.5-m-long hollow cylinders with 30 mm inner radius and 70 mm outer radius. The cavities are surrounded by a hollow 5-mm-thick steel cylinder, 0.5 m in radius, representing the cryostat. The distance between two adjacent cavities is 0.5 m. A 30 mm radius beam-pipe made of steel connects each cavity to the next one. The nine cavities are distributed along the axis of a concrete cylinder, 10 m long and 2 m in radius, which represents the tunnel. The concrete shielding was assigned the minimum thickness required to meet the 3 μSv/h constraint.

Figure 5.1 shows the ambient dose equivalent $H^*(10)$ around the niobium cavities during operation. The total power lost inside the tunnel is the same for all scenarios (i.e., 10 W), but the dose rate distribution obviously depends on the beam energy. The maximum ambient dose equivalent rates scored with FLUKA are given in Table 5.2. The shielding thickness calculated with the analytical method is in overall good agreement with the FLUKA results and tends to be rather conservative, except at 600 MeV where the analytical method slightly underestimates the dose past the shield.

A beam-loss monitoring system, interlocked with the accelerator control, will be needed to ensure that during operation losses stay below the specified value of 1 W/m.

A shielding designed for a continuous beam loss of 1 W/m (or 10 W point loss) during routine operation is also adequate for an accidental loss of the full beam at a localized point, provided that the control system can intervene and stop the beam within a pre-defined time. If the linac is stopped within 10 ms, the integral dose delivered to a public, supervised, or controlled area in this time interval is of the order of 0.1 μSv, 1 μSv, and 10 μSv, respectively.

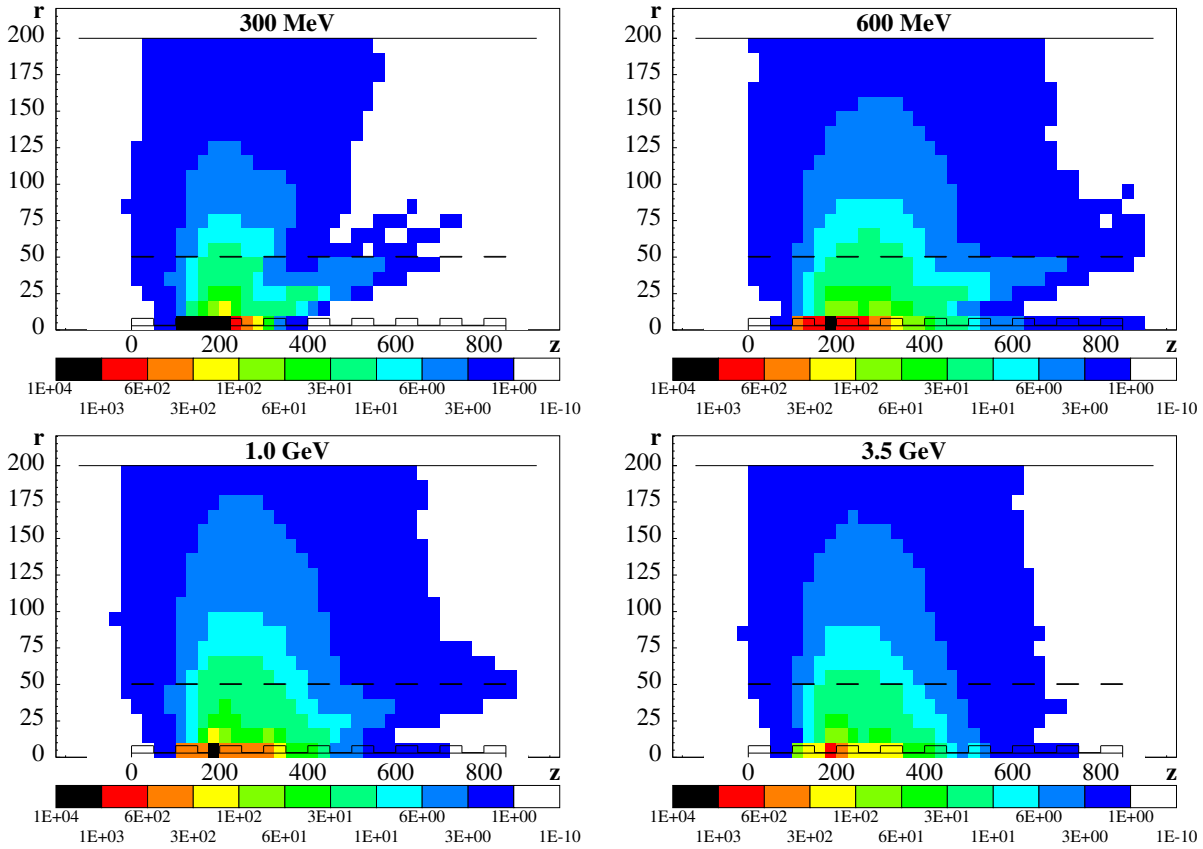

Fig. 5.1: Side cross-sectional view of the tunnel (cylindrical geometry) with the radiation levels (ambient dose equivalent rate in Sv/h) for losses at 300 MeV, 600 MeV, 1 GeV, and 3.5 GeV. The z-r scales are in centimetres, with z representing the tunnel axis. The beam propagates from left to right on $r = 0$. The RF cavities are centred along $r = 0$, the dashed line at $r = 50$ cm represents the cryostat. The colour scale is in Sv/h; the white area represents dose equivalent rates < 1 Sv/h.

Table 5.2: Maximum ambient dose equivalent rate past the shield as a function of beam energy (FLUKA simulations) for a beam loss of 10 W. The shielding thicknesses are those giving 3 μSv/h with the simple point-source/line-of-sight model.

Energy [MeV]	300	600	1000	3500
Shielding [m]	3.3	3.8	4.4	4.4
Distance from beam axis [m]	6	8	10	10
$H^*(10)$ [μSv/h]	2.3	3.2	1.1	1.8

In the present design several ducts connect the linac and klystron tunnels, housing the waveguides linking the klystrons to the RF cavities. At the exit of multi-leg straight ducts, the dose equivalent is dominated by the contribution from low- and intermediate-energy neutrons. The transmission of neutrons around right-angled bends can be estimated by means of universal transmission curves [117]. These curves provide the attenuation factor after the first and the subsequent legs as a function of the distance from the tunnel mouth and the duct cross-section.

The waveguides of the SPL may be divided into three sections. In the first section protons are accelerated up to 90 MeV. There are 14 waveguides distributed along 49 m with $60 \times 16\,\mathrm{cm}^2$ cross-section. The second section, where protons reach 180 MeV, is 36 m long and includes six ducts ($29.2 \times 14.6\,\mathrm{cm}^2$). The superconducting section (above 180 MeV) is 342 m in length and includes 69 ducts (29.2

$\times$ 14.6 cm^2). The klystron gallery is 12 m wide in the warm section (0–180 MeV) and 4 m wide in the superconducting section (>180 MeV). The horizontal distance between the mouths at the two ends of the ducts will consequently be 3.5 m in the warm section and 9 m in the superconducting section. The vertical distance will be 5 m in both cases.

The case of two-leg waveguides was studied first, because of their technical and economic advantage with respect to multi-leg guides. Point losses of 10 W (off the duct axis) were assumed in the SPL tunnel. Table 5.3 provides the dose rate expected at the mouth of the ducts in the klystron gallery (H_{klystron}) as a function of the beam energy.

Table 5.3: Attenuation properties of two-leg ducts connecting the SPL tunnel to the klystron gallery. For each energy the ambient dose equivalent rate $H^*(10)$ in the linac tunnel, the transmission factor of the two legs, and the $H^*(10)$ in the klystron gallery are given.

Energy [MeV]	25	50	100	200	300	400	800	1000	2000	3500
H_{linac} [Sv/h]	0.63	0.81	1.08	1.46	1.73	1.8	1.8	2.93	2.48	2.19
1$^{\mathrm{st}}$ leg transm.	$< 10^{-3}$	$< 10^{-3}$	$< 10^{-3}$	$< 10^{-3}$	$< 10^{-3}$	$< 10^{-3}$	$< 10^{-3}$	$< 10^{-3}$	$< 10^{-3}$	$< 10^{-3}$
2$^{\mathrm{nd}}$ leg transm.	$< 10^{-4}$	$< 10^{-4}$	$< 10^{-4}$	$< 10^{-4}$	$< 10^{-4}$	$< 10^{-4}$	$< 10^{-4}$	$< 10^{-4}$	$< 10^{-4}$	$< 10^{-4}$
H_{klystr} [μSv/h]	< 0.1	< 0.1	< 0.1	< 0.2	< 0.2	< 0.2	< 0.2	< 0.3	< 0.3	< 0.3

The attenuation factors given in Ref. [117] are a function of the normalized distance $d_{\mathrm{n}} = d/\sqrt{A}$, where d is the leg length and A is the cross-sectional area of the duct. The attenuation factors decrease with increasing d_{n}. However, in Ref. [117] these factors are only given for $d_{\mathrm{n}} < 10$, whilst in our case $11 < d_{\mathrm{n}} < 44$. To be on the safe side, the attenuation factor corresponding to $d_{\mathrm{n}} = 10$ was taken for all legs. Even under this conservative assumption, the two-leg ducts as described above comply very well with the constraints of a supervised radiation area ($< 3\,\mu$Sv/h). In the room-temperature section of the SPL, the contribution of the radiation streaming through the ducts is negligible with respect to the radiation transmitted through the 2.6 m thick layer of rock between the linac tunnel and the klystron gallery.

A preliminary investigation of the induced radioactivity in the linac was also performed using FLUKA [111]. For a six-month irradiation with a beam loss of 1 W/m, values range from a maximum of about 5×10^8 Bq (for one-hour waiting time) down to a minimum of 2×10^5 Bq (for one-year wait). The average specific activity ranges from about 10^4 Bq/g to 200 Bq/g for one-hour waiting time, and in the range 2×10^3 Bq/g to a few Bq/g for a cooling time of one year. The induced radioactivity is obviously not uniformly distributed, with the material close to the loss point more active, and scales with the deposited power.

As the project advances, the present preliminary shielding and duct design will have to be confirmed by detailed Monte Carlo simulations. The design of the beam dumps will need careful attention. The shielding of the transfer line will have to be designed. Further issues which will have to be considered are groundwater activation, as well as radioactive air and liquid releases. An aspect which will have to be carefully addressed is the induced radioactivity in the linac and surrounding structures (shielding, support structures, cables and cable-trays, etc.), this also in view of assessing the amount of radioactive waste to be handled at the time of the facility's decommissioning.

5.2 Civil engineering

The main guidelines for the design of the civil-engineering parts of the linac were, as far as possible,

- to minimize the civil-engineering costs (construction costs and re-use of existing tunnels and infrastructure);
- to respect the tunnel depth and shielding specified by radiation protection;
- to provide an easy connection with the ISR tunnel, the PS (clockwise injection), and with the ISOLDE area; and
- to minimize the environmental impact.

For CDR1 five alternative positions of the linac were compared. After an analysis of their advantages and disadvantages and a brief cost estimation, the site parallel to Route Gregory, immediately outside of the existing CERN fence, was chosen. The linac tunnel and a parallel klystron gallery followed this road for 800 m on Swiss territory. For this solution, the connections with the ISR, the PS and ISOLDE could re-use a maximum of existing tunnels, and a cut-and-cover excavation technique could minimize the construction costs. The final environmental impact was minimum (most of the site is at present an empty grass field) and a maximum of existing buildings on the Meyrin site could be re-used. Access to the site was easy from the existing Route Gregory.

Following the design changes of the SPL, a new version of the civil-engineering layout is now being considered (Fig. 5.2). The overall length of the linac tunnel is now 470 m, cross-sectional dimensions being 4 m in width by 4.80 m in height. At the end of the linac, there is a 20-m-long dump tunnel.

In order to take into account the shielding requirements imposed by radiation-protection considerations and the location of the ISR, the level of the top section of the tunnel is about 17 m below ground level and its slope is 1.3% (Fig. 5.3). The underground structures are made of reinforced concrete with a thickness of the order of 0.4 m for walls, 0.6–0.7 m for floors and covering slabs, to be determined more precisely at a later stage of the design. Figure 5.4 shows a transverse cut of the tunnel. Tunnel works are carried out partially using the cut-and-cover method (earthworks, diaphragm wall or sheet piling) and partially by road-header, optimizing the depth with reference to predicted costs and environmental impact. One access shaft is located at the start of the linac tunnel for transfer of the equipment. Figure 5.5 shows a cross-section with the access shaft.

Rather than considering klystron buildings above ground, a tunnel alternative has been chosen in order to reduce the environmental impact. The klystron tunnel is 470 m long, with cross-sectional dimensions of 12 m in width by 4 m in height in the first 95 m, and of 4 m in width by 4 m in height in the following 375 m. The depth of the underside of the cover slab is about 1 m below ground level at the start and the end of the tunnel. Its slope is approximately 2.25%. The tunnel works are carried out using the cut-and-cover method. Figure 5.6 shows a cross-section of the first 95 m.

The location of the accumulator and compressor ring is likely to change in future revisions of the SPL layout. For lack of well studied alternatives, however, we assume as in CDR1 that such a ring will be installed in the tunnel of the old Intersecting Storage Rings (ISR) which is in principle available for this purpose. Therefore the CDR1 layout has been adopted even though it is already clear that the transfer line radius will have to be increased from the present 100 m to $\approx$ 220 m. The length of the present transfer tunnel connecting the linac with the ISR is about 150 m and is likely to increase once the radius is increased to $\approx$ 220 m. The cross-sectional dimensions are the same as those of the linac tunnel. It will have a slope of about 1.65%, governed by the present location of the ISR. In this case, tunnel works are carried out using excavation by road-header, since this tunnel is too short to use a tunnel-boring machine. The level of the top section of the tunnel is about 14 m underground, and 6 m into the molasse. The transfer tunnel is connected to both the ISR and the TT1 tunnel via a new cavern. The TT1 tunnel, and further on the TT6 tunnel, connects the linac with the PS ring (clockwise). No civil-engineering works are necessary for this connection.

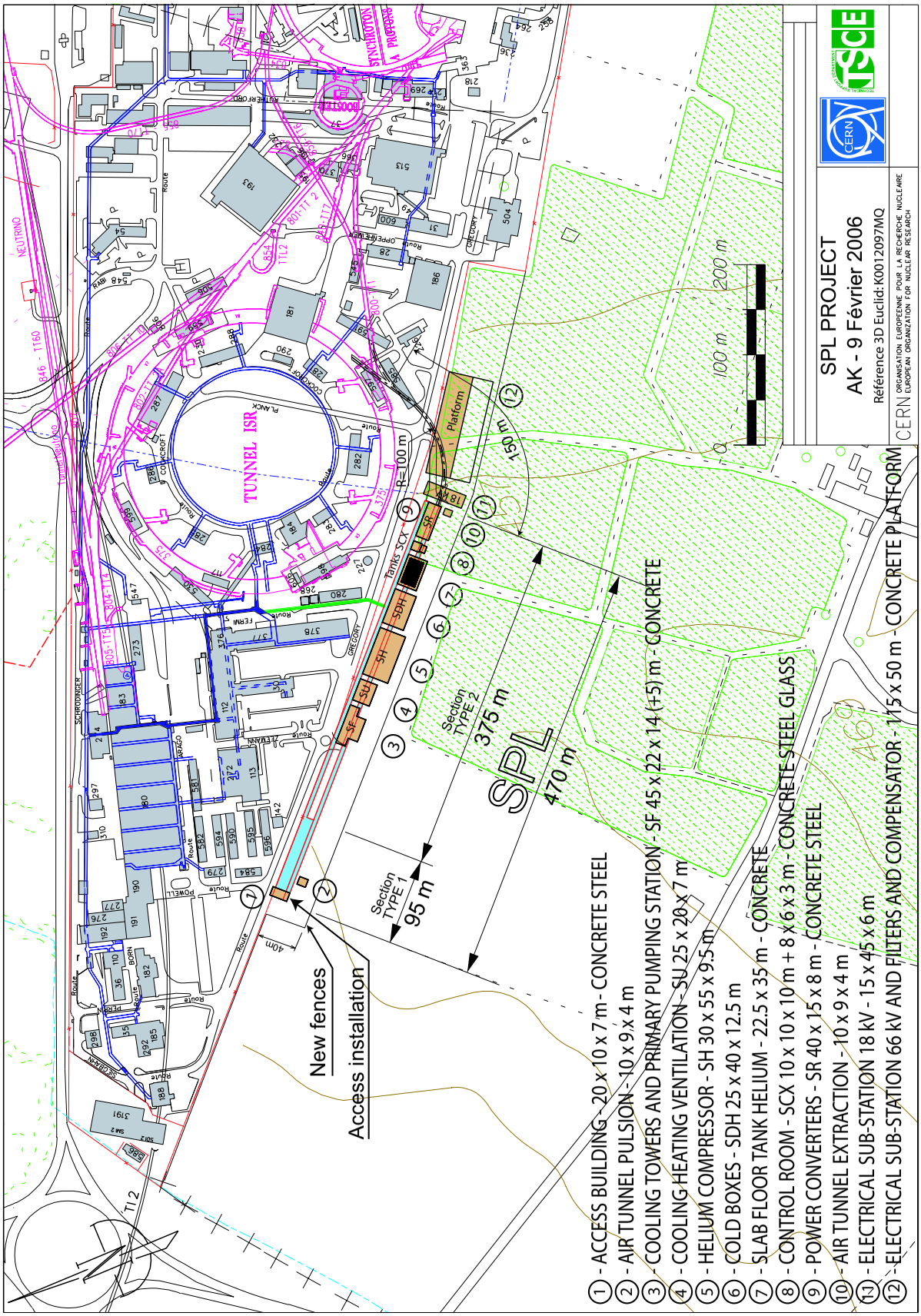

Fig. 5.2: Proposed layout of the linac facilities on the CERN Meyrin site

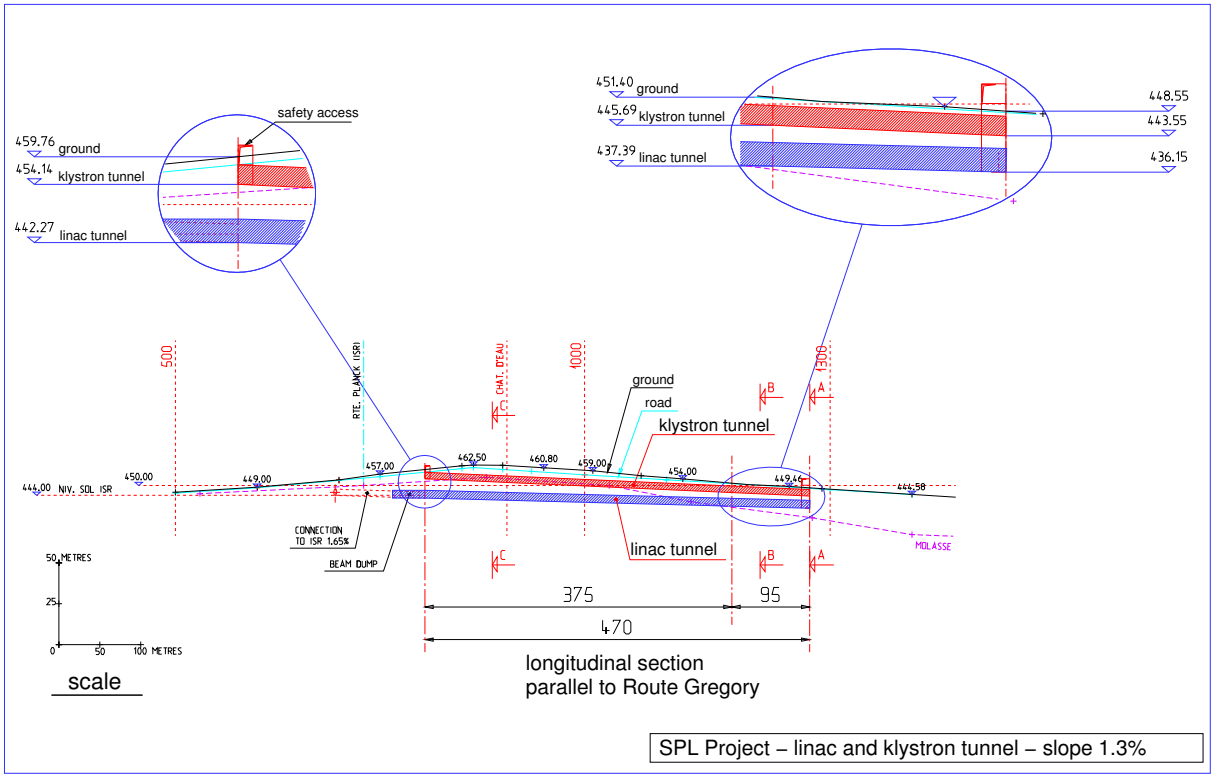

Fig. 5.3: Side view of the linac tunnel

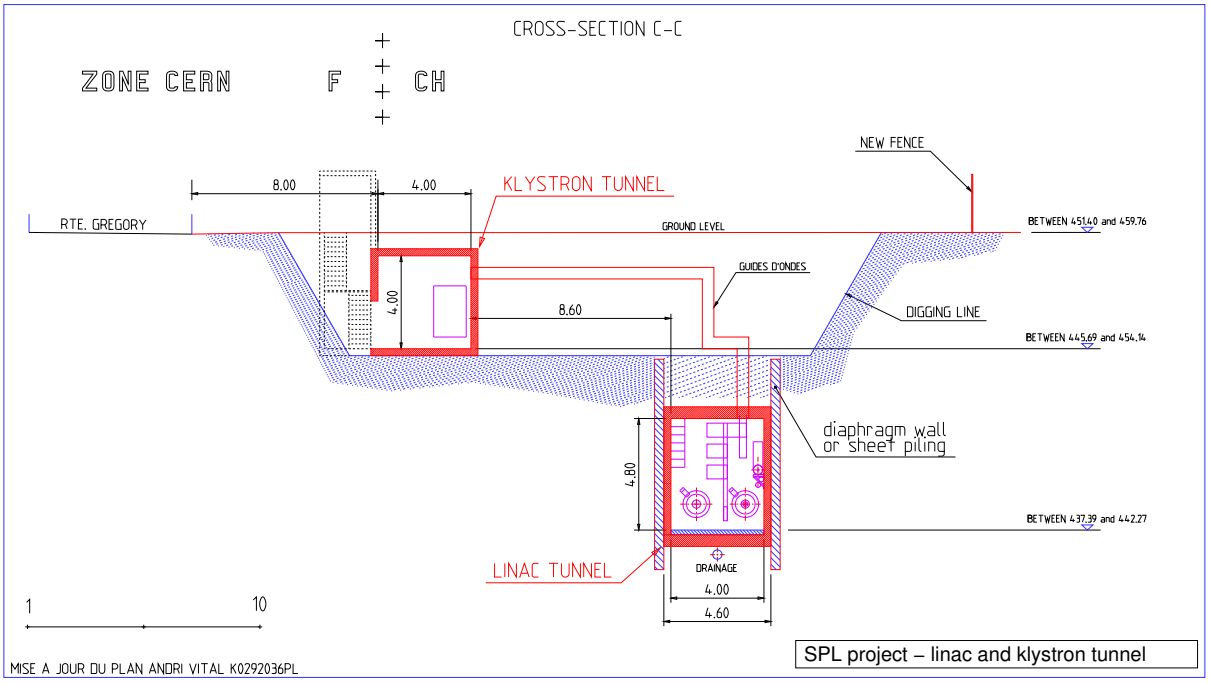

Fig. 5.4: Cross-section of the linac and klystron tunnels for the superconducting section

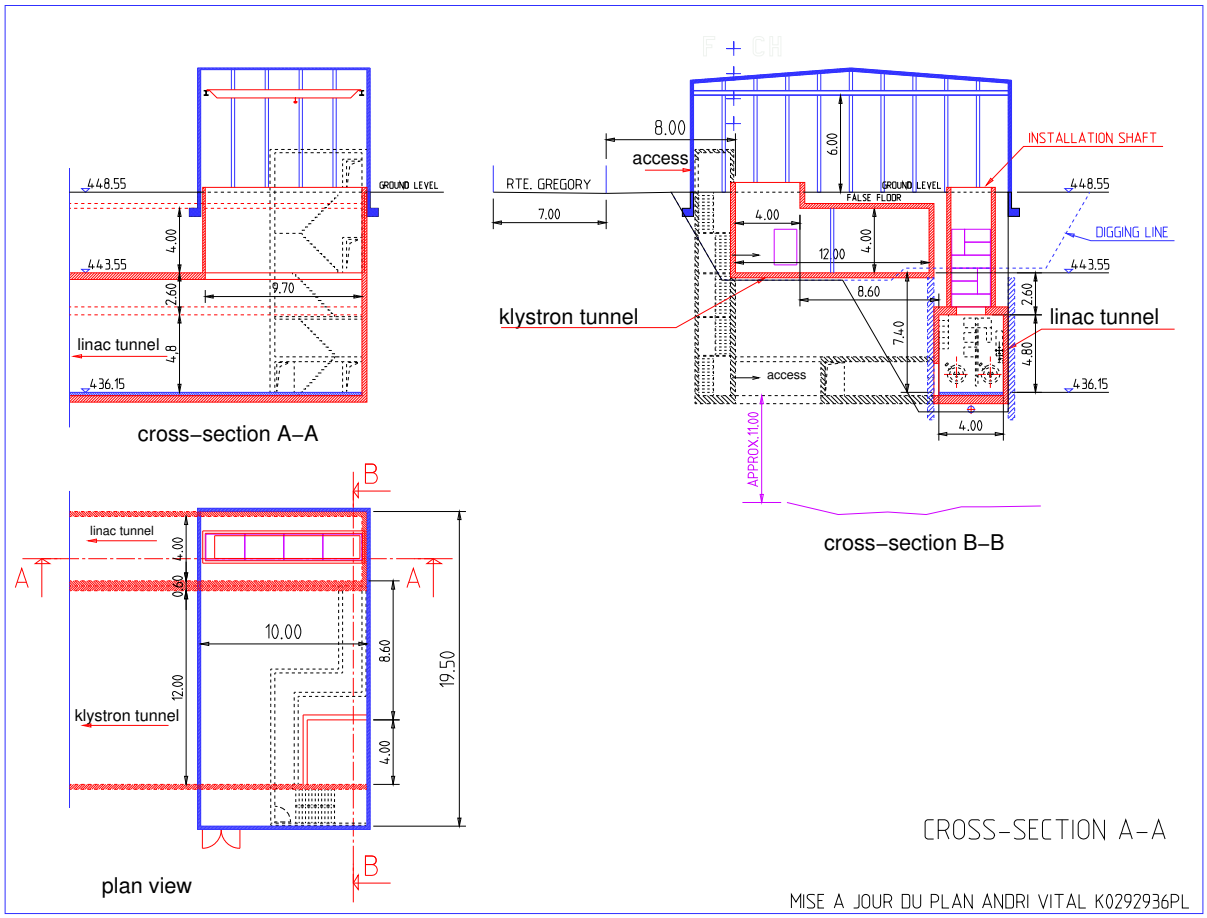

Fig. 5.5: Cross-section with access and access shaft

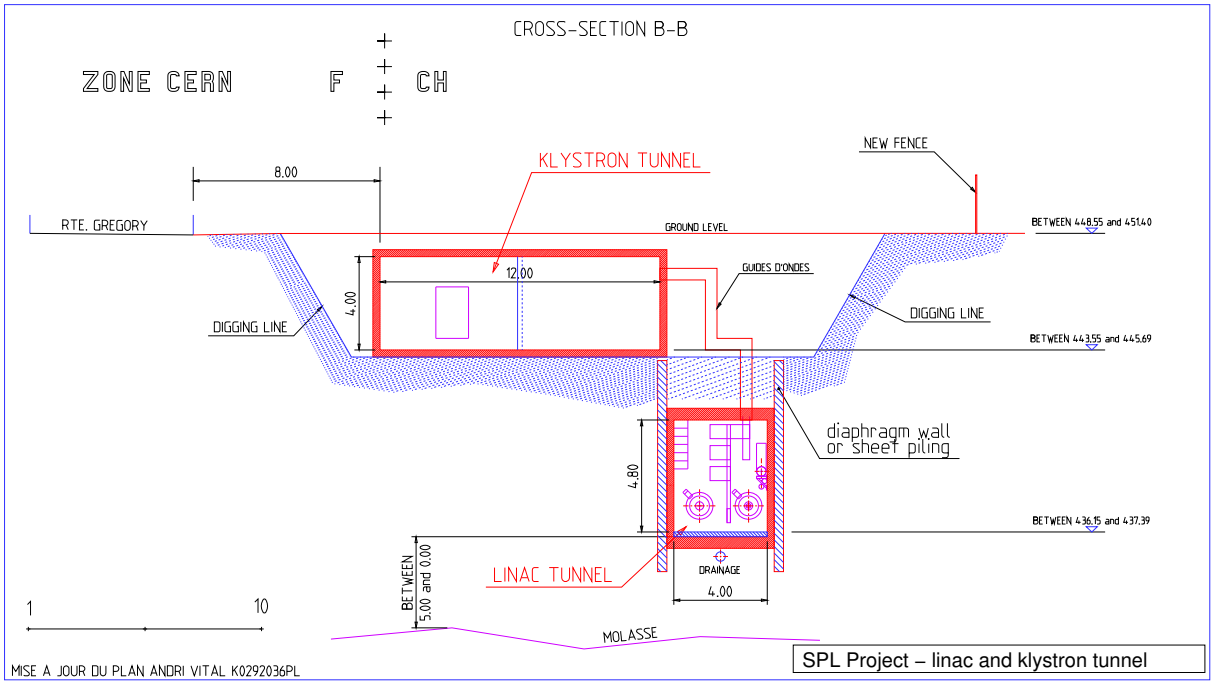

Fig. 5.6: Cross-section of the linac and klystron tunnels (first 95 m)

A connection with ISOLDE (Fig. 5.7) can be made via the TT6 tunnel, requiring a new tunnel section of about 40 m length which includes a dump of 10 m length. The tunnel floor level is horizontal, to avoid the risk of irradiation to Route Democrite, and crosses the existing TT70 tunnel which is no longer in use. In this preliminary design, a vertical shaft links the transfer tunnel with the ISOLDE area. The exact position and angle of the beam entering the area will be defined according to ISOLDE's future plans. Tunnel works are again carried out using excavation by road-header.

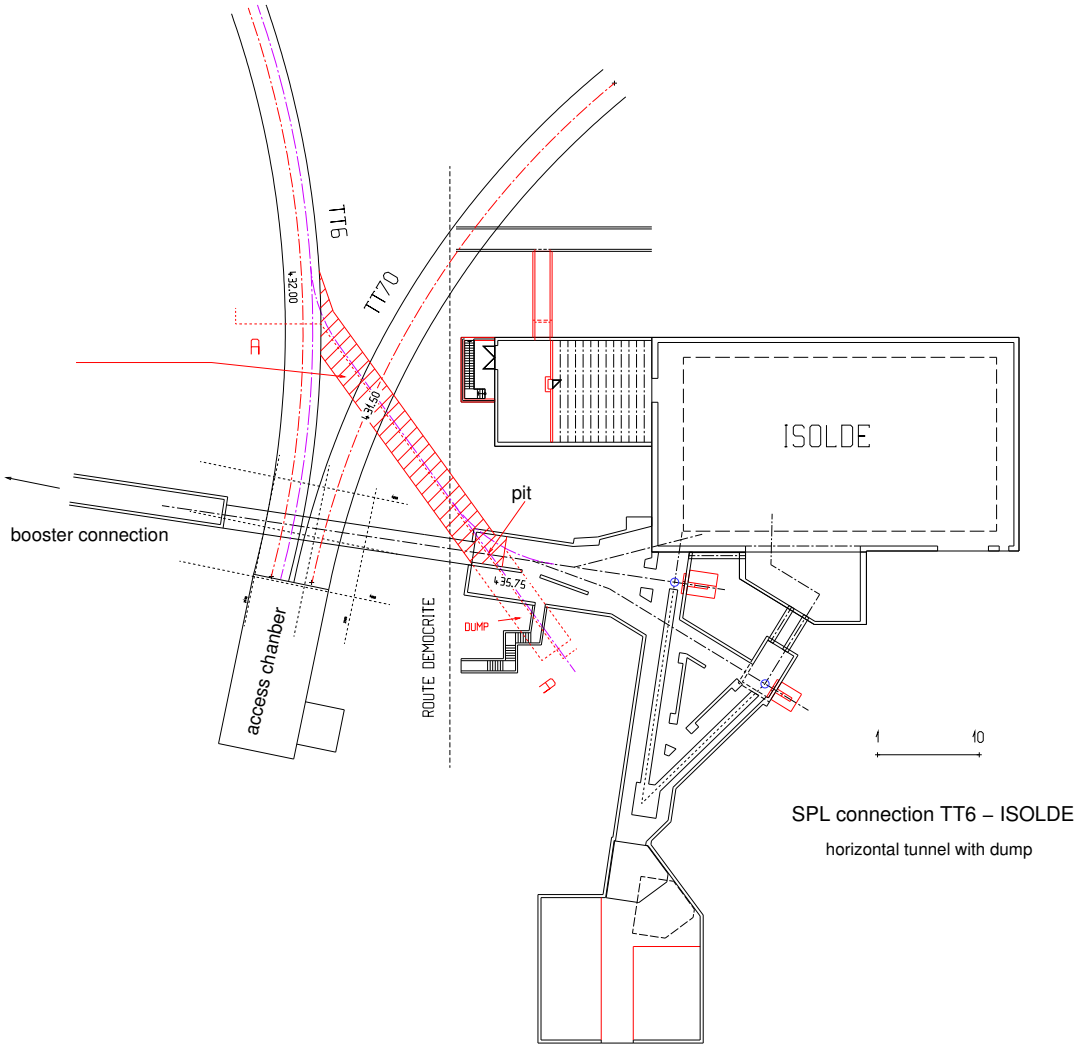

Fig. 5.7: Connection of the transfer tunnel to ISOLDE, plan view

For the services related to the machine, the new surface buildings and related ancillary structures that are directly linked to the running of the machine are described in Table 5.4. For a preliminary analysis of the layout, all the new buildings have been placed on the new land to be acquired by CERN across Route Gregory (Fig. 5.2).

No additional road networks need to be created. The existing roads provide access to all surface buildings, to the shafts and the underground machine facilities (Route Gregory). However, some adaptation of the existing roads is likely to be required. Car parks and areas for handling equipment are foreseen around the buildings and the shafts. A new plot of land has to be integrated in the CERN Meyrin site, through negotiations with the relevant Swiss authorities. A positive preliminary answer has been given to CERN's Local Affairs section. Nevertheless, particular care will have to be given to the final landscaping of this area, with the intervention of a landscape designer.

Table 5.4: Surface buildings

Purpose	Name	Dimensions†	Material	Particularity
Control room	SCX	18×10×10	Concrete, steel, glass	False floor under racks
Power converters	SR	40×15×8	Concrete, steel	False floor under racks Overhead crane (10 t)
Helium compressor	SH	55×30×9.5	Concrete	Overhead crane (20 t)
Cold boxes	SDH	40×25×12.5	Concrete, steel	Overhead crane (5 t)
Slab floor for helium tank		22.5×35	Concrete	–
Cooling, heating, ventilation	SU	25×20×7	Concrete	False floor (2 m) Overhead crane (5 t)
Electrical sub-station (18 kV)		15×45×6	Concrete	False floor (2 m) Overhead crane (5 t)
Electrical sub-station (66 kV), filters and compensators		115×50	Concrete platform	False floor (2 m) Overhead crane (5 t)
Air tunnel		10×9×4	Concrete	–
Air tunnel extraction		10×9×4	Concrete	–
Cooling towers and primary pumping station	SF	45×22×14	Concrete	–

† Dimensions are specified as: length [m] × width [m] or length [m] × width [m] × height [m]

5.3 Cooling and ventilation

5.3.1 Primary cooling plant

The cooling is achieved by means of cooling towers which dump into the atmosphere all the power dissipated as heat, by both machine elements and their facilities. The primary cooling circuit collects cold water from the basin of the cooling towers and delivers it to the different users, who can either use the primary water to directly cool their equipment (as in the case of cryo-compressors) or, if required by the process, to cool down the secondary circuits. Cooling towers and primary pumping station equipment will be housed in the same building (SF), much in the fashion of the cooling towers built for the new experimental areas of the LHC at points 1 and 5. This building should be erected in concrete (on account of the noise made by the machinery) and close to the other cooling equipment buildings to minimize the cost of the necessary distribution piping. Two cells, of a specific capacity of $\approx$ 20 MW (allowing a spare cell for maintenance or breakdowns) will be necessary.

The cooling temperature of the cooling towers is conditioned by the thermodynamic characteristics of the outside air, the final cold source. The cooling-tower water will reach temperatures of about 24 °C during the summer months in the Geneva region, which in turn entails temperatures of the order of 26 °C for the secondary circuits.

The primary water will be routed to the cooling technical building (SU) housing the secondary cooling plant (heat exchangers and demineralized water distribution pumps) and the chilled (or mixed) water production plant. Chilled water, at 6 °C, is used for air conditioning (or when required by the process for specific cooling) purposes. Table 5.5 summarizes the primary cooling needs and the parameters defining the primary circuit.

5.3.2 Secondary cooling plant

The secondary cooling circuits are used when the process to be cooled requires a cooling medium other than raw (drinking quality) water. This is usually the case for magnets and RF amplifiers where dem-

Table 5.5: Primary cooling needs and cooling-circuit parameters

	ΔT [K]	**Power** [MW]	ΔP [bar]	**Flow rate** [m^3/h]
Primary cooling SPL	9	16.8	5	1600
Cryo-compressors	5.7	4.0	5	600

ineralized water is necessary. The klystrons may be a particular case in that they sometimes require a somewhat lower resistivity of the secondary cooling circuit water, usually achieved by 'doping' the demineralized-water circuit. The secondary circuits extract the heat dissipated by the warm sources and convey this heat to the primary source via heat exchangers.

In order to minimize the cost and complexity of the cooling facilities, 'lumped' cooling circuits are used which are shared amongst machine components requiring similar cooling characteristics. The schematic diagram of the main cooling plant (housed in building SU) is shown in Fig. 5.8. The production of compressed air (300 Nm^3/h) for instrumentation (cryogenics) will also be housed in the SU building.

It is customary to house as much of the equipment as possible in the cooling technical building, in order to simplify the associated operation and maintenance costs. However, as can be seen in Fig. 5.8, some minor circuits will be located outside the SU building. This is the case for the beam dump, which will sit in the non-accessible machine tunnels on account of the induced radioactivity.

The SU building would have approximately 25 m × 20 m plan dimensions and a height of 5 m, with a false floor of 2 m. Tables 5.6 and 5.7 summarize the secondary and tertiary cooling circuits required.

When the integration studies of the equipment are carried out, particular attention must be paid to the space required by the water distribution lines (demineralized and chilled water, compressed air) in the tunnels, in view of their size.

Table 5.6: Secondary cooling circuits

Item	**Fluid**	**Power** [kW]	P_{max} [bar]	ΔT [K]	**Flow rate** [m^3/h]
Klystron	Demineralized water	11000	8.5	7.5	1300
RF loads	Demineralized water	4500	8.5	20	200
RT cavities	Demineralized water	800	8.5	10	70
Magnets (quadrupole)	Demineralized water	100	12	15	6
Magnets (bending)	Demineralized water	300	12	15	17
Dump linac	Demineralized water	100	12	15	6

Table 5.7: Air-conditioning/chilled-water requirements

Building	**Air conditioning** [kW]	**Chilled-water flow rate** [m^3/h]
SH	250	36
SR	50	8
SCX	120	18
Tunnels	500	72

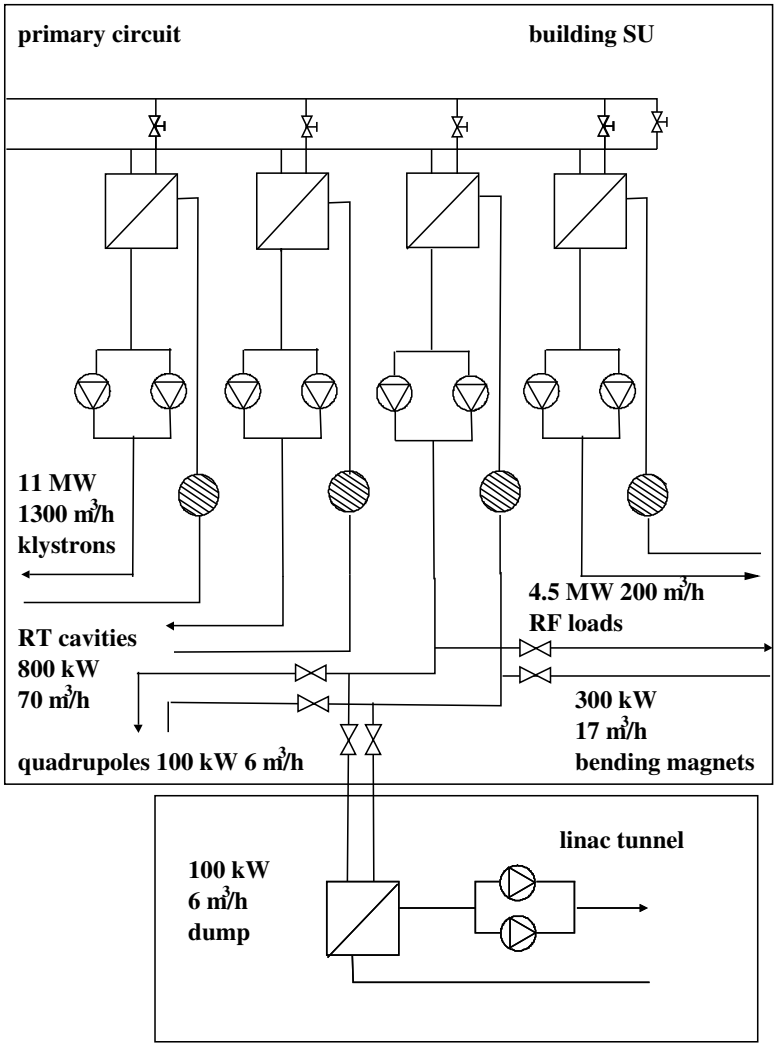

Fig. 5.8: Schematic diagram of the main cooling plant

5.3.3 Chilled-water plant

The chilled-water plant provides the cold fluid (6–12°C) necessary for the air conditioning of the different spaces and for the cooling of racks and electronics.

Three mid-range capacity screw compressors (500 kW each) should be installed to provide for all the SPL project needs. This allows for one group to be employed as 'hot' spare in case of maintenance or breakdowns. Chilled water will be distributed via dedicated circuits to the different users. For the same reasons mentioned above in the case of the SF–SU siting, the closer the end-users are to the SU building the more economical the insulated distribution piping will be. If necessary, for direct cooling of racks or electronics at temperatures above the dew point, a tertiary circuit could be made (via a heat exchanger and distribution pumps) using chilled water as secondary.

This schematic is for indicative purposes only; the final layout of the stations (pumps and circuits grouping) can only be determined when the detailed engineering is complete.

5.3.4 Air-conditioning (HVAC) plants

The different buildings requiring air conditioning will be built with a technical room for the installation of the HVAC plants, of sufficient surface to allow the installation of the equipment and the subsequent

maintenance; this is in addition to the buildings defined for the HVAC needs of the machine tunnels. The SCX building would require a technical room 8 m × 6 m (3 m high) next to an external wall of the building (for the fresh air intake). The SH unit, installed preferably inside the building proper, would require the same free surface. The SR unit would require a surface of 3 m × 3 m.

The operation parameters for the air conditioning in the SH building would be somewhat different from those linked to comfort applications, leaving the ambient temperature to reach higher temperatures (in the order of the 30–35°C) in order to reduce the HVAC equipment size and cost. Comfort or rack applications usually require more stringent temperature conditions (ambient temperature in the order of 25°C).

Smoke extraction installations, as required by law, will have to be studied at a later stage when details on the equipment layout and installation are known.

5.3.5 Power requirements

Table 5.8 summarizes the power requirements for the operation of the cooling and ventilation equipment.

Table 5.8: Power requirements for cooling and ventilation

Item	**Location**	**Power** (kW) $\cos\phi = 0.8$
Cooling towers	SF	600
Primary pumps	SF	500
Demin. and chilled water pumps	SU	700
Chilled water production	SU	600
HVAC tunnel	HVAC pulsion bldg.	900
HVAC SCX	SCX	120
HVAC SH	SH	400
HVAC SR	SR	50
Total		3870

5.4 Electrical infrastructure

An estimation of the electrical power requirements for the different components of the SPL facility is presented in Table 5.9. The final power requirements will depend on the performance of the normal-conducting and superconducting RF cavities and the pulse structure used for operation.

Table 5.9: Electrical power requirements (MW) of the SPL (r.m.s. values)

Load	**4 MW neutrino baseline**	**5 MW EURISOL baseline**
RF system[†]	20.2	24.4
Cryogenics	3.6	4.4
Cooling and ventilation	4	4
Other	1	1
General services (surface + tunnel), racks, computers, controls	3	3
Total	32	37

[†] Including 30% margin to compensate for Lorentz-force detuning in the SC cavities.

The current study is based on the power requirements for the SPL EURISOL baseline (right column). Owing to the high costs of the 4 km of 66 kV cable and power transformers, the link between

Prévessin and Meyrin already takes into consideration possible future upgrades of the SPL in order to avoid replacement of these very costly components.

So far, we assume that all major electrical loads (RF, cryogenics and CV) are stable, non-pulsating loads and that the RF pulsing is absorbed in the power supplies. However, because of the high contents of rectifier load, a Static Var Compensator (SVC) will most likely be required to obtain a satisfactory mains quality with respect to harmonic distortion and voltage stabilization. At the same time, the reactive power will be compensated such that MW and MVA are almost equal.

The overall electrical consumption will be around 40 MW. For comparison, the Meyrin electrical network with the PS and Booster in operation consumes about 25 MW during the full-load period in summer. The SPL EURISOL baseline will have almost twice the power consumption of the entire Meyrin network, and corresponds to about 30% of total LHC consumption. Owing to its large power demand, the SPL cannot be integrated into the existing electrical infrastructure of Meyrin; a new power in-feed from Prévessin and a large new 66/18 kV substation in Meyrin will be necessary (Fig. 5.9). Standard solutions developed for LEP/LHC will be applied to a large extent.

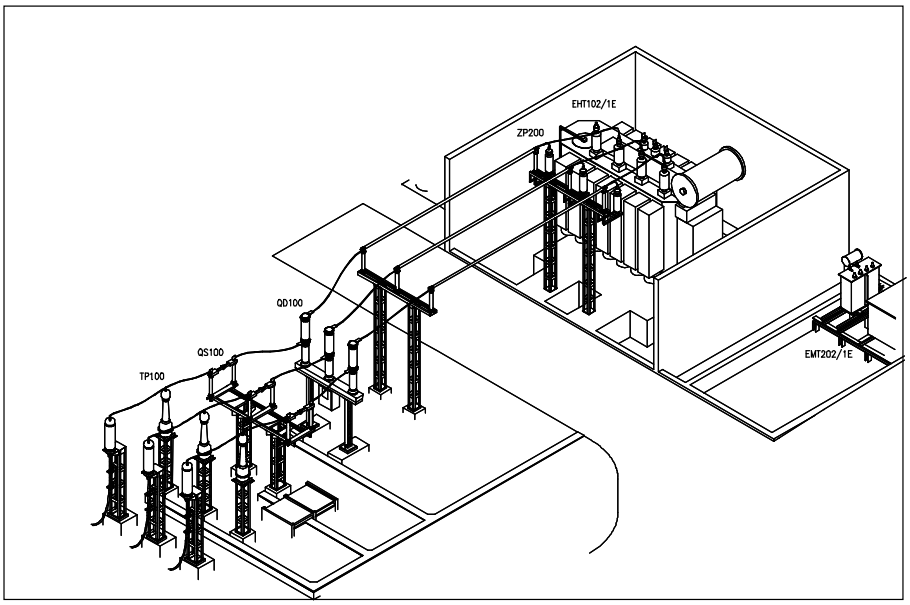

Fig. 5.9: Layout of CERN's standard 66/18 kV substation

The total power available from the Prévessin 66 kV system is 220 MVA: two transformers, each with 110 MVA. The total existing requirements will be around 180 MVA, including the LHC requirements estimated to be around 125–130 MVA. Adding the power requirements for the SPL to the existing 66 kV station would bring CERN's entire 66 kV system, including LHC, too close to 100% of its thermal limits or even overload the system. Any future upgrade of the SPL or any other additional high-power user could certainly not be covered with the existing 400 kV installation. Clearly, a new in-feed from 400 kV will be needed right from the beginning.

This will require a new 400 kV bay in CERN's major 400 kV substation, including a new 400/66 kV transformer in Prévessin. From the 66 kV side of the transformer there will be a 66 kV cable from Prévessin to Meyrin, terminating in Meyrin with a 66/18 kV transformer and a major 18 kV substation. Depending on the final power requirements of SPL upgrades or other users on the Meyrin site, the possibility of future extension with a second 66 kV cable and a second 66/18 kV transformer will be reserved. From the 18 kV substation, there will be 18 kV cables to the 18/0.4 kV individual distribution transformers and to the 18/3.3 kV transformers for cryogenics, as well as to large RF power converters being supplied directly from the 18 kV level (see Fig. 5.10).

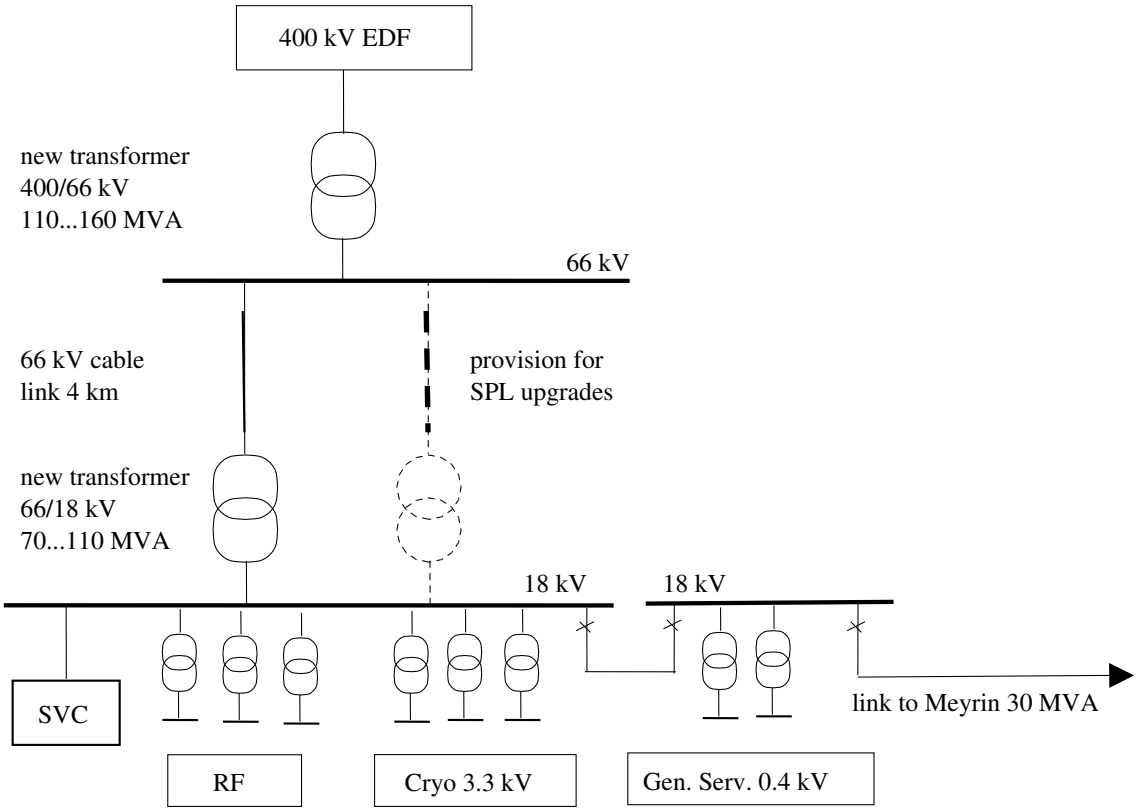

Fig. 5.10: Proposed electrical distribution system for the SPL

Based on previous experience with repeated cable trench digging between Meyrin and Prévessin, it is strongly proposed to install a cable duct or gallery between these two major CERN sites. Previous experience has shown that such a cable duct would be amortized within five to seven years, since additional cabling needs (including optical fibres) arise on average every three years. This would give the possibility of a second 66 kV link and of a new crucial 18 kV cable MP6 between Prévessin and Meyrin.

Depending on the final power requirements and their geographical distribution, there might be the need for an underground cavern for an electrical substation.

The new electrical system is proposed as follows:

400 kV system (Prévessin): An additional 400 kV bay, including a 400/66 kV transformer and circuit breaker. Displacement or modification (into two levels) of the existing 400 kV incoming overhead line will be required in order to gain the space for the transformer and circuit breaker.

66 kV system: The 400/66 kV transformer will supply a new 66 kV station with two outgoing feeders. One feeder is needed for the SPL EURISOL baseline, and there should be provision for a second one for possible SPL upgrades or future additional users. At the Meyrin end of the 66 kV cable, there will be a 66/18 kV transformer rated 70 MVA, feeding a new major 18 kV substation. It is proposed to install the 66/18 kV station in the close vicinity of the SPL to minimize cabling and electrical losses.

18 kV system (Meyrin): The 18 kV system will be the backbone of the SPL power distribution. The 18 kV substation will be directly behind the main 66/18 kV transformer, as the connection needs to transmit very high currents. As a rough estimation, a large substation with about 30 cubicles will be required to transmit the power of 40 MW. In addition, a 30 MVA bidirectional connection to the Meyrin 18 kV network (Station SW or ME9) is proposed in order to have a backup supply in both directions, for critical infrastructures. As for the LHC, the 18 kV station will be divided into two individual sections for Machine and General Services.

An 18 kV SVC will be required for harmonic filtering, voltage stabilization and reactive power control. It will consist of six or seven harmonic filters and a thyristor controlled rectifier for fast dynamic control.

3.3 kV system: It should be installed in conjunction with the cryogenics installation, to save civil-engineering costs by using a part of the cryogenic building. A first estimation points to a switchboard with approximately twelve to fifteen 3.3 kV cubicles. It may be required to feed the system from two sources, depending on the requirements of the project (e.g., diesel generator backup). The 18/3.3 kV transformers will be placed close to the 3.3 kV substation.

0.4 kV system: The 18/0.4 kV transformers and low-voltage switchboards always need to be installed in close vicinity of the load, to minimize voltage drop and electrical losses. It might be necessary to install some of these large components underground.

General Service installations: General services in the buildings and underground, as well as auxiliary and safety systems, would be designed using the standard solutions applied CERN-wide by the electrical service since the construction of LEP.

Generator backup: The SPL project with its associated critical systems (e.g., cryogenics) might require a dedicated 3.3 kV diesel generator backup of about 1 MW.

Uninterruptible power supplies (UPS): Safety critical systems (e.g., cryogenics controls) might require redundant uninterruptible power supplies, as used for the LHC.

5.5 Access control, safety, interlocks

As the SPL infrastructure is considered a primary beam area, an access control system and a machine interlock safety system will be installed to ensure personnel and equipment protection. The SPL infrastructure will be subdivided into three areas equipped with the usual CERN access equipment dedicated to primary beam area access (identification access points, search sectors).

The personnel protection is ensured by the machine interlock system; thus, in access mode, a VETO signal hampers any activation of specific machine equipment (beam stopper, RF modulators, power supplies). All the access procedures will be supervised by an operator from the CERN Control Centre (CCC). As for the existing PS primary beam areas, warnings will be activated in the SPL areas before beam operation.

The fire and gas detection policy will be based on the CERN Fire Protection Code [118] and on the CERN Flammable Gas Code [119]. CERN policy is to protect first and foremost the integrity of the people inside the installations, followed by the environment and the equipment. Consequently, and following the advice of the Safety Commission, adequate alarm systems will be installed in the linac tunnel and buildings.

Chapter 6

Design options

6.1 Upgrade options and their limitations

Generally there are three upgrade paths to achieve higher beam power with the SPL: lengthening the beam pulse, raising the final energy of the linac, or raising the beam current. All three options, which are discussed in the following, have to conform to the design rule of keeping uncontrolled beam losses below the threshold of 1 W/m. Furthermore, the installations in the SPL tunnel for electricity, cooling water, and cryogenics will have to be upgraded to meet the increased demands. The electrical infrastructure on the Meyrin site which has to be put into place for the nominal SPL (see Chapter 5, Section 5.4) already foresees the possibility of future upgrades. The infrastructure for cooling water and cryogenics will have to be upgraded in accordance with the operational experience of the nominal SPL.

6.1.1 Longer beam pulses

The maximum pulse length is determined by the 10% duty cycle of the 704.4 MHz pulsed klystrons. At 50 Hz repetition rate this duty cycle corresponds to a maximum RF pulse length of 2 ms. Taking into account the time needed to fill the SC cavities and to stabilize the cavity voltage, the theoretical maximum beam pulse length is $\approx$ 1.6 ms. Since the installed RF peak power is designed to cover an average pulse current of 40 mA, one could achieve a maximum beam power of $\approx$ 11 MW. The normal-conducting cavities below 180 MeV are designed for 15% duty cycle and the LEP klystrons used for this section were originally used in CW operation, so that there should be no bottleneck in this area. Depending on the required beam structure, the 3 MeV beam chopper, together with the MEBT, may have to be replaced. The only serious limitation for longer beam pulses is the availability of suitable H^- sources. At present, there is no H^- source available that is capable of delivering even the nominal SPL beam (see Chapter 4, Section 4.2.1). In the course of the R&D work for the SPL H^- source, it will become clear whether pulses of the order of 2 ms are realistic. If, on the other hand, part of the required high-power beam can be covered with protons instead of H^-, then it is conceivable to construct a second front end (source, RFQ, chopper) and to use a proton source capable of delivering high currents at high duty cycles.

Altogether a power upgrade by a factor of $\approx$ 2 using longer beam pulses seems to be realistic with only little investment.

6.1.2 Higher energy

A rise in beam energy can be achieved simply by adding more superconducting modules at the end of the linac. Every additional 75 m of SC cavities will raise the beam energy by 1 GeV and increase the beam power by $\approx$ 30% (compared to the nominal 3.5 GeV). In this case, however, a long enough tunnel has to be foreseen from the beginning of the construction to accommodate additional SC cavities. One of the limitations in this scenario is the increase in stripping losses due to a) the magnetic fields in the dipoles of any subsequent transfer line and b) the stripping of electrons due to black-body radiation of the beam pipe.

The magnetic stripping increases with rising beam energy and can be estimated with a simple formula for the H^- lifetime in magnetic fields (Ref. [120]). Using fits from experimental data [121, 122, 123], one can determine the maximum magnetic field to keep the beam loss per metre below a certain threshold. Figure 6.1(a) shows the resulting minimum arc radius for a 4 MW beam with a maximum acceptable loss level of 0.1 W/m for various beam energies. For this plot it was assumed that the arcs have a geometrical dipole filling factor of 60%. In Fig. 6.1(b) one can see the stripping losses with respect to the magnetic field strength in the arc dipoles, again assuming a 4 MW beam. For higher beam power the stripping losses will scale linearly with the beam power. For the installation on the CERN site

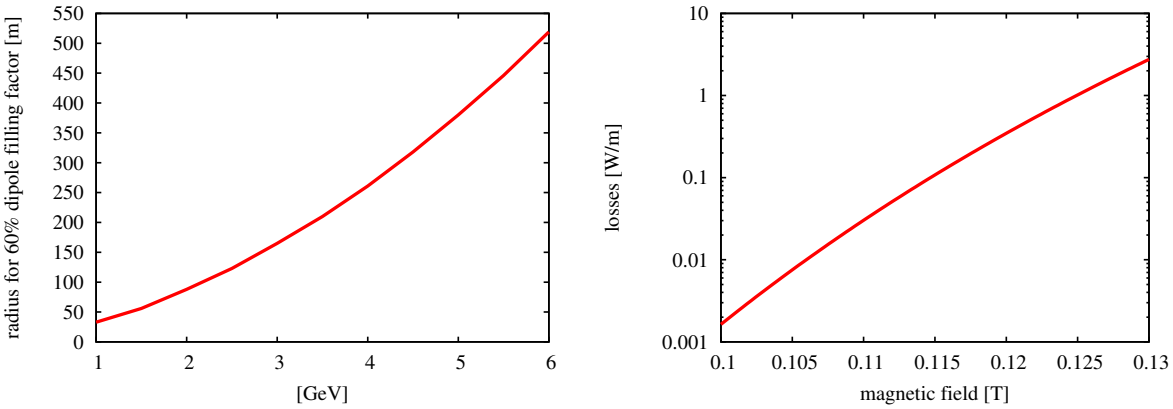

Fig. 6.1: (a) Minimum arc radius for a 4 MW beam for different energies, assuming 0.1 W/m stripping losses and 60% geometrical dipole filling factor (b) Stripping losses versus magnetic field strength in the arc dipoles (4 MW beam at 3.5 GeV)

it is preferable to have small bending radii in order to simplify the layout of transfer lines to the different users (PS, EURISOL, neutrino applications, etc.).

H^- stripping due to black-body radiation is a relatively new phenomenon and is still under study. Thermal photons are Doppler shifted so that their cross-section overlaps with that for H^- stripping. According to studies made for the Fermilab 8 GeV proton driver project [124, 125], the SPL beam at 3.5 GeV would experience stripping losses of the order of 1 W/m if the transfer line is operated at room temperature. Using a cold beam-screen inside the vacuum pipe, e.g., at nitrogen gas temperature (150 K), would reduce the stripping losses by more than a factor of 10 to approximately the same level as the assumed H^- stripping due to the magnetic fields in the bending dipoles.

An energy (and power) upgrade by a factor 2 seems realistic, although the difficulties connected with H^- stripping become much more severe at increasing energy levels. The only option to by-pass the problem of H^- stripping is to have a straight transfer line which is as short as possible. This option, however, is limited by the need to reduce the linac energy jitter via a system of debunching cavities, long drifts, and re-buncher cavities (see Chapter 4, Section 4.5.1).

6.1.3 Higher current

A significant increase in beam current will be severely limited by the availability of suitable H^- sources and will possibly require the installation of two new front ends (source, RFQ, chopper line) together with a beam funnel before the DTL. Furthermore, this option requires the installation of additional klystrons in the existing klystron gallery and a re-installation of the complete RF power distribution system. Higher currents will yield increased space-charge forces and emittance growth, and will thus make it more difficult to keep the beam losses below 1 W/m. In particular, the beam transport in the chopper line or the beam dynamics in a beam funnel pose significant risks for emittance blow up. In the SC section new power couplers with higher power transmission capabilities would be needed and the higher beam loading in the SC cavities will make it more difficult to control the RF phases and amplitudes at the required levels.

Small increases in beam current ($< 10\%$) may, however, be possible since most systems are designed with a certain safety margin.

6.2 Failure scenarios

6.2.1 Machine and personnel protection

The machine (MPS) and personnel protection systems (PPS) will follow the established CERN safety rules as mentioned in Chapter 5, Section 5.5.

The fastest element to switch off the beam is the H^- ion source. However, stops of several minutes or hours will destabilize the source and long start-up times may be required for a re-start. The down-time of the source can be reduced to 1–2 s if a beam stopper is used in the LEBT, which needs approximately 1 s to be inserted into the beam line. In order to have a redundant safety system, a second beam stopper should be foreseen in the LEBT.

The area downstream of the linac will be protected by switching off the first bending magnet in the transfer line connecting the linac with either the accumulator/compressor ring or the subsequent users and/or accelerators. At the same time a beam plug will be inserted in the transfer line while the beam is collected in a low-power dump at the end of the linac.

Once the beam is cut off at low energy there will still be a bunch train of $\approx 2.5\,\mu$s coming out of the linac, carrying an energy of ≈ 0.5 kJ. In the worst case, however, one should consider a full linac pulse reaching the dump, yielding an instantaneous power of 140 MW over 0.8 ms/0.6 ms in case of EURISOL/neutrino operation. The average power rating of the dump should be ≈ 100 kW, which allows setting up the machine with full current at a 1 Hz duty cycle. The accidental loss of the full beam at top energy has been analysed in Chapter 5, Section 5.1 and approximately yields to a dose rate which is equivalent to one hour of nominal operation, provided that the beam can be switched of within 10 ms (five pulses).

6.2.2 Machine operation with loss of non-critical systems

The SPL is designed to use single klystrons for several normal-conducting or superconducting cavities, which means that there is no possibility of operating the linac with one or more failing klystrons. The failure of single klystrons will entail down-times of 1–3 days, needed to replace the faulty device. The loss of superconducting cavities (e.g., due to quenches, multipacting in the power coupler, failing RF windows, etc.), however, can entail down-times of several months if the cryostats need to be opened. In this case it is highly desirable to be able to accept the failure of single cavities for continued operation.

Failure studies for Accelerator Driven Systems (ADS) [126] show that superconducting linacs can operate with a certain 'fault tolerance' to failing cavities or quadrupoles if the control system is programmed to re-tune the surrounding elements. If one cavity in a string becomes unavailable, it must be detuned using mechanical tuners so that a) the incoming power from the generator will be fully reflected via a circulator into an RF load, and b) the beam does not lose energy by exciting a cavity mode. Since it is unlikely that the piezo-tuners can provide a sufficient detuning, one has to consider the time constant of the slower mechanical tuners for this process. Since the SPL accelerates a non-relativistic beam, a missing cavity will result in a phase and energy error which is more severe for lower particle velocities. In order to restore the nominal energy and phase value at some point after the failing cavity, the field amplitude in the surrounding cavities has to be raised and the phase needs to be adjusted to compensate for the missing cavity. Additionally, several quadrupoles should be adjusted to minimize the transverse mismatching of the beam. Simulations reported in Ref. [126] show that using this procedure one can re-tune the system so that no additional beam loss is created. However, one must foresee the installation of sufficient RF loads to cope with the reflected power (not included in this report) and there has to be enough operational margin (range of phase/amplitude shifters, cavity tuners, etc.) so that the RF system can continue to operate. Furthermore, the control system must be programmed with the appropriate cavity and quadrupole settings needed for the compensation of each possible failure scenario. Only then can the beam be restored with a minimum time delay.

Acknowledgements

This report would not have been possible without the work of many collaborating institutes. In addition to the authors mentioned in the author list we would like to thank our Russian colleagues at ITEP (Moscow), VNIIEF (Sarov), BINP (Novosibirsk) and VNIITF (Snezinsk), and our Indian colleagues at CAT (Indore) and BARC (Mumbai) for their valuable contributions. In addition, our study benefits from ongoing discussion with our colleagues at SNS and Fermilab.

References

[1] P. Zucchelli, A novel concept for a $\bar{\nu}_e/\nu_e$ neutrino factory: the beta-beam, *Phys. Lett.* **B 532** (2002) 166. [http://cdsweb.cern.ch/record/588640] 1, 9

[2] J.E. Campagne and A. Caze, The θ_{13} and δ_{CP} sensitivities of the SPS-Fréjus project revisited, CERN-NUFACT-NOTE 142 (2004) [LAL-2004-102]. [http://cdsweb.cern.ch/record/806547] 1, 3, 9

[3] The SPL Study Group, Conceptual design of the SPL a high power superconducting H^- linac at CERN, CERN 2000-012 (2000), Ed. M. Vretenar. [http://cdsweb.cern.ch/record/489425] 3, 5, 13, 26, 49, 50, 51, 55

[4] P. Gruber *et al.,* The study of a European neutrino factory complex, CERN-NUFACT-NOTE 122 (2002) [CERN/PS/2002-080 (PP)]. [http://cdsweb.cern.ch/record/610249] 3

[5] M. Benedikt, K. Cornelis, R. Garoby, E. Métral, F. Ruggiero and M. Vretenar, Report of the High Intensity Protons Working Group, CERN-AB-2004-022 OP/RF (2004). [http://cdsweb.cern.ch/record/734636] 3

[6] E. Métral *et al.,* High-intensity proton beams at CERN and the SPL study, Proc. 3rd Asian Particle Accelerator Conf., Gyeongju, Korea, 2004, e-proceedings (JACoW, Geneva, 2004), p. 539 [CERN-AB-2004-021-ABP]. [http://cdsweb.cern.ch/record/733603] 3

[7] M. Benedikt *et al.,* Preliminary accelerator plans for maximizing the LHC integrated luminosity, CERN-AB-2006-018-PAF (2006). [http://cdsweb.cern.ch/record/946248] 3

[8] M. Benedikt and R. Garoby, High brightness proton beams for LHC: needs and means, First CARE-HHH-APD Workshop on Beam Dynamics in Future Hadron Colliders and Rapidly Cycling High-Intensity Synchrotrons, HHH 2004, CERN, Geneva, Switzerland, 2004, CERN-2005-006, pp. 203–207. [http://cdsweb.cern.ch/record/815739] 3

[9] K. Hanke *et al.,* Superconducting proton linac development at CERN, Proc. 34th ICFA Advanced Beam Dynamics Workshop on High Power Superconducting Ion, Proton, and Multi-Species Linacs, Naperville, United States, 2005 [CERN-AB-2005-053]. [http://cdsweb.cern.ch/record/882237] 3

[10] S.J. Brooks and K.A. Walaron, Computed pion yields from a tantalum rod target: comparing MARS15 and GEANT4 across proton energies, Proc. 7th International Workshop on Neutrino Factories and Superbeams, Frascati, Italy, 2005. 3

[11] K.A. Walaron, Simulations of pion production in a tantalum rod target using GEANT4 with comparison to MARS, UKNF-NOTE-30 (2005). 3

[12] EURISOL Design Study, http://eurisol.org. 4, 10

[13] E. Noah, F. Gerigk, J. Lettry, M. Lindroos and T. Stora, EURISOL target stations operation and implications for its proton linac driver beam, to be published in Proc. European Particle Accelerator Conf., Edinburgh, United Kingdom, 2006. 4

[14] A. Herrera-Martínez and Y. Kadi, EURISOL-DS multi-MW target, preliminary study of the liquid metal proton-to-neutron converter, EURISOL-DS/TASK2/TN-05-01 (2005), CERN-AB-Note-2006-013 ATB. [http://cdsweb.cern.ch/record/934206] 4

[15] Spallation Neutron Source home page, http://www.sns.gov. 4, 5, 47, 50

[16] European Spallation Source, http://neutron.neutron-eu.net/n_ess. 4

[17] H. Padamsee, J. Knobloch and T. Hays, *RF Superconductivity for Accelerators*, Wiley series in beam physics and accelerator technology (John Wiley and Sons, 1998). [http://cdsweb.cern.ch/record/366783] 5

[18] D.A. Edwards (Ed.), TESLA test facility linac design report, DESY Print TESLA 95-01 (1995). [http://cdsweb.cern.ch/record/282046] 5

[19] R. Brinkmann *et al.,* TESLA technical design report, part II: the accelerator, DESY 2001-011 (2001) [ECFA 2001-209, TESLA Report 2001-23, TESLA-FEL 2001-05]. [http://tesla.desy.de/new_pages/TDR_CD/PartII/accel.html] 5, 38

[20] L. Lilje, High gradients in multi-cell cavities, Proc. 11th International Workshop on RF Superconductivity, Travemünde, Germany, 2003. 5, 32

[21] J.F. Tooker *et al.,* Overview of the APT accelerator design, Proc. Particle Accelerator Conf., New York, 1999 (IEEE, Piscataway, NY, 1999), p. 3567. [http://cdsweb.cern.ch/record/452157] 5

[22] A. Bosotti *et al.,* RF tests of the beta = 0.5 five cell TRASCO cavities, Proc. 9th European Particle Accelerator Conf., Lucerne, Switzerland, 2004, e-proceedings (JACoW, Geneva, 2004), p. 1024. [http://cdsweb.cern.ch/record/822793] 5, 33, 35

[23] J.L. Biarrotte *et al.,* 704 MHz superconducting cavities for a high intensity proton accelerator, Proc. 9th Workshop on RF Superconductivity, Santa Fe, United States, 1999. 5

[24] B. Visentin *et al.,* Experimental results on 700 MHz multicell superconducting cavity for proton linac, Proc. Particle Accelerator Conf., Portland, OR, United States, 2003 (IEEE, Piscataway, 2003), p. 1303. [http://cdsweb.cern.ch/record/748780] 5, 33, 35

[25] G. Ciovati *et al.,* Superconducting prototype cavities for the Spallation Neutron Source (SNS) project, Proc. Particle Accelerator Conf., Chicago, IL, United States, 2001 (IEEE, New York, 2002), p. 484. [http://cdsweb.cern.ch/record/533311] 5, 33, 35

[26] C.C. Compton *et al.,* Prototyping of a multicell superconducting cavity for acceleration of medium-velocity beams, *Phys. Rev. Special Topics Acc. Beams* **8** (2005) 042003. 5, 33, 35

[27] S. Calatroni, 20 years of experience with the Nb/Cu technology for superconducting cavities and perspectives for future developments, Proc. 12th Workshop on RF Superconductivity, Ithaca, NY, United States, 2005 [CERN-TS-2005-001]. [http://cdsweb.cern.ch/record/920988] 5

[28] O. Aberle *et al.*, Technical developments on reduced-beta superconducting cavities at CERN, Proc. Particle Accelerator Conf., New York, United States, 1999 (IEEE, Piscataway, 1999), p. 949 [CERN-SL-99-024-CT]. [http://cdsweb.cern.ch/record/387156] 5

[29] C. Pagani *et al.,* Improvement of the blade tuner design for superconducting RF cavities, Proc. Particle Accelerator Conf., Knoxville, United States, 2005, CARE-Conf-05-052-SRF, CARE-Conf-05-012-HIPPI. [http://cdsweb.cern.ch/record/943250] 5

[30] P. Sekalski, S. Simrock and A. Napieralski, Piezoelectric stack based system for Lorentz-force compensation caused by high field in superconducting cavities, Proc. 12th International Workshop on RF Superconductivity, Ithaca, United States, 2005, CARE-Conf-05-050-SRF. [http://cdsweb.cern.ch/record/943248] 5

[31] P. Pierini, Analysis of gradients for future high-gradient proton accelerators, Proc. 34th ICFA Advanced Beam Dynamics Workshop on High Power Superconducting Ion, Proton, and Multi-Species Linacs, Naperville, United States, 2005. 5

[32] F. Gerigk *et al.,* Progress in the design of Linac4, the SPL normal conducting front-end (< 180 MeV), Proc. 34th ICFA Advanced Beam Dynamics Workshop on High Power Superconducting Ion, Proton, and Multi-Species Linacs, Naperville, United States, 2005 [CERN-AB-2005-055]. [http://cdsweb.cern.ch/record/884655] 6, 26

[33] R. Garoby *et al.,* Linac4, a new H^- linear injector at CERN, Proc. 19th Russian Particle Accelerator Conf. (RUPAC), Dubna, Russia, 2004, e-proceedings (JACoW, Geneva, 2004), p. 28 [CERN-AB-2005-012]. [http://cdsweb.cern.ch/record/818568] 6

[34] R. Garoby, F. Gerigk, K. Hanke, A. Lombardi, C. Rossi and M. Vretenar, Design of Linac4, a new injector for the CERN booster, Proc. 22nd International Linear Accelerator Conf., Lübeck, Germany, 2004, e-proceedings (JACoW, Geneva, 2004), p. 291 [CERN-AB-2004-104-RF]. [http://cdsweb.cern.ch/record/806551] 6

[35] F. Gerigk and M. Vretenar, Design of a 120 MeV H^- Linac for CERN high-intensity applications, Proc. 21st International Linear Accelerator Conf., Gyeongju, Korea, 2002 (Pohang Accelerator Laboratory, Pohang, 2002), p. 73 [CERN-PS-2002-069-RF]. [http://cdsweb.cern.ch/record/581341] 6, 30

[36] M. Martini and C.R. Prior, High-intensity and high-density charge-exchange injection studies into the CERN PS booster at intermediate energies, Proc. 9th European Particle Accelerator Conf. Lucerne, Switzerland, 2004, e-proceedings (JACoW, Geneva, 2004), p. 1891 [CERN-AB-2004-069]. [http://cdsweb.cern.ch/record/791846] 6

[37] Neutrino Factory and Muon Collider Collaboration, Feasibility Study II, http://www.cap.bnl.gov/mumu/studyii/FS2-report.html. 9

[38] Y. Mori, Neutrino factory in Japan, Proc. International Workshop on Neutrino Factories, London, United Kingdom, 2002 [*J. Phys. G: Nucl. Part. Phys.* **29** (2003) 1527]. [http://cdsweb.cern.ch/record/584731] 9

[39] International Scoping Study of a Future Neutrino Factory and Super-beam Facility, http://www.hep.ph.ic.ac.uk/iss/. 9

[40] HARP experiment home page, http://harp.web.cern.ch/harp. 9

[41] BENE Steering Group, Beams for European neutrino experiments (BENE), Midterm scientific report, CARE-Report-06-009-BENE, CERN-2006-005, ECFA/06/242 (2006). [http://cdsweb.cern.ch/record/955252] 9

[42] The EURISOL Report, Appendix A, The Physics Case for EURISOL, http://www.ganil.fr/eurisol/Final_Report/Appendix-A.pdf. 10

[43] NUPECC, Nuclear Science: Impact, Applications, Interactions, http://www.nupecc.org/iai2001. 10

[44] R. Garoby and M. Vretenar, Proposal for a 2 GeV linac injector for the CERN PS, PS/RF/Note 96-27 (1996). 12

[45] D. Boussard *et al.,* Report of the study group on a superconducting proton linac as a PS injector, CERN/PS 98-063 (RF-HP) (1998). [http://cdsweb.cern.ch/record/379059] 13

[46] The Large Hadron Collider: conceptual design, CERN/AC/95-05 (LHC) (1995). [http://cdsweb.cern.ch/record/291782] 13

[47] Proton Accelerators for the Future, Inter-Departmental Working Group, http://paf.web.cern.ch/paf. 14

[48] C. Rossi *et al.,* The SPL front end: a 3 MeV H^- test stand at CERN, Proc. International Linear Accelerator Conf., Lübeck, Germany, 2004, e-proceedings (JACoW, Geneva, 2004), p. 294 [CERN-AB-2004-102-RF]. [http://cdsweb.cern.ch/record/806549] 15, 21

[49] M. Vretenar and R. Garoby, Overview of high intensity linac programs in Europe, Proc. 22nd International Linear Accelerator Conf., Lübeck, Germany, 2004, e-proceedings (JACoW, Geneva, 2004), p. 559 [CERN-AB-2004-042-RF]. [http://cdsweb.cern.ch/record/790197] 15

[50] HIPPI home page, http://mgt-hippi.web.cern.ch/mgt-hippi/. 15, 51

[51] J. Peters, Negative ion sources for high energy accelerators, *Rev. Sci. Instrum.* **71** (1999) 1069. 16

[52] R. Scrivens, Proton and ion sources for high intensity accelerators, Proc. 9th European Particle Accelerator Conf., Lucerne, Switzerland, 2004, e-proceedings (JACoW, Geneva, 2004), p. 103 [CERN-AB-2004-075]. [http://cdsweb.cern.ch/record/793626] 16

[53] J. Peters, New developments in RF-driven multicusp H^- ion sources, Proc. International Conf. on Ion Sources, Caen, France, 2005 [to be published in *Rev. Sci. Instrum.*]. 16

[54] J. Peters, The HERA Volume H^- source, Proc. Particle Accelerator Conf., Knoxville, United States, 2005 (IEEE, Piscataway, NY, 2005), p. 788. [http://cdsweb.cern.ch/record/927080] 16, 17

[55] M. Weiss, The RFQ2 complex: the future injector to CERN Linac2, Proc. 3rd European Particle Accelerator Conference, Berlin, 1992 (Edition Frontières, Gif-sur-Yvette, 1992), p. 539 [CERN/PS 92-34 (HI)]. [http://cdsweb.cern.ch/record/238556] 16

[56] T. Steiner, H^- source ion source developments and diagnostics at CERN, Ph.D. thesis, Technical University Vienna, 2005. 17

[57] P.-Y. Beauvais, Recent evolutions in the design of the French high intensity proton injector (IPHI), Proc. 9th European Particle Accelerator Conf., Lucerne, Switzerland, 2004, e-proceedings (JACoW, Geneva, 2004), p. 1273. [http://cdsweb.cern.ch/record/822865] 18, 43, 53

[58] B. Bondarev *et al.*, Multilevel codes RFQ.3L for RFQ designing, Proc. Computational Accelerator Physics Conf., Williamsburg, VA, United States, 1996, AIP Conf. Proc. 391 (AIP, Woodbury, NY, 1997). 20

[59] S.S. Kurennoy and J.F. Power, Development of meander-line current structure for SNS fast 2.5 MeV beam chopper, Proc. 7th European Particle Accelerator Conf., Vienna, Austria, 2000 (E.P.S., Geneva, 2000), p. 336. [http://cdsweb.cern.ch/record/505148] 22

[60] F. Caspers *et al.,* The CERN-SPL chopper concept and final layout, Proc. 9th European Particle Accelerator Conf., Lucerne, Switzerland, 2004, e-proceedings (JACoW, 2004), p. 1141 [CERN-AB-2004-049]. [http://cdsweb.cern.ch/record/790647] 22, 23

[61] F. Caspers, A. Mostacci and S. Kurennoy, Fast chopper structure for the CERN Superconducting Proton Linac, Proc. 8th European Accelerator Conf., Paris, France, 2002 (E.P.S., Geneva, 2002), p. 873 [CERN-PS-2002-027-RF]. [http://cdsweb.cern.ch/record/562006] 22, 23

[62] U. Barabas, On an ultrabroad-band hybrid tee, *IEEE Trans. Microwave Theory Tech.* **MTT-27** (1979) 1. 24

[63] M. Paoluzzi, Status of CERN chopper driver and the solid state alternative, CARE/HIPPI Document-2005-003 (2005) [CERN-AB-Note-2005-031].
[http://cdsweb.cern.ch/record/854660] 25

[64] F. Gerigk and M. Vretenar, Design choices for the SPL normal-conducting front end (3–120 MeV), CERN NUFACT-NOTE 110 (2002), PS/RF Note 2002-038.
[http://cdsweb.cern.ch/record/689906] 26

[65] M. Pasini, Phase and amplitude error study for the Linac4 RF system, CARE HIPPI-DOCUMENT 05-006 (2005). 26

[66] J. Billen, F. Krawczyk, R. Wood and L. Young, A new RF structure for intermediate-velocity particles, Proc. 17th International Linac Conf., Tsukuba, Japan, 1994. 28

[67] Y. Cuvet *et al.,* Development of a 352 MHz cell-coupled drift tube linac prototype, Proc. 22nd International Linear Accelerator Conf., Lübeck, Germany, 2004, e-proceedings (JACoW, Geneva, 2004), p. 288 [CERN-AB-2004-103]. [http://cdsweb.cern.ch/record/806550] 30

[68] E. Benedico Mora and M. Vretenar, Design of a side-coupled linear accelerator structure for Linac4, CERN-AB-Note-2005-044 RF. [http://cdsweb.cern.ch/record/912283] 31

[69] E.A. Knapp, B.C. Knapp and J.M. Potter, Standing wave high energy linear accelerator structure, *Rev. Sci. Instrum.* **39** (1968) 979. 31

[70] C. Pagani *et al.,* Design criteria for elliptical cavities, Proc. 10th Workshop on RF Superconductivity, Tsukuba, Japan, 2001. 33

[71] B. Aune *et al.*, Superconducting TESLA cavities, *Phys. Rev. Special Topics Acc. Beams* **3** (2000) 092001. [http://cdsweb.cern.ch/record/429906] 33

[72] D. Barni *et al.,* RF tests of the single cell prototypes for the TRASCO $\beta = 0.47$ cavities, Proc. 8th European Particle Accelerator Conf., Paris, France, 2002 (E.P.S., Geneva, 2002), p. 2277.
[http://cdsweb.cern.ch/record/584788] 33

[73] J. Delayen *et al.,* Performance overview of the production of superconducting RF cavities for the Spallation Neutron Source linac, Proc. Particle Accelerator Conf., Knoxville, United States, 2005. 34, 35

[74] All the statistics of the TTF cavity treatments and tests are accessible from the TESLA-Technology Collaboration web site at http://tesla.desy.de, (cavity information database). 34

[75] L. Lilje, High gradient multicell superconducting cavities, Proc. 21st International Linear Accelerator Conf., Gyeongju, Korea, 2002 (Pohang Accelerator Laboratory, Pohang, 2002), p. 219. [http://cdsweb.cern.ch/record/728965] 34

[76] See http://www.linearcollider.org for information on the global design effort and the ILC. 35

[77] L. Lilje, State of the art SRF cavity performances, Proc. 22nd International Linear Accelerator Conference, Lübeck, Germany, 2004, e-proceedings (JACoW, Geneva, 2004), p. 518. [http://cdsweb.cern.ch/record/925563] 35

[78] C. Pagani *et al.,* Construction, commissioning and cryogenic performances of the first TESLA test facility (TTF) cryomodule, *Adv. Cryog. Eng.* **43** (Plenum Press, New York, 1998). 38

[79] W.J. Schneider *et al.,* Design of the SNS cryomodule, Proc. Particle Accelerator Conf., Chicago, United States, 2001 (IEEE, New York, 2002), p. 1160. 38

[80] The ILC Baseline Configuration Document is available from the web site http://www.linearcollider.org. 38

[81] R. Duperrier, N. Pichoff and D. Uriot, CEA Saclay codes review, Proc. International Conf. on Computational Science, Amsterdam, The Netherlands, 2002. 41

[82] A. Perrin and J.F. Amand, Travel v4.06, user manual, CERN (2003). 41

[83] A. B. Ismaïl, R. Duperrier, D. Uriot and N. Pichoff, Space charge compensation in low energy proton beams, Proc. 22nd International Linear Accelerator Conf., Lübeck, Germany, 2004, e-proceedings (JACoW, Geneva, 2004), p. 324. 42

[84] I.A. Soloshenko, Problems of intense negative ion beam transport, *Rev. Sci. Instrum.* **75** (2004) 1694. 42

[85] C.F. Bamett, Collisions of H, H{2}, Atomic Data for Fusion, Vol. 1: He and Li atoms and ions with atoms and molecules, Report ORNL-6086 (1990), see http://www-amdis.iaea.org/ALADDIN/. 42

[86] J. Heinemeier, P. Hvelplund and F.R. Simpson, Collisional detachment cross sections for H^- and He^- at high energies, *J. Phys. B: At. Mol. Phys.* **9** (1976) 2669. 42

[87] C.J. Anderson, R.J. Girnius, A.M. Howald and L.W. Anderson, Production of fast H_0 atoms by stripping H^- ions in gas and vapor targets, *Phys. Rev.* **A 22** (1980) 822. 42

[88] R. Ferdinand *et al.,* Status report on the 5 MeV IPHI RFQ, Proc. 20th International Linear Accelerator Conf., Monterey, United States, 2000, e-proceedings (JACoW, Geneva, 2000), p. 551. 43

[89] R. Ferdinand, P. Mattei and R. Duperrier, Le RFQ du projet IPHI, DSM/DAPNIA/SEA/IPHI 99/62 (1999). 43

[90] M. Baylac, technical note in preparation. 44

[91] I. Hofmann, Stability of anisotropic beams with space charge, *Phys. Rev.* **E 57** (1998) 4713. 44

[92] TESLA Technical Design Report: http://tesla.desy.de/new_pages/TDR_CD/start.html (2001). 50, 56, 57, 58

[93] ILC Global Design Effort: http://www.interactions.org/linearcollider/gde/. 50

[94] L. Lilje, Piezo tuner options for the next module, talk: http://www-zeuthen.desy.de/tesla2004/talks/wg1/piezo_plan_lilje.pdf (2004). 50

[95] J. Tückmantel, SPLinac: computer simulations of SC linac RF systems with beam, Proc. 10th Workshop on RF Superconductivity, Tsukuba, Japan, 2001, CERN-SL-2001-056-HRF (2001). [http://cdsweb.cern.ch/record/522703] 51

[96] J. Tückmantel, SPLinac, a program to simulate SC linac RF systems with beam, CERN-SL-Note-2000-053-HRF (2000). [http://cdsweb.cern.ch/record/702620] 51

[97] J. Tückmantel, Simulation of the SPL SC RF system with beam using "SPLinac", CERN-NUFACT-Note-64 [CERN-SL-Note-2000-054-HRF] (2000). [http://cdsweb.cern.ch/record/497871] 51

[98] J. Tückmantel, Control instabilities in a pulsed multi-cavity RF system with vector sum feedback (a mathematical analysis), CERN-SL-Note-2001-023-HRF (2001). [http://cdsweb.cern.ch/record/702659] 51

[99] H. Frischholz, private communication (2000–2003). 51

[100] D. Valuch, High CW power, phase and amplitude modulator realized with fast ferrite phase-shifters, Ph.D. thesis, Slovak University of Technology, Bratislava [CERN-THESIS-2005-021] (2005). [http://cdsweb.cern.ch/record/835268] 51

[101] H. Frischholz, J. Tückmantel, D. Valuch and C. Weil, First results with a fast phase and amplitude modulator for high power RF application, Proc. European Accelerator Conf., Lucerne, Switzerland, 2004 [CERN-AB-2004-052]. [http://cdsweb.cern.ch/record/790650] 51, 55

[102] E. Bravin, Thermal analysis of a metallic foil under a proton beam load for the SPL chopper, CERN/PS/BD/Note 2002-132 (2002). 53

[103] E. Sargsyan, K. Hanke and A. Lombardi, Simulations of the beam diagnostics line for the SPL 3 MeV chopper line, CERN-AB-Note-2004-053 (2004). [http://cdsweb.cern.ch/record/746299] 53

[104] K. Hanke and M. Hori, Design and construction of a beam shape and halo monitor for the CERN SPL, CARE-Note-2005-013-HIPPI (2005) [CERN-AB-Note-2005-033 OP]. [http://cdsweb.cern.ch/record/860947] 54

[105] 2005 International Linear Collider Physics and Detector Workshop and 2nd ILC Accelerator Workshop, Snowmass, United States, 2005. 55

[106] H. Frischholz and D. Valuch, Operation of LEP CW klystrons in pulsed mode, Proc. Particle Accelerator Conf., Portland, United States, 2003 [CERN-AB-2003-043-RF]. [http://cdsweb.cern.ch/record/619610] 55

[107] D. Valuch, A fast phase and amplitude modulator for the SPL, Proc. 34th ICFA Advanced Beam Dynamics Workshop on High Power Superconducting Ion, Proton, and Multi-Species Linacs, Naperville, United States, 2005. 55

[108] F. Gerigk, Formulae to calculate the power consumption of the SPL SC cavities, CERN-AB-Note-2006-011 RF (2006). [http://cdsweb.cern.ch/record/931597] 55

[109] LHC Design Report Volume 1: the LHC Main Ring, CERN-2004-003-V-1. [http://cdsweb.cern.ch/record/782076] 56

[110] ILC Technical Design Report, to be published 2006. 56

[111] M. Magistris and M. Silari, Shielding requirements and induced radioactivity in the 3.5 GeV version of the SPL, CERN-SC-2005-067-RP-TN (2005). 62, 63, 65

[112] H. Nakashima *et al.,* Estimation of activity and dose distributions around a proton linac induced by beam spill, *J. Nucl. Sci. Technol.*, **Suppl. 1** (2000) 870. 62

[113] CERN Radiation Safety Manual, Safety Code F (1996). 62

[114] A. Fassò *et al.,* Shielding against high energy radiation, in Landolt-Börnstein, *Numerical Data and Functional Relationships in Science and Technology, New Series, Group I: Nuclear and Particle Physics*, Ed. H. Schopper (Springer-Verlag, Berlin, 1990), Vol. 11. [http://cdsweb.cern.ch/record/214135] 62

[115] M. Magistris and M. Silari, Preliminary shielding design of Linac4, CERN-SC-2005-011-RP-TN (2005). 63

[116] M. Magistris and M. Silari, Preliminary shielding design of Linac4. Top shielding and induced radioactivity, CERN-SC-2005-RP-TN (2005). 63

[117] R.H. Thomas and G.R. Stevenson, Radiological safety aspects of the operation of proton accelerators, Technical Report 283 (International Atomic Energy Agency, Vienna, 1988). [http://cdsweb.cern.ch/record/112571] 63, 64, 65

[118] CERN Fire Protection Code, E, Rev., Revision 1995. 77

[119] Flammable Gas Safety Code, CERN Safety Code, G, Rev., Revision 1996. [http://cdsweb.cern.ch/record/330282] 77

[120] L.R. Scherk, An improved value for the electron affinity of the negative hydrogen ion, *Can. J. Phys.* **57** (1979) 558. 78

[121] G.M. Stinson *et al.,* Electric dissociation of H^- ions by magnetic fields, *Nucl. Instrum. Methods*, **74** (1969) 333. 78

[122] A.J. Jason, D.W. Hudgings and O.B. van Dyck, Neutralisation of H^- beams by magnetic stripping, *IEEE Trans. Nucl. Sci.* **28** (1981) 2704. 78

[123] P.B. Keating *et al.,* Electric-field-induced detachment of 800-MeV H^- ions, *Phys. Rev.* **A 52** (1995) 4547. 78

[124] W. Chou *et al.,* 8 GeV H^- ions: transport and injection, Proc. Particle Accelerator Conf., Knoxville, United States, 2005. 79

[125] H.C. Bryant and G.H. Herling, Atomic physics with a relativistic H^- beam, *J. Modern Optics* **53** (2006) 45. 79

[126] J-L. Biarrotte *et al.,* Beam dynamics studies for the fault tolerance assessment of the PDS-XADS linac design, Proc. 9th European Particle Accelerator Conf., Lucerne, Switzerland, 2004, e-proceedings (JACoW, Geneva, 2004), p. 1282. 80

Appendix: SPL parameter list

Parameter	Value	Comment
General linac parameters		*Tables 2.1 and 2.2*
Energy	3.56 GeV	
Beam power	4/5 MW	'Neutrino'/'EURISOL'
Bunch frequency	352.2 MHz	
Peak current	64 mA	Output
Average pulse current	40 mA	Output
Beam duty cycle (after chopper)	2.9/3.6%	'Neutrino'/'EURISOL'
Peak RF power	161.6 MW	Installed RF systems
Average RF plug power	17/21 MW	'Neutrino'/'EURISOL'
Repetition rate	50 Hz	
Beam pulse length	0.57/0.71+0.014 ms	'Neutrino'/'EURISOL'
RF efficiency	0.5/0.85/0.95	Klystron/power conv./waveguide
Number of 352.2 MHz klystrons	14	1 MW peak
Number of 704.4 MHz klystrons	44	5 MW peak
Primary cooling linac	16.8 MW	Heat capacity, *Table 5.5*
	1600 m^3/h	($\Delta T = 9$ K, $\Delta P = 5$ bar)
Cryo-compressors	3.6/4.4 MW	Heat capacity 'neutrino'/'EURISOL'
	600 m^3/h	($\Delta T = 5.7$ K, $\Delta P = 5$ bar)
Elec. power cooling/ventilation	4 MW	*Table 5.8*
Total power consumption	32/37 MW	'Neutrino'/'EURISOL', *Table 5.9*
Length	429 m	Without debuncher
Tunnel length	470 m	Including access area
Normal-conducting linac		
Energy	180 MeV	
RF frequency	352.2/704.4 MHz	0.095–90 MeV/90–180 MeV
Peak RF power	26.4 MW	Installed RF systems
Average RF power	0.9/1.2 MW	'Neutrino'/'EURISOL'
Average RF plug power	2.2/3 MW	'Neutrino'/'EURISOL'
Length	87 m	
Error amplitudes		Maximum, uniform distribution
Quadrupole gradient	$\pm 0.5\%$	
Quadrupole displacement	± 0.1 mm	
Quadrupole rotation (x,y)	± 0.5 deg	
Quadrupole rotation (z)	± 0.2 deg	
Cavity field phase	± 1 deg	
Cavity field amplitude	$\pm 1\%$	
Superconducting linac		
Input energy	180 MeV	
Output energy	3.56 GeV	
RF frequency	704.4 MHz	
Peak RF power	135.2 MW	Installed RF systems
Average RF power	6.0/7.2 MW	
Average RF plug power	14.9/17.8 MW	
Length	342 m	

table continued on next page

Parameter	Value	Comment
Cryogenic temperature	2 K	
Error amplitudes		Maximum, uniform distribution
Quadrupole gradient	$\pm 0.5/\pm 0.05\%$	Static/dynamic
Quadrupole displacement	$\pm 0.5/\pm 0.01$ mm	Static/dynamic
Quadrupole rotation (x,y)	$\pm 0.25/\pm 0.005$ deg	Static/dynamic
Quadrupole rotation (z)	$\pm 0.5/\pm 0.05$ deg	Static/dynamic
Cavity displacement	$\pm 0.5/\pm 0.01$ mm	Static/dynamic
Cavity rotation (x,y)	$\pm 0.08/\pm 0.005$ deg	Static/dynamic
Cavity field phase	± 1 deg	
Cavity field amplitude	$\pm 1\%$	
Ion source and LEBT		*Section 4.2.1*
Ion species	H^-	
Source current	80 mA	
Extraction voltage	95 kV	
Source length	1 m	
LEBT focusing type	solenoid	
LEBT length	<2 m	
Transverse output emittance	0.25 π mm mrad	(r.m.s., normalized)
Vacuum	10^{-5} mbar	
RFQ		*Table 4.1*
Input energy	0.095 MeV	
Output energy	3.0 MeV	
RF frequency	352.2 MHz	
Peak current	70 mA	
Average pulse current	70 mA	
Design current	100 mA	CW
Design duty cycle	100%	
Voltage	87–122 kV	
Modulation factor	1.0–1.7	
Maximum surface field	1.7 kilpatrick	
RF beam power	210 kW	(70 mA)
RF peak power (superfish)	884 kW	
RF peak power (expected)	1020 kW	
Number of klystrons	1	
No. of cells	560	
Length	5.95 m	
Beam aperture	3.7–4.1 mm	
Transverse output emittance	0.28 π mm mrad	r.m.s., normalized
Longitudinal output emittance	0.15 π deg MeV	At 352.2 MHz
	0.38 π mm mrad	r.m.s., normalized
Vacuum	10^{-7} mbar	
MEBT (chopper line)		*Table 4.3*
Beam energy	3 MeV	
Peak current	70/64 mA	Input/output
Average pulse current	70/40 mA	Input/output
Effective chopper plate voltage	400 V	Seen by beam

table continued on next page

Parameter	Value	Comment
Chopper plate voltage	500 V	
Chopper rise/fall time	< 2 ns	10–90%
Maximum chopper frequency	44 MHz	
Chopper repetition rate	1–50 Hz	
Maximum chopping factor	40%	
Chopper deflection angle	5.3 mrad	
RF frequency buncher cavities	352.2 MHz	
Maximum buncher voltage	150 kV	
RF peak power per buncher	16–18 kW	
Number of buncher cavities	3	At 352.2 MHz
Number of chopper structures	2	Inside quadrupoles
Number of quadrupoles	11	
Length of chopper plates	400 mm	
Chopper plate distance	20 mm	
Length	3.7 m	
Beam collimation	$\approx 9\%$	
Transverse output emittance	0.32 π mm mrad	r.m.s., norm., collimated
Longitudinal output emittance	0.17 π deg MeV	At 352.2 MHz
	0.43 π mm mrad	r.m.s., normalized
Vacuum	10^{-7} mbar	
DTL		*Table 4.4*
Input energy	3 MeV	
Output energy	40 MeV	
RF frequency	352.2 MHz	
Peak current	64 mA	
Average pulse current	40 mA	
Design RF duty cycle	14%	
Gradient E_0	3.3/3.5 MV/m	1st / (2nd,3rd) tank
Maximum surface field	1.4–1.7 kilpatrick	
Synchrotron phase	$-30 \rightarrow -20/-20$ deg	1st / (2nd,3rd) tank
RF beam power	1.5 MW	
RF peak power per tank	0.7/1.57/1.55 MW	1st/2nd/3rd tank
RF peak power	3.8 MW	
Number of klystrons	1/2/2	1st/2nd/3rd tank
Cells per tank	28/33/24	1st/2nd/3rd tank
Number of tanks	3	
Focusing tank 1	FOFODODO	
Focusing tank 2/3	FODO	
Length per tank	2.63/5.2/5.0 m	1st/2nd/3rd tank
Total length	13.4 m	
Transition to CCDTL	0.25 m	
Beam aperture	20 mm	
Quadrupole type	PMQ	
Quadrupole length	45/80 mm	1st / (2nd,3rd) tank
Outer drift tube diameter	90 mm	
Inner quadr. diameter	22 mm	
Transverse output emittance	0.34 π mm mrad	r.m.s., normalized
Longitudinal output emittance	0.19 π deg MeV	At 352.2 MHz

table continued on next page

Parameter	Value	Comment
	0.49 π mm mrad	r.m.s., normalized
Vacuum	10^{-7} mbar	
CCDTL		*Tables 4.5 and 4.6*
Input energy	40 MeV	
Output energy	92 MeV	
RF frequency	352.2 MHz	
Peak current	64 mA	
Average pulse current	40 mA	
Design RF duty cycle	14%	
Gradient E_0	2.8–3.9 MV/m	
Maximum surface field	1.4–1.7 kilpatrick	
Synchr. phase	−20 deg	
RF beam power	2 MW	
RF power per module	0.8 MW	
RF peak power	6.4 MW	
Number of klystrons	8	
Cells per cavity	3	
Cavities per module	3	
Number of cavities	24	
Number of modules	8	
Focusing	FODO	
Length	25.2 m	
Transition to SCL	0.25 m	
Beam aperture	28 mm	
Transverser output emittance	0.35 π mm mrad	r.m.s., normalized
Longitudinal output emittance	0.19 π deg MeV	At 352.2 MHz
	0.48 π mm mrad	r.m.s., normalized
Vacuum	10^{-7} mbar	
SCL		*Tables 4.7 and 4.8*
Input energy	92 MeV	
Output energy	180 MeV	
RF frequency	704.4 MHz	
Peak current (at 704.4 MHz)	128 mA	Every 2nd RF bucket filled
Average pulse current	40 mA	
Design RF duty cycle	14%	
Gradient E_0	4 MV/m	
Maximum surface field	1.1–1.2 kilpatrick	
Synchrotron phase	−20 deg	
RF beam power	3.6 MW	
RF peak power	15.1 MW	
Number of klystrons	5	
Cells per cavity	11	
Cavities per module	4–5	
Number of cavities	24	
Focusing	FODO	
Length	34.4 m	
Transition to SC linac	0.5 m	

table continued on next page

Parameter	Value	Comment
Beam aperture	32 mm	
Transverse output emittance	0.36 π mm mrad	r.m.s., normalized
Longitudinal output emittance	0.19 π deg MeV	At 352.2 MHz
	0.48 π mm mrad	r.m.s., normalized
Vacuum	10^{-7} mbar	
SC linac		*Tables 4.11, 4.12, 4.13, 4.14*
Input energy	180 MeV	
Output energy	3.56 GeV	
RF frequency	704.4 MHz	
Peak current (at 704.4 MHz)	128 mA	Every 2nd bucket filled
Average pulse current	40 mA	
Cryo duty cycle	4.6/5.5%	'neutrino'/'EURISOL'
Design cryo duty cycle	6%	
(R/Q)	290/570 Ω	Linac definition (β = 0.65/1.0)
Q_0	10^{10}	Min. performance goal (β = 0.65/1.0)
Q_l	0.9/1.0 $\times 10^6$	(β = 0.65/1.0)
Filling time τ_l	0.21/0.23 ms	Q_l/ω (β = 0.65/1.0)
Gradient E_0	19/25 MV/m	Without transit time factor (β = 0.65/1.0)
Synchronous phase	$-20 \rightarrow -15$ deg	
RF peak power	135.2 MW	
Number of klystrons	7/32	(β = 0.65/1.0)
Cells per cavity	5	
Active length per cavity	0.692/1.064 m	(β = 0.65/1.0)
Number of cavities	42/136	(β = 0.65/1.0)
Cavities per cryo-module	6/8	+4 quads / +2 quads (β = 0.65/1.0)
Foc. periods per cryo-module	2/1	(β = 0.65/1.0)
Number of cryo-modules	7/17	(β = 0.65/1.0)
Length of cryo-module	11.45/14.26 m	(β = 0.65/1.0)
Dist. between cryo-modules	0.8 m	
Focusing	FDO	
Period length	6.13/15.06 m	(β = 0.65/1.0) cryostat transitions
Length	85.8/256.1 m	(β = 0.65/1.0)
SC linac length	342 m	
Beam aperture	85/90 mm	Diameter
Transverse output emittance	0.36 π mm mrad	r.m.s., normalized
Longitudinal output emittance	0.20 π deg MeV	At 352.2 MHz
	0.50 π mm mrad	r.m.s., normalized
Vacuum	10^{-9} mbar	